Search for supersymmetry in events with at least one photon, missing transverse momentum, and large transverse event activity in proton-proton collisions at 13 TeV with the CMS detector in 2016

Von der Fakultät für Mathematik, Informatik und Naturwissenschaften der RWTH Aachen University zur Erlangung des akademischen Grades eines Doktors der Naturwissenschaften genehmigte Dissertation

vorgelegt von

Maximilian Knut Kiesel, M. Sc. RWTH

aus

Stuttgart

Berichter: Prof. Dr. Lutz Feld
Prof. Dr. Jörg Pretz

Tag der mündlichen Prüfung: 20. Juni 2018

Zusammenfassung

In dieser Arbeit wird eine Suche nach Supersymmetrie (SUSY) vorgestellt. Betrachtet werden Ereignisse aus Proton-Proton Kollisionen am CERN LHC mit einer Schwerpunktsenergie von 13 TeV, die vom CMS Detektor gemessen wurden. Die analysierten Daten entsprechen einer integrierten Luminosität von $35{,}9\,\mathrm{fb}^{-1}$ und wurden im Jahr 2016 aufgezeichnet. SUSY stellt eine Erweiterung des Standardmodells der Elementarteilchenphysik (SM) dar, die neue Teilchen, wie zum Beispiel Gravitinos oder Gluinos, vorhersagt. In den in dieser Arbeit betrachteten Modellen werden Ereignisse mit Photonen und Gravitinos im Endzustand erwartet. Die Gravitinos können nicht direkt detektiert werden, sodass ein nicht-vernachlässigbarer fehlender transversaler Impuls im Event gemessen wird. Wenn solche Ereignisse über die starke Wechselwirkung produziert werden, werden zusätzlich Jets erwartet. Es werden Ereignisse mit mindestens einem hochenergetischen Photon, großer transversaler Aktivität von Jets und einem großen fehlenden transversalen Impuls selektiert. Der Beitrag von SM Ereignissen wird mithilfe von simulierten Ereignissen sowie gemessenen Daten abgeschätzt. Um die Sensitivität der Suche zu erhöhen, wird die Selektion in sechs Regionen unterteilt. Es wird kein signifikanter Überschuss von Ereignissen zusätzlich zur SM Vorhersage beobachtet. Interpretiert wird die Analyse unter anderem in vereinfachten SUSY Modellen mit Gluinopaarproduktion mit unterschiedlichen Szenarien für die Zerfallswahrscheinlichkeiten für die Gluinos. Die Gluinos können in mehreren Schritten zu Photonen, Gravitinos und Jets zerfallen. Abhängig von der Neutralinomasse können Gluinomassen bis zu 1,5–2 TeV mit einem Vertrauensniveau von 95% ausgeschlossen werden. Diese Analyse liefert die bisher stärksten Ausschlussgrenzen für kleine Neutralinomassen in den betrachteten Modellen.

Abstract

In this thesis, a search for supersymmetry (SUSY) is presented. Events from proton-proton collisions at the CERN LHC with a center-of-mass energy of 13 TeV are considered, measured with the CMS detector. The data correspond to an integrated luminosity of $35.9\,\mathrm{fb}^{-1}$, recorded in the year 2016. SUSY is an extension to the standard model of particle physics (SM), which predicts new particles, such as for example gravitinos or gluinos. In the models considered in this thesis, events with photons and gravitinos in the final state are expected. Gravitinos cannot be detected, such that non-negligible missing transverse momentum is measured in the event. If the events are produced via the strong interaction, jets are expected in addition. Events with at least one high-energy photon, large transverse jet activity, and a large missing transverse momentum are selected. The contribution of SM events is estimated using data control regions and simulated events. To increase the sensitivity of the analysis, the selection is divided into six regions. No significant excess of events above the SM prediction is observed. The analysis is interpreted among others in terms of simplified models of gluino pair production with different scenarios for the decay probabilities of the gluinos. The gluinos can decay in several steps to photons, gravitinos, and jets. Depending on the mass of the neutralino, gluino masses up to 1.5–2 TeV are excluded with a confidence level of 95%. This analysis sets up to now the most stringent limits for low neutralino masses in the scenarios considered.

Contents

1 Introduction

"What is everything made of? Where do we come from?" These questions are as old as humankind, but the scientific method seems to bring us closer to answering such questions. We hypothesise theories to describe nature, make predictions, and perform experiments to test these theories.

One of these theories is the standard model (SM) of particle physics, describing the fundamental particles and their interactions. ("What is everything made of?") Among other, it predicted the top quark, the Higgs boson (however not the exact masses of these particles), and the existence of various hadrons. Parameters of the theory are well studied, and measurements from various experiments have confirmed the predictions of the SM with great precision. However, there are measurements which can only be explained by extensions of the SM. In addition, there are also theoretical concerns, leading to many new theories for physics beyond the SM. Testing the SM or possible extensions at high energy scales results in an environment similar to the one shortly after the big bang. ("Where do we come from?")

An attractive theory is supersymmetry (SUSY), which postulates partner particles to each of the SM particles. Particles and their partner particles have the same quantum numbers, except for the spin, which differs by $\hbar/2$. As such particles have not been found yet, the partner particles must also have larger masses. In the models considered in this thesis, gluinos, the partner particles of the gluons are assumed to be pair-produced in proton-proton collisions. They can decay in several steps to jets, photons and gravitinos. Gravitinos are partner particles of the gravitons, the hypothetical elementary particle mediating the gravitational force.

To establish the existence of the Higgs boson and find clues for physics beyond the SM, the Large Hadron Collider was build at the European Organization for Nuclear Research (CERN). Most theories predict new physics to appear at the TeV scale, which is in reach of the collider. Protons are accelerated counter-rotating to a center-of-mass energy of 13 TeV, and brought to collision. At one of the collision points, the CMS detector is located, measuring particles produced in such collision events.

In this thesis, data corresponding to an integrated luminosity of $35.9\,\mathrm{fb}^{-1}$ are used, recorded in 2016. Gravitinos cannot be directly detected, but can be traced by the missing transverse momentum. The transverse event activity is defined as the scalar sum of all jet momenta and the momentum of the highest energy (leading) photon. Events with at least one high-energy photon, large transverse event activity, and large missing transverse momentum are selected. This event selection also contains events from SM processes, and their contribution and uncertainty to the event yield needs to be determined. The contribution from SM events with nongenuine missing transverse momentum is estimated using events from a SUSY signal depleted event selection. Events with electrons can enter the search region, if the electron is misidentified as a photon. An electron-to-photon scale factor is determined from events containing a Z boson, and applied to an electron control region to estimate the contribution to the search region. The contribution from SM events with a genuine photon and considerable genuine missing transverse momentum is estimated using simulation. To increase the sensitivity of the analysis, the search region is divided into six subregions.

Upper limits on the production cross section of simplified supersymmetric processes are determined as a functions of SUSY particle masses. The results of this thesis are published by the Journal of High Energy Physics [1]. Here, a more detailed version is presented with additional studies and explanations. Figures taken from the publication are created by the author.

In section 2, the theoretical foundation of this thesis is outlined. Section 3 describes the experimental setup. The event simulation and reconstruction is depicted in section 4. The event selection and the background estimation methods are described in section 5 and the results and interpretations in section 6. In section 7, the analysis is compared to other analyses. A summary is given in section 8.

2 Theoretical foundations

A brief introduction to the theoretical foundations is given in this chapter. To simplify the notation, natural units are used, in which the reduced Planck constant $\hbar$ and the velocity of light c are set to unity:

$$\hbar = c = 1$$

Momentum, mass, and energy are therefore measured in terms of eV $\approx 1.6 \times 10^{-19}$ J. Spin is a dimensionless quantity. For length and time the metric system is used.

2.1 Standard model

The SM model of particle physics was developed during the second half of the 20th century and describes the interactions of elementary particles [2]. It is a gauge quantum field theory based on the SU(3) × SU(2) × U(1) gauge group, which describes the electromagnetic, the weak, and the strong force. The only fundamental force not included is the gravitational force, which is weak in comparison to the forces described by the SM.

All particles are composed of elementary particles, which can be divided into fermions with half integer spin and bosons with integer spin. To give mass to the gauge bosons W^1, W^2, W^3 (of the SU(2) gauge group), and B^0 (of the U(1) gauge group) with the corresponding couplings g and g', the Higgs field

$$V(\phi) = \mu^2 \phi^\dagger \phi + \lambda (\phi^\dagger \phi)^2, \qquad \mu^2 < 0,\ \lambda > 0,$$

is added to the SM lagrangian [3–6], where ϕ is a doublet of complex fields. The ground state of ϕ at $\nu^2 = -\mu^2/\lambda$ spontaneously breaks the gauge symmetry, resulting in one neutral Higgs scalar (H). The number of H bosons is not specified, but so far only one H boson with a mass of about 125 GeV was found [7, 8]. As a further result of the Higgs mechanism, the gauge bosons mix to the massless electromagnetic photon

$$\gamma = B \cos\theta_W + W^3 \sin\theta_W,$$

and the neutral and charged gauge bosons of the weak force

$$Z = -B \sin\theta_W + W^3 \cos\theta_W$$

and

$$W^\pm = (W^1 \mp i W^2)/\sqrt{2},$$

with masses of about 91 GeV and 80 GeV, respectively [2]. The weak mixing angle is given by

$$\theta_W = \tan^{-1}\left(g'/g\right),$$

while the electric elementary charge is $e = g \sin\theta_W$. The weak mixing angle can be determined to $\sin^2\theta_W = (0.2223 \pm 0.0021)$ [9]. The strong force is mediated by eight massless gluons (g) with spin 1, which are the gauge bosons of the SU(3) gauge group.

Fermion elementary particles arise in three generations, with the same quantum numbers but different masses. To each fermion, there exists an antiparticle, with the same mass, lifetime, and spin, but opposite electric charge. If not explicitly stated, the name of the particle is used for both particle and antiparticle. Elementary SM fermions are leptons and quarks. The electrically charged leptons (ℓ) are the electron e, the muon μ, and the tau τ lepton with masses of about 511 keV, 106 MeV, and 1.78 GeV, respectively [2]. They all carry one electrical charge and interact with the electromagnetic and the weak force. The electrically neutral leptons are the neutrinos ν, which are massless in the SM. They interact with the weak force only. Two types of quarks exist: up-like quarks (up, charm, and top) with 2/3 electrical charge and down-type quarks (down, strange, and bottom) with $-1/3$ electrical charge. As they carry color in addition to the weak and electric charge, they interact with all the forces described above. Unbound colored particles are not observed, as they hadronize and form jets, which are multiple hadrons within a tight cone around the quark's or gluon's initial momentum. The top quark with a mass of about 173 GeV is exceptionally heavy and decays almost always to a bottom quark and a W boson before the hadronization process starts [10]. The masses arise from the coupling of the particles to the Higgs field.

All elementary SM particles and interactions are shown in figure 2.1. The H, W, and gluon also couple to themselves.

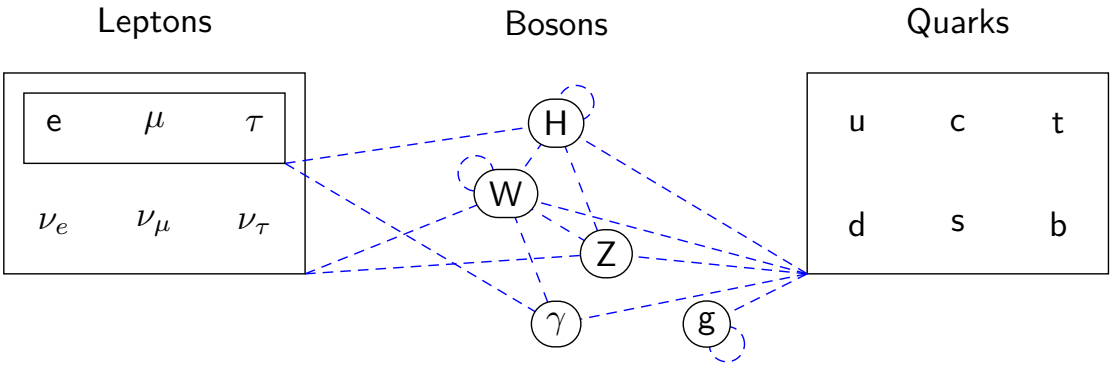

Figure 2.1: SM fermions (in boxes) and bosons (in rounded boxes) and their interactions (blue dashed lines). All bosons except for the photon and the Z boson couple to themselves.

The cross section σ of a process, which is a measure of the probability for particle interactions, is calculated in perturbation theory and is given in barn ($1\text{b} = 10^{-28}\text{m}^2$). Terms in this calculation can be illustrated by Feynman diagrams. Figure 2.2 shows an example Feynman diagram for a $u\overline{u} \to \gamma Z \to \gamma\nu\overline{\nu}$ process in leading order (LO). The next-to-leading order (NLO) Feynman diagrams contain one additional vertex.

2.2 Indications for physics beyond the standard model

Although the SM describes most experimental results to a high precision, there are many reasons suggesting the SM is not complete, motivating physics beyond the SM (BSM).

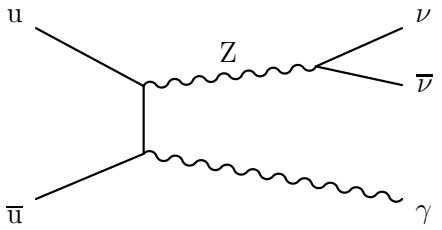

Figure 2.2: Feynman diagram for a $u\overline{u} \to \gamma Z \to \gamma\nu\overline{\nu}$ process. Here, antiparticles are marked explicitly by a bar.

Neutrino masses

In the SM, neutrinos are assumed to be massless. Observed neutrino oscillations however indicate that at least two neutrino masses are nonzero [11], contradicting the prediction from the SM. The observed neutralino oscillation can however be explained by extensions of the SM [12].

Baryon asymmetry

If the initial state of our universe is assumed to have contained the same amount of matter and antimatter, it is puzzling that today more matter than antimatter is observed [13]. Charge-conjugation-parity can be violated through the complex phase in the quark mixing matrix and in models explaining nonzero neutrino masses [14]. However, the size of the effect is not large enough to explain the observed excess of matter with respect to antimatter.

Dark matter

Dark matter is a hypothetical type of matter, which interacts neither electromagnetically nor strongly, but gravitationally and possible weakly. It is not directly observed up to now, but several astrophysical phenomena are well described with dark matter. The rotational velocity of galaxies is larger than expected when only taking the visible mass of the galaxy into account [15]. In addition, there are gravitational lenses without any visible heavy objects causing the bending of space-time [16]. Fits of the standard model of cosmology to the cosmic microwave background yield that only 4.8% of the energy density of the universe is ordinary matter, whereas 25.8% of the energy density is dark matter [17]. The residual 69.4% of the energy density is assigned to dark energy, of which even less is known [17].

Neutrinos and black holes are the only SM candidates for dark matter, but their contribution to dark matter is by far not enough to explain all dark matter. Certain BSM theories introduce new particles, which could be candidates for dark matter.

Unification of forces

Historically, it turned out that some scientific theories were only special cases of a larger framework. Unifying theories leads to a deeper understanding of the phenomena and provides a better model for experimental observations. Examples are the unification of the electric and the magnetic force to the electromagnetic force [18], or of the electromagnetic and the weak force to the electroweak force [19–21].

Although the electroweak and the strong force are both described by quantum field theories, their current modeling in the SM is not unified [22]. These two processes may indeed be independent, but there may also be a deeper common mechanism leading to both phenomena [23].

In addition to the unification of the strong and the electroweak force, there also are approaches to unify the SM forces with the gravitational force [24]. The SM describes physics at small scales, while gravity dominates physics at large scales. While the strong force and the electroweak force both are described in quantum field theories, there is no similar description of the gravitational force, which makes this unification even more difficult.

Hierarchy problem

For most particles, higher-order quantum-loop corrections to the mass are smaller than the observed mass, but for the H boson, this is not the case [22, 25]. For the H boson, the contribution from corrections is given as

$$\Delta m_{\mathrm{H}}^2 = -\frac{2|\lambda_f|^2}{16\pi^2}\Lambda_{UV}^2 + \frac{\lambda_S}{16\pi^2}\Lambda_{UV}^2 - \frac{m_S^2\lambda_S}{8\pi^2}\ln(\Lambda_{UV}/m_S) + \cdots , \tag{2.1}$$

where the first (second) term results from the left (right) diagram shown in figure 2.3 and corresponds to the coupling of fermions (scalars) with the coupling constant λ_f (λ_S) [22]. The mass of the scalar is denoted as m_S, and the ultraviolet cutoff parameter Λ_{UV} corresponds approximately to the energy scale to which the theory is valid. In the SM, the first two terms do not cancel, leading to a quadratic dependence on Λ_{UV}. If the SM is valid up to the Planck energy scale of about 10^{19} GeV, at which gravitational effects are assumed to contribute to the theory, the bare H mass and the corrections must be fine-tuned to yield an observed H mass of 125 GeV [26].

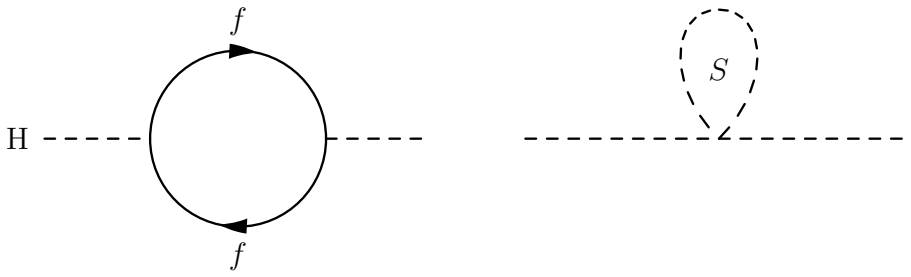

Figure 2.3: Feynman diagrams for H mass corrections with fermions (left) and scalars (right).

2.3 Supersymmetry

SUSY [22,27–33] is a symmetry transforming fermions into bosons and vice versa. It introduces a supersymmetric partner particle for each chirality state of each SM particle with the same quantum numbers, except for the spin, which differs by 1/2. For the nomenclature of SUSY particles (sparticles), the following scheme is used: An "s" is prepended to each name of a SM fermion to name its SUSY partner (squark, slepton, ...), while the names of the SUSY fermions are built with the SM particle name and "ino" at the end (bino, gluino, ...). Due to the structure of SUSY, several H particles are needed to give mass to the up-type and down-type quarks. Their superpartners are the higgsinos. If gravity is included, the SM particle content is extended by the graviton (G) whose superpartner is the gravitino ($\widetilde{G}$). The particle content of the minimal supersymmetric extension is shown in figure 2.4.

Gauginos are the SUSY partners of SM gauge bosons and H particles. The neutral gauge eigenstates of the higgsinos ($\widetilde{H}_{u/d}^0$), the bino ($\widetilde{B}$) and the neutral wino ($\widetilde{W}^0$) mix to the

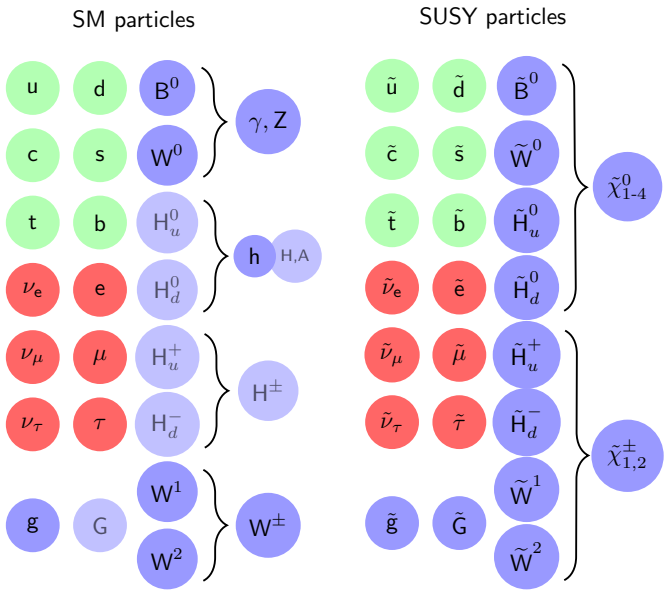

Figure 2.4: Particle content of the minimal supersymmetric model. The SM particle content is extended by additional H bosons and the graviton. Gauge eigenstates of the SM bosons and SUSY fermions are given, and their corresponding mixture to their mass eigenstates.

neutralino mass eigenstates according to

$$\begin{pmatrix} \widetilde{\chi}_1^0 \\ \widetilde{\chi}_2^0 \\ \widetilde{\chi}_3^0 \\ \widetilde{\chi}_4^0 \end{pmatrix} = \begin{pmatrix} M_1 & 0 & -c_\beta s_W m_Z & s_\beta s_W m_Z \\ 0 & M_2 & c_\beta c_W m_Z & -s_\beta c_W m_Z \\ -c_\beta s_W m_Z & c_\beta c_W m_Z & 0 & -\mu \\ s_\beta s_W m_Z & -s_\beta c_W m_Z & -\mu & 0 \end{pmatrix}^{-1} \begin{pmatrix} \widetilde{B} \\ \widetilde{W}^0 \\ \widetilde{H}_d^0 \\ \widetilde{H}_u^0 \end{pmatrix}, \tag{2.2}$$

where $c_\beta = \cos\beta$, $s_\beta = \sin\beta$, $c_W = \cos\theta_W$, and $s_W = \sin\theta_W$. M_1 and M_2 are the bino- and wino mass terms, $\tan(\beta)$ the ratio of the vacuum expectation values of the two Higgs doublets, and μ the higgsino mass term. The lightest neutralino is denoted as $\widetilde{\chi}_1^0$. The charged gauge eigenstates of the higgsinos and winos mix to the charginos ($\widetilde{\chi}_{1,2}^{\pm}$). The couplings of supersymmetric partners are the same as for their SM particles.

With the supersymmetric extension of the particle spectrum as discussed above, the quadratic divergences in Λ_{UV} of the H boson mass corrections in equation 2.1 are canceled: In SUSY, the coupling constants $|\lambda_f|^2 = \lambda_S$ are the same. Due to the different chiralities of fermions, there are twice as many scalars, cancelling the factor of 2 in equation 2.1 and thus solving the hierarchy problem.

The coupling constants for the electromagnetic ($\alpha_{\mathrm{U}(1)}$), weak ($\alpha_{\mathrm{SU}(2)}$), and strong ($\alpha_{\mathrm{SU}(3)}$) force are functions of the interaction energy. With additional particles, the running of the coupling constants changes. Figure 2.5 shows the coupling constants for the SM, where no unification of the forces is possible compared to the coupling constants with the minimal supersymmetric extension of the SM where a unification can be achieved at high energies [34].

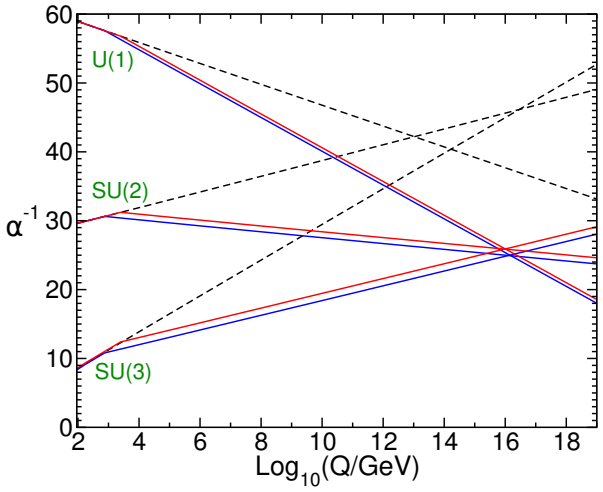

Figure 2.5: Running couplings for SM (dashed black lines) and for a SUSY model (colored solid lines). The sparticle masses are treated as a common threshold varied between 750 GeV and 2.5 TeV in the SUSY model [22].

2.3.1 *R*-parity conservation

R parity is a multiplicative quantum number defined by

$$R = (-1)^{3(B-L)+2s},$$

where B, L, and s are the baryon number, the lepton number, and the spin, respectively. R is $+1$ for SM particles and -1 for sparticles.

In this thesis, R-parity is assumed to be conserved. This is well motivated by the long measured life time of the proton [35], which restricts many R-parity violating couplings. R-parity conservation has the phenomenological consequences that sparticles are produced in pairs only, and that the lightest supersymmetric particle (LSP) is stable. In some R-parity conserving models, the LSP can be a dark matter candidate. The models considered in this thesis predict light LSPs, which are excluded to contribute strongly to dark matter [36].

2.3.2 Gauge mediated supersymmetry breaking

If SUSY was a perfect symmetry, the mass of sparticles would be the same as the one of their SM partners. Since this is not the case, SUSY must be a broken symmetry. Gauge mediated SUSY breaking (GMSB) [37–44] models introduce new messenger particles, which couple to the sparticles via gauge bosons. In GMSB models, the gravitino is the LSP. In this analysis, it is assumed that the gravitino is close to massless and the lightest neutralino is assumed to be the next-to-lightest SUSY particle. The decay lengths of the gauginos depend on the scale of SUSY breaking and can be anything from sub-micron to kilometer. Here, a prompt decay of the gauginos is assumed. Gauginos can decay into a gravitino and their SM partner-particle, depending on the mixture of the gauginos. If the lightest neutralino is 100% $\widetilde{B}$, the decay probability to a photon and a gravitino is large, as is shown in figure 2.6. Heavy neutralinos composed solely of $\widetilde{W}$ dominantly decay to a Z boson, but, especially for smaller masses, the decay into a photon is also possible [45].

If the neutralino composed solely of higgsinos, the branching fractions depend on the parameters introduced in equation 2.2. Figure 2.7 shows two examples of parameter sets. For light neutralino masses, the decay into a photon is dominant for all parameters. For $m_Z < m_{\widetilde{\chi}_1^0} < m_H$,

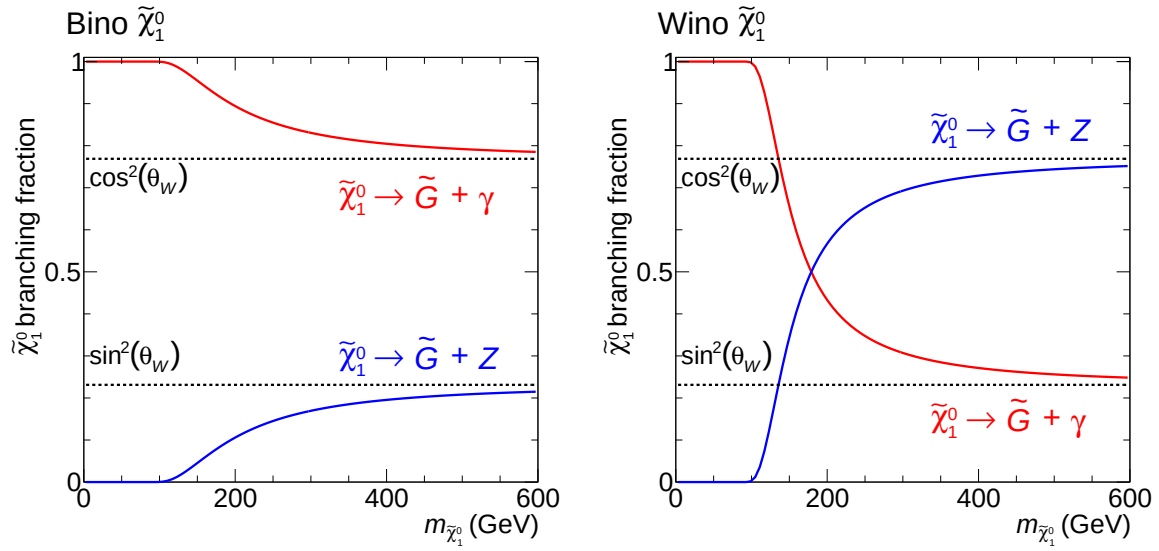

Figure 2.6: Neutralino branching fraction as a function of the neutralino mass for neutralinos composed solely of bino (left) and neutralinos composed solely of wino (right). At high masses, the branching fractions converge to the squared sine or cosine of the weak mixing angle.

the decay to a Z boson is dominant. If the lightest chargino ($\tilde{\chi}_1^\pm$) mass is close to the $\tilde{\chi}_1^0$ mass, the decay $\tilde{\chi}_1^\pm \to \tilde{\chi}_1^0 + W^\pm$ is suppressed, and the chargino can decay directly to a gravitino and a W boson.

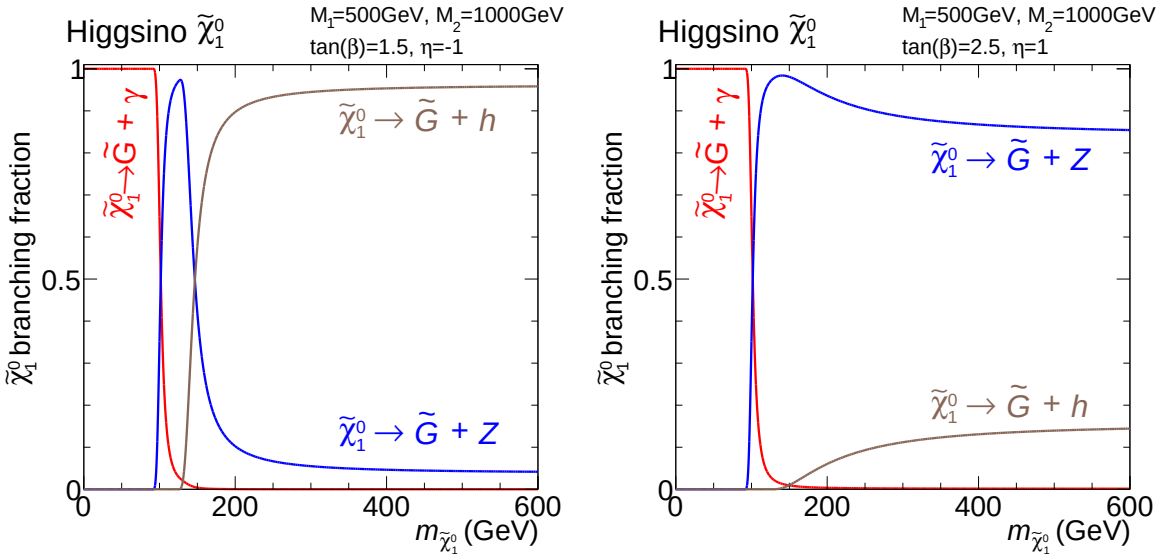

Figure 2.7: Neutralino branching fraction as a function of the neutralino mass for neutralinos composed solely of higgsinos for two different parameter sets. Here η is the sign of μ [45].

2.3.3 Status of searches for supersymmetry

Searches for SUSY were performed at experiments at the LEP [46], Tevatron [47], and the LHC colliders, but no clear hint for BSM physics has been found yet. Due to the higher

center-of-mass energy ($\sqrt{s}$) and integrated luminosity provided by the LHC, the most stringent restrictions on BSM physics come from the LHC experiments. Many BSM models can be constrained by precision measurements of SM parameters, which could be altered by non-SM particles. The most important constraints are the measurement of the H boson branching fractions [48] and the cross section and branching fractions of the $B_s^0 \to \mu\mu$ process [49], which are both compatible with the SM expectations. SUSY models are also probed directly, and squark (gluino) masses of up to 1.5 (2) TeV can be excluded, depending on the specific model. The limits for gauginos are less stringent.

Several signatures for GMSB were probed: Long lived neutralinos with a decay length of up to 6 m can be excluded up to a mass of 220 GeV [50], and neutralinos with a decay length of up to 0.6 m can be excluded up to a mass of 430 GeV [51]. Signatures without a requirement on the missing transverse momentum can exclude squark masses of up to 1050 GeV [52]. Such final states appear in stealth models of SUSY, which predict a hidden sector at the electroweak energy scale. In models with two photons produced via top squarks, top squark masses of up to 750 GeV can be excluded [53]. With a photon and a lepton signature, gluino masses up to 1.1 TeV can be excluded [54]. In addition to gluino production via the strong interaction, the photon and lepton analysis is also sensitive to the production of primary sparticles via the electroweak force (electroweak models). Signatures with two photons provide good sensitivity for large neutrino to photon branching ratios [55, 56]. In case of higgsino-like neutralinos, signals can be tagged by two photons with an invariant mass close to the H boson mass [57]. Searches for BSM physics in events with photons, jets, and large transverse momentum imbalance have been carried out by ATLAS [58] and the predecessor of this analysis [59], the latter one being sensitive to gluino masses of up to 1.2 TeV, but no hint for BSM physics has been found. The analysis presented in this thesis was developed in parallel to an analysis concentrating on scenarios with low jet multiplicity and electroweak production models [60]. Comparisons to this analysis are discussed in section 7.1.

As sparticle masses are not predicted by the theory, it is hard to exclude SUSY completely. Then again the amount of fine-tuning occurring in the hierarchy problem increases with increasing sparticle masses. Therefore, too heavy SUSY particles are disfavored. This analysis targets a mass scale at the order of a few TeV, at which SUSY is expected to produce effects which result only in a moderate fine-tuning.

2.3.4 Simplified models

The minimal extension of SUSY extends the number of SM parameters by about 120 and offers many different final states. Probing all parameter combinations is unrealistic. Simplified model spectra (SMS) are effective Langrange-descriptions of BSM models, and can be used to characterize BSM physics. Most sparticles are decoupled, such that only a small number of sparticles contribute to the process [61]. The simplicity of the final state also allows easy reinterpretations in other BSM models. A nomenclature, similar to the one introduced in reference [62], is given as well in brackets. In this analysis, four signal SMS are considered:

Squark-diphoton model (T6gg)

A right- and left-handed partner of the first- or second-generation quark and its antisquark are pair produced in proton-proton interactions, leading to eight possible squark states. Both squarks decay into a quark and a neutralino. The neutralino then decays to a photon and a gravitino. All branching fractions are assumed to be 100%. All sparticles except for the gravitino, the neutralino and the squark are assumed to be decoupled by setting their mass to high unreachable values. The gravitinos are simulated with a mass of 1 GeV, and gauginos

are decaying promptly. The Pseudo-Feynman diagram of this model is shown in the top left of figure 2.8. In the final state, there are two gravitinos, two photons and two jets.

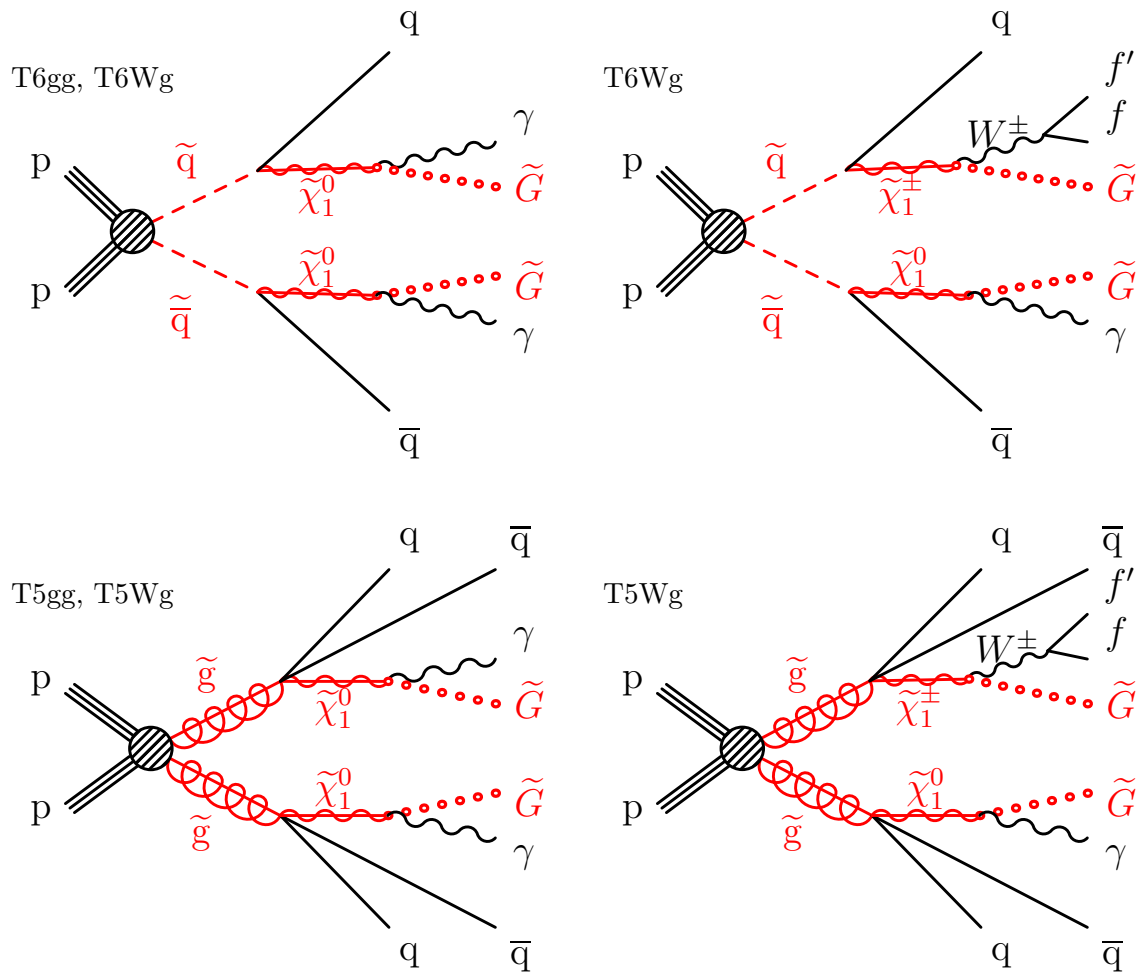

Figure 2.8: Pseudo-Feynman diagrams for the squark-diphoton (top left), squark-single-photon (top), gluino-diphoton (bottom left), and gluino-single-photon (bottom) models. SUSY particles are marked in red. The W decays to two fermions f. The single-photon models also include events with two W bosons.

Squark-single photon model (T6Wg)

This model is similar to the squark-diphoton model, except that the squark to quark and neutralino branching fraction is limited to be 50%, while in all other cases the squark decays to a chargino and a quark. The chargino then decays to a W and a gravitino. Possible Pseudo-Feynman diagrams for this model with photons in the final state are shown in the top of figure 2.8. There are three possible final states: Two gravitinos, two jets, and two photons; two gravitinos, two jets, one photon, and the decay products of one W; and two gravitinos, two jets and the decay products of two W. In total, 75% of the events contain at least one photon.

Gluino-diphoton model (T5gg)

If the gluino is lighter than the lightest squark, gluino pair production is dominant. The gluino then decays in a three body decay into two quarks and one neutralino. This results in a similar final state as the squark-diphoton model, except that there are four instead of two jets. While the gluino mass is set to values reachable by the LHC, squarks are decoupled in this scenario. The Pseudo-Feynman diagram of this model is shown in the bottom left of figure 2.8.

Gluino-single-photon model (T5Wg)

Gluinos are produced in pairs, and decay with equal probability to either two jets and a neutralino, or to two jets and a chargino. The gauginos decay as described above, which leads to similar final states as the squark-single-photon model, except that there are four instead of two jets. Possible Pseudo-Feynman diagrams for this model with photons in the final state are shown in the bottom of figure 2.8.

Kinematic properties of the signal events

For all models, several combinations of squark/gluino and gaugino masses are considered. In the single-photon models, the neutralino and the chargino are assumed to be mass-degenerate. The gluino and the squark are initial pair produced particles, and the total energy of the final state particles correlates with the mass of the initially produced particles. The size of the gaugino mass influences the energy distribution of the decay products. To allow the squark/gluino to gaugino decay, the gaugino is always lighter than the squark/gluino. In compressed scenarios with small mass difference between the squark/gluino and the gaugino, most of the energy is transfered to the gauginos, leading to low-energy (soft) jets. The gravitinos and the bosons dominate the final state. If, however, the gaugino mass is small, much energy is transferred to jets, and little energy is available for the neutralinos, resulting in soft photons and soft gravitinos in a jet dominated event. If the chargino mass is below the W mass, the W boson is produced off-shell. For events in which the chargino mass is close to the W mass, much energy of the chargino is transferred to the W boson, and the energy of the gravitino is even smaller.

3 Experimental setup

In this analysis, events from high-energy proton-proton interactions are studied. The protons are accelerated at the Large Hadron Collider and the interactions are measured by the CMS detector. Both of these instruments are described in the following chapter.

3.1 Large Hadron Collider

The Large Hadron Collider (LHC) is a synchrotron which is used to accelerate protons or nuclei and bring them to collision to study their interactions [63]. It is located at the European Organization for Nuclear Research (CERN), around 100 m below the border of France to Switzerland near Geneva in a tunnel of 27 km circumference.

Protons are provided by ionizing hydrogen gas and are accelerated in an injection chain composed of the Linac2 linear accelerator, the Proton Synchrotron Booster (PSB), the Proton Synchrotron (PS) and the Super Proton Synchrotron (SPS). At an energy of 450 GeV, up to $n_\mathrm{b} = 2200$ bunches of on average $N_\mathrm{p} = 1.1 \cdot 10^{11}$ protons are injected counter-rotating into the two beam pipes of the LHC with a bunch-bunch separation of 25 ns [64]. For the data used in this analysis, they are accelerated to an energy of 6.5 TeV by a 400 MHz radio frequency accelerating system with an electric field of 5.5 MV/m. The center-of-mass energy $\sqrt{s}$ is therefore 13 TeV. Superconducting magnets with a maximal magnetic field of 8.33 T force the particles in the desired orbit. Quadropole, sextupole, octupole and decapole magnets modify the magnetic field to focus the beams. In four interaction regions, the beams are focused and brought to collision. At each collision point, a particle detector is located, namely the ATLAS detector [65], the ALICE detector [66], the LHCb detector [67], and the CMS detector [68]. The layout of the CERN accelerator facilities can be seen in figure 3.1.

The instantaneous luminosity can be calculated as

$$\mathcal{L} = \frac{N_\mathrm{p}^2 n_\mathrm{b} f_\mathrm{rev} \gamma_r}{4\pi \epsilon_n \beta^*} F,$$

where $f_\mathrm{rev} = 11246\,\mathrm{Hz}$ [69] is the revolution frequency, γ_r the relativistic gamma factor, $\epsilon_n \approx 2.2\,\mu\mathrm{m}$ the normalized transverse beam emittance, $\beta^* = 40\,\mathrm{cm}$ the beta function at the collision point, and F the geometric luminosity reduction factor depending on the crossing angle at the interaction point. It relates the cross section σ to the event rate $\dot{N}$ as

$$\mathcal{L} = \frac{\dot{N}}{\sigma}. \tag{3.1}$$

In the year 2016, a maximum instantaneous luminosity of $1.5 \cdot 10^{34}\,\mathrm{cm}^{-2}\,\mathrm{s}^{-1}$ was achieved [70].

3.2 Compact Muon Solenoid

The Compact Muon Solenoid (CMS) detector [68] is a multi-purpose apparatus, consisting from the inside to the outside of a silicon pixel and strip tracker, an electromagnetic and a

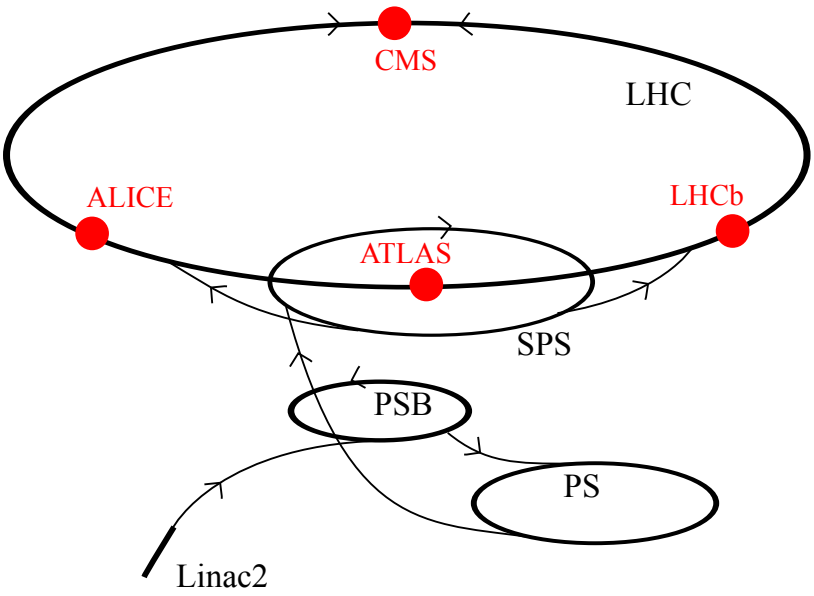

Figure 3.1: The layout of the LHC accelerator complex including preaccelerators. The four main LHC experiments are marked as red dots.

hadron calorimeter, a solenoid, and muon detectors. It is shaped cylindrically, with its axis being the beam pipe. Most detector systems have a barrel and two endcap parts. Figure 3.2 shows a layout of the detector.

Definition of the coordinate system

The origin of the coordinate system resides in the center of the CMS detector. The x-axis points towards the center of the LHC ring, the y-axis points vertically upwards, and the z-axis lies counterclockwise along the beam-pipe line, forming a right-handed coordinate system. The distance from the z-axis is calculated as $r = \sqrt{x^2 + y^2}$. The azimuthal angle ϕ is measured in the x-y-plane, with respect to the positive x-axis, ranging from $-\pi$ to π. With the polar angle θ, measured from the positive z-axis, the pseudorapidity $\eta = -\ln[\tan(\theta/2)]$ can be defined. For relativistic particles ($m \ll p$), η approximates the rapidity. The rapidity is used in most theoretical calculations, and differences in rapidity are Lorentz invariant under transformations along the z-axis. Distances in the $\eta - \phi$ plane are measured in $\Delta R = \sqrt{\Delta\phi^2 + \Delta\eta^2}$. Since the initial longitudinal momentum of the partons inside the colliding protons is unknown, transverse momenta $p_\mathrm{T} = |\vec{p}| \sin\theta$ are commonly used. If the mass of a particle can be neglected with respect to its kinetic energy, momenta can be approximated by the energy and vice versa.

Inner tracking system

The inner tracking system consists of a silicon pixel and a silicon strip detector. The silicon pixel detector was replaced in the beginning of 2017. In the following, the former pixel detector is described, which was used for the data analyzed in this thesis. The layers of the pixel barrel detector are located at radii of 4.4, 7.3, and 10.2 cm from the beam, and the pixel endcap detector disks at $z = \pm 34.5$ and ± 46.5 cm. The disposal of the disks and barrel layers is shown in figure 3.3. There are approximately 66 million pixels, each with an area of $100 \times 150\,\mu\mathrm{m}^2$.

The silicon strip detector surrounds the pixel detector and is composed of the Tracker Inner Barrel (TIB), Tracker Inner Disks (TID), Tracker Outer Barrel (TOB), and Tracker Endcaps

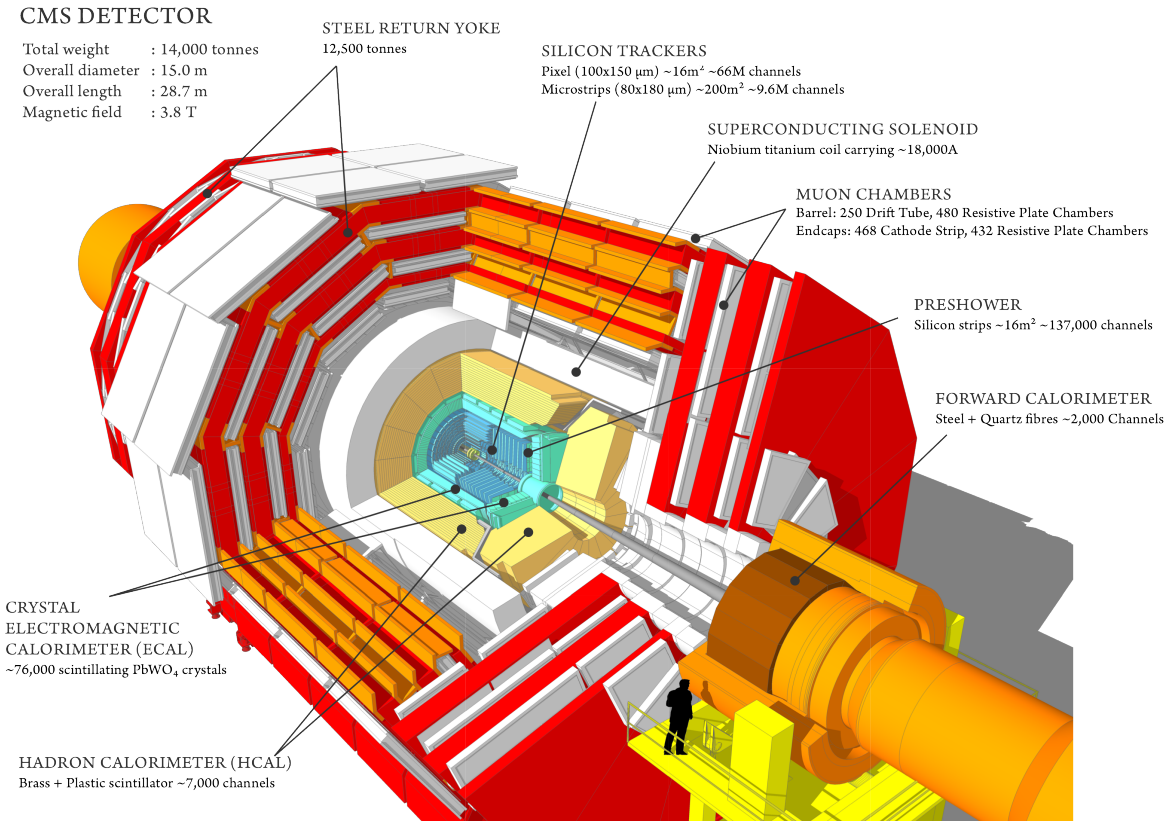

Figure 3.2: Layout of the CMS detector [71].

(TEC). The TIB consists of two inner layers of silicon micro strips with a strip pitch of 80 μm, and two outer layers with a strip pitch of 120 μm. It is located in $r < 55$ cm and $|z| < 70$ cm. The three disks of the TID are located between $z = \pm 80$ cm and ± 90 cm, and span the radius from about 20 cm to 50 cm. The mean pitch varies between 100 μm and 141 μm. The six layers of the TOB encloses the TIB and TID in radial direction, and extends in radius to 116 cm, with strip pitches between 122 μm and 183 μm. The TEC encloses the inner detectors in z-direction, extending to $z = \pm 282$ cm. Up to five rings of silicon micro-strip detectors are mounted on nine disks, with a strip pitch of 97 to 184 μm. This leads to a pseudorapidity coverage of $|\eta| < 2.5$.

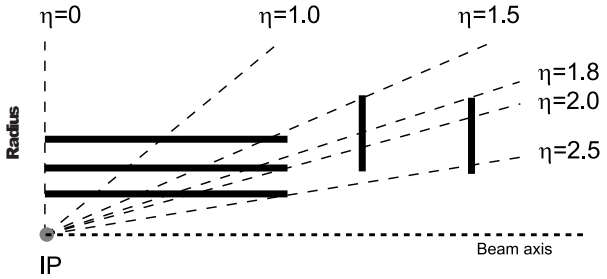

Figure 3.3: Sketch of one quadrant of the pixel detector in the z-y plane as black solid lines [68]. The dashed lines indicated the pseudorapidity.

Electrically charged particles transversing the depleted volume of the silicon semi-conductor induce an electric pulse, which is called hit. Several hits along the trajectory of a charged particle form a track. To minimize the interaction of particles with the inner tracking system,

a small material budget of about 0.4 to 1.8 radiation lengths for the inner tracking system is used.

For tracks from muons with $p_T = 100\,\text{GeV}$ in $|\eta| < 1.4$, the transverse impact parameter resolution reaches $10\,\mu\text{m}$, and the relative transverse momentum resolution is approximately 2.8% [72].

Electromagnetic calorimeter

The electromagnetic calorimeter (ECAL) surrounds the inner tracking system, and consists of a barrel part (EB) with a pseudorapidity coverage of $|\eta| < 1.479$ and two endcap parts (EE) with a coverage of $1.479 < |\eta| < 3.0$. A preshower detector is installed between the inner tracker and the EE. The layout of the ECAL is shown in figure 3.4.

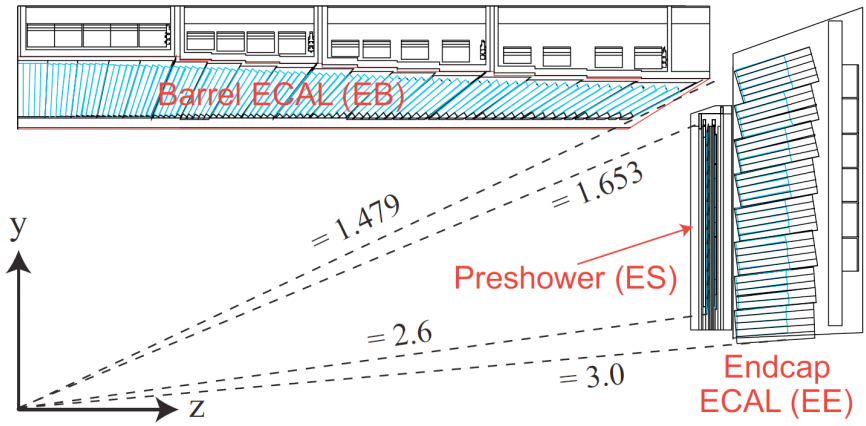

Figure 3.4: Sketch of one quadrant of the electromagnetic calorimeter in the z-y plane [73]. The dashed lines represent the boundaries of the detector in η.

The EB consists of 61 200 lead tungstate crystals with a front surface of 0.0174×0.0174 in η-ϕ (approximately $22 \times 22\,\text{mm}^2$). The crystal length of 230 mm corresponds to 25.8 radiation lengths. In the EE, the crystals have a front cross section of $28 \times 28\,\text{mm}^2$ and are arranged along the x- and y-axis. As shown in figure 3.4, the crystals are tilted, such that their front face points towards the interaction point. The crystal to crystal distance varies from 0.35 to 0.5 mm. Photons undergo electron-positron pair production, and electrons radiate photons, leading to electromagnetic showers. The scintillation light is measured with avalanche photodiodes (APD) in the barrel and vacuum phototriodes in the endcaps. The crystals and the electronics are water cooled to 18° C. As both the response of the crystals and the amplifications of the APDs are temperature dependent, the temperature is kept stable within 0.05° C.

The energy resolution of the ECAL can be parametrized as

$$\left(\frac{\sigma}{E}\right)^2 = \left(\frac{2.8\%}{\sqrt{E[\,\text{GeV}]}}\right)^2 + \left(\frac{0.12}{E[\,\text{GeV}]}\right)^2 + (0.30\%)^2,$$

where the first term describes the stochastic uncertainty, the second the noise, and the last term the constant uncertainties, like intercalibration errors of crystals, or shower leakage of energy from the back of the crystals [74].

Hadron calorimeter

The sampling hadron calorimeter (HCAL) consists of four parts: The barrel part (HB) and the endcap part (HE) reside within the solenoid, while the hadron outer (HO) calorimeter extends the barrel part at the outer side of the solenoid. The forward parts (HF) cover $3 < |\eta| < 5.2$ and are placed at $z = \pm 11.2\,\mathrm{m}$. The disposal is shown in figure 3.5.

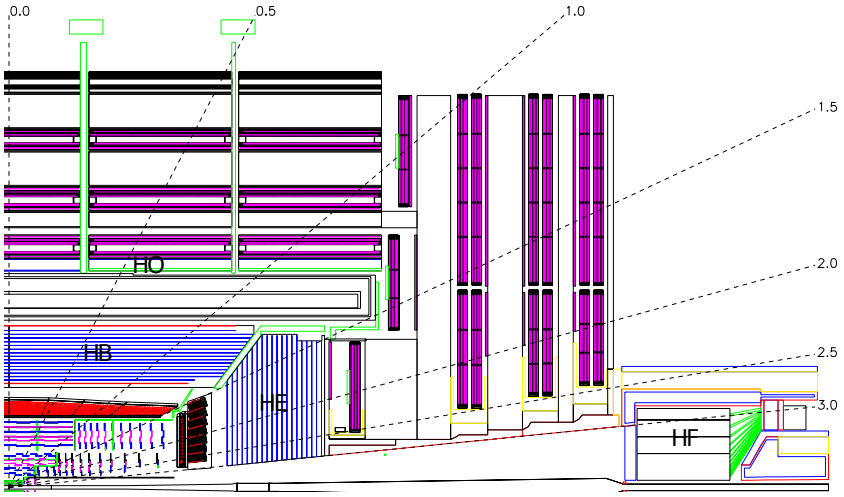

Figure 3.5: Longitudinal view of the CMS detector [68]. The dashed lines correspond to positions of equal η.

The barrel part resides in $1.77 < r < 2.95\,\mathrm{m}$, and is restricted by the outer extend of the ECAL and the magnet coil. It is a sampling calorimeter consisting of 36 wedges of flat brass absorber plates and stainless steel, aligned parallel to the beam axis. Steel is used to also support the large weight of the detector. The thickness of the absorber plates ranges from 40 to 75 mm, resulting in a total thickness of 6.7–11.7 interaction lengths, including the 1.1 interaction lengths of the ECAL. The plastic scintillator is segmented in $\Delta\eta \times \Delta\phi = 0.087 \times 0.087$ with a thickness of 3.7 mm made out of Kuraray SCSN81. Up to 16 longitudinal layers are used.

The hadron endcaps are constructed of brass absorber plates with a thickness of 79 mm and plastic scintillators. For $|\eta| < 1.6$, the granularity is the same as in the barrel part, and for larger $|\eta|$, it is about 0.17×0.17 in $\eta \times \phi$. The thickness is about 10 interaction lengths, including the ECAL.

The outer calorimeter consists of 1–2 scintillator layers at $r = 3.82$–$4.07\,\mathrm{m}$, increasing the minimal thickness to 11.8 interaction lengths. The forward calorimeter is designed to endure the large radiation dose. Quartz fibres are chosen as active medium, which are also sensitive to electromagnetic radiation, allowing to measure electromagnetic energy also out of the ECAL boundaries of $|\eta| < 3$. As absorber, 5 mm thick steel plates are used, resulting in a weight of 108 t. The granularity is approximately the same as in the high-η endcap part.

The hadronic energy resolution in the barrel region of the ECAL and HCAL combined is given as

$$\left(\frac{\sigma}{E}\right)^2 = \left(\frac{85\%}{\sqrt{E[\,\mathrm{GeV}]}}\right)^2 + (7\%)^2$$

and is larger by about one to two orders of magnitudes than the energy resolution of the ECAL [75].

Solenoid

Momenta of charged particles are measured using the curvature of the particle tracks. As the momentum resolution for high-energy particles is limited by the measurement accuracy of the curvature of their tracks, a superconducting magnet provides a strong magnetic field of 3.8 T. The magnet consists of a four-layer winding made from a stabilized reinforced NbTi conductor. An iron yoke is used to return the magnetic flux, which is embedded in the muon system.

Muon system

The muon system is the outermost part of the CMS detector and consists of three detector types: Barrel drift tubes (DT), cathode strip chambers (CSC), and resistive plate chambers (RPC). The DT consists of 172 000 sensitive wires in four cylindric station layers, located in $|\eta| < 1.2$. The length of each wire is around 2.4 m, and the transverse dimension of the Ar/CO_2-filled drift cell is 21 mm. The CSC covers $0.9 < |\eta| < 2.4$, where a higher muon rate is expected and the magnetic field is non-uniform. Six stations contain in total about 2 million wires. The wires are perpendicular to the beam axis, causing the pitch to widen from 8.4 mm to 16 mm. The flux-return yoke is used as absorber material. Both of the subdetectors can be used to trigger events, but to assign the signal to the correct bunch crossing, the RPC is used, which is embedded in the DT and CSC. The momentum resolution for muons with $p_T = 1$ TeV is around 5%, if the inner tracker is included in the track fit.

Trigger system

Beam crossings happen every 25 ns, and with a typical event size of 0.5 MB, this would lead to a data stream of about 20 PB/s, which is not recordable with today's technology. To reduce the data rate, a two level trigger system is used to select events of possible interest [76, 77].

The first level trigger (L1) is a configurable hardware system, which filters events based on object candidates from local structures, and reduces the event rate from 40 MHz to around 100 kHz. The calorimeters are subdivided in trigger towers with an $\eta \times \phi$-coverage of 0.087×0.087 for $|\eta| < 1.74$, corresponding to 5×5 ECAL crystals. For larger $|\eta|$, the towers have a larger extent. Electromagnetic objects are built from clusters of 3×5 ECAL crystals in η-ϕ around a local maximum. Loose shower shape criteria are applied, and the energy in the HCAL in the same η-ϕ region must be small compared to the energy of the ECAL cluster. Candidates for τ leptons are built from several clusters of electromagnetic objects, and loose shape criteria are required. Jets are built from clusters of 9×9 towers of energy deposit in both ECAL and HCAL around a local maximum. The transverse energies or the transverse vectorial momenta of the jets can be added to compute further variables. Muons are built in three η regions: In the barrel region, in the endcap region, and in an overlapping region, for which all muon detector systems are combined. Events are selected if the transverse momentum of the objects exceeds predefined adaptable thresholds.

The high level trigger (HLT) is a computer farm with approximately 16 000 CPU cores, and reconstructs the events similar to the offline reconstruction. The average output rate of around 1 kHz is limited by the output band width. To select events of various final states, approximately 500 HLT paths are used. The paths run independently of each other, but share common sequences across different paths. Special paths are added to select cosmic muons outside of proton-proton collisions, for collisions with few simultaneous proton-proton interactions, for heavy ion collisions and for commissioning of the detector. In addition, paths for monitoring and calibration are used.

Events with less stringent requirements can be selected using prescaled trigger paths. Only a fraction (the inverse of the prescale) of the events fulfilling the requirement of a L1 or HLT path are saved. The prescale can be adopted to limit the total HLT output rate to a feasible value. As the proton beams lose luminosity due to proton-proton collisions, the event rate at the collision point decreases, and the prescales may be lowered.

3.3 Luminosity

The luminosity is calculated using $\mathcal{L} = \dot{N}/\sigma_{\text{vis}}$ from equation 3.1, where $\dot{N} = \langle N_{\text{cluster}} \rangle f_{\text{rev}}$ is the measured rate of reconstructed clusters of hits in the pixel detector, and σ_{vis} the visible cross section (corrected for acceptance and efficiency) of this process [69, 78].

The visible cross section is measured in Van-der-Meer scans [79]: The beams are separated by $\pm 590\,\mu$m and then moved through one another and the number of pixel clusters $\dot{N}(\Delta x, \Delta y)$ is measured as a function of the beam separation in Δx and Δy. From the width of these distributions, the beam widths Σ_x and Σ_y can be estimated, and the visible cross section can be calculated as

$$\sigma_{\text{vis}} = \frac{2\pi \Sigma_x \Sigma_y \dot{N}(\Delta x_0, \Delta y_0)}{N_1 N_2 f_{\text{rev}}} = (8.513 \pm 0.006)\,\text{b},$$

where $\dot{N}(\Delta x_0, \Delta y_0)$ is the pixel cluster rate for head on collisions and $N_1(N_2)$ the number of particles per beam, measured via the beam current [80, 81]. Several sources of uncertainties are considered, the one with the largest impact being the non-factorizability of the Δx and Δy with a relative uncertainty of 0.9%. The uncertainty in the length scale calibration of the beam-beam separation results in a relative uncertainty of 0.8%. In total, a relative uncertainty of 2.5% is achieved.

The $\dot{N}$ and therefore the integrated luminosity is measured in small blocks of events, with approximately constant instantaneous luminosity corresponding to the events recorded in approximately 20 s. The luminosity integrated over time ($\mathcal{L}_{\text{int}}$) as a function of time is shown in figure 3.6. The LHC delivered collisions corresponding to $40.82\,\text{fb}^{-1}$, of which $37.76\,\text{fb}^{-1}$ were recorded by the CMS experiment. The data are validated, and only data of high quality in all subdetectors are used in the further analysis. The validated data used in this analysis correspond to

$$\mathcal{L}_{\text{int}} = (35.87 \pm 0.90)\,\text{fb}^{-1}. \tag{3.2}$$

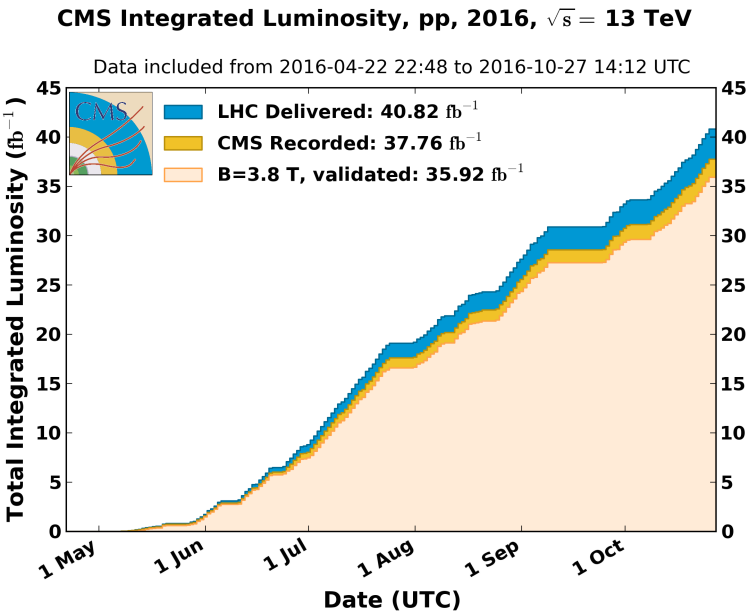

Figure 3.6: Delivered, recorded, and validated integrated luminosity versus time for the data taking in 2016 [70]. The value of the validated luminosity in this plot differs from the luminosity mentioned in the text because an updated luminosity estimation has been used for the latter.

4 Data processing

In this chapter, the event simulation, reconstruction, and event filtering are described.

4.1 Event simulation

Simulated events can be used to study events with the knowledge of the underlying process and decays. They can be used to estimate the yields of SM processes, to test background estimation methods, and to calculate the acceptance for signal models.

Event simulation is done in several steps: Firstly, the hard scattering is generated, taking into account the parton distribution functions (PDF) inside the colliding protons. Secondly, subsequent decays, the fragmentation and the hadronization are simulated. In a third step, simultaneous proton-proton interactions are added, and at last, the response of the detector is simulated.

The total cross section for hadron-hadron collisions is given by the cross section for the hard parton scattering $\hat{\sigma}$, convolved with the PDF $f_i^{\mathrm{p}}(x^{\mathrm{p}}, Q^2)$ for the particle i, depending on the parton's momentum relative to the proton's momentum x^{p} and the scale Q^2. The total cross section to produce the final state C in proton-proton (pp) collisions is given by

$$\sigma(\mathrm{pp} \to C) = \sum_{ij} \int\int f_i^{\mathrm{p}}(x_1^{\mathrm{p}}, Q^2)\, f_j^{\mathrm{p}}(x_2^{\mathrm{p}}, Q^2)\, \hat{\sigma}(ij \to C)\, \mathrm{d}x_1^{\mathrm{p}}\, \mathrm{d}x_2^{\mathrm{p}},$$

where the sum includes all partons inside the proton. The NNPDF 3.0 [82] PDF set is used in LO and NLO, matching the order of event generation. They are fitted to a global data set including HERA-II deep-inelastic inclusive cross-sections, the combined HERA charm data, jet production from ATLAS and CMS, vector boson rapidity and transverse momentum distributions from ATLAS, CMS and LHCb, $W{+}c$ data from CMS and top quark pair production total cross sections from ATLAS and CMS.

The MadGraph5_aMC@NLO 2.2.2 [71] program is used to generate γ+jet, multijet, $(\gamma+)t\bar{t}$, $(\gamma+)W \to \ell\nu$, $(\gamma+)Z \to \nu\nu$, $Z \to \ell\ell$, $\widetilde{g}\widetilde{g}$, and $\widetilde{q}\widetilde{q}$ events. Multijet events are events comprised uniquely of jets produced through the strong interaction. γ+jet events are similar to multijet events, except at least one photon is generated in the hard scattering. The event generation is based on high dimensional integrals, which are computed by the Monte Carlo (MC) method. Several jets may be added to all hard scattering processes to improve the agreement between data[1] and simulation. The event simulation is done in NLO for $\gamma t\bar{t}$ events, and LO for all other processes. To account for higher orders in perturbation theory, all events except for γ+jet and multijet events are weighted to at least NLO cross sections. In this analysis, multijet and γ+jet events are not directly compared to data, so NLO corrections are not necessary.

To minimize the statistical uncertainty in important event topologies, some samples are generated in bins of generated photon p_{T} or $H_{\mathrm{T}}^{\mathrm{gen}}$, where $H_{\mathrm{T}}^{\mathrm{gen}}$ is defined as the scalar sum of the p_{T} of all quarks and gluons in the hard scattering process. Each bin is weighted such that the

[1] Data always corresponds to measured data events and does not include simulation (simulated events).

weighted number of simulated events corresponds to the expected number of events in data. In figure 4.1, the $H_{\mathrm{T}}^{\mathrm{gen}}$ distribution is shown for the γ+jet and $W(\ell\nu)$+jet samples after selection on the reconstructed transverse momentum activity. No discontinuity is observed, indicating that the relative normalization is correct. The reduction of the statistical uncertainty is best illustrated at the transition for the $W(\ell\nu)$+jet sample at $H_{\mathrm{T}}^{\mathrm{gen}} = 2500\,\mathrm{GeV}$. The cross sections and the sample segmentations are shown in appendix A.1.

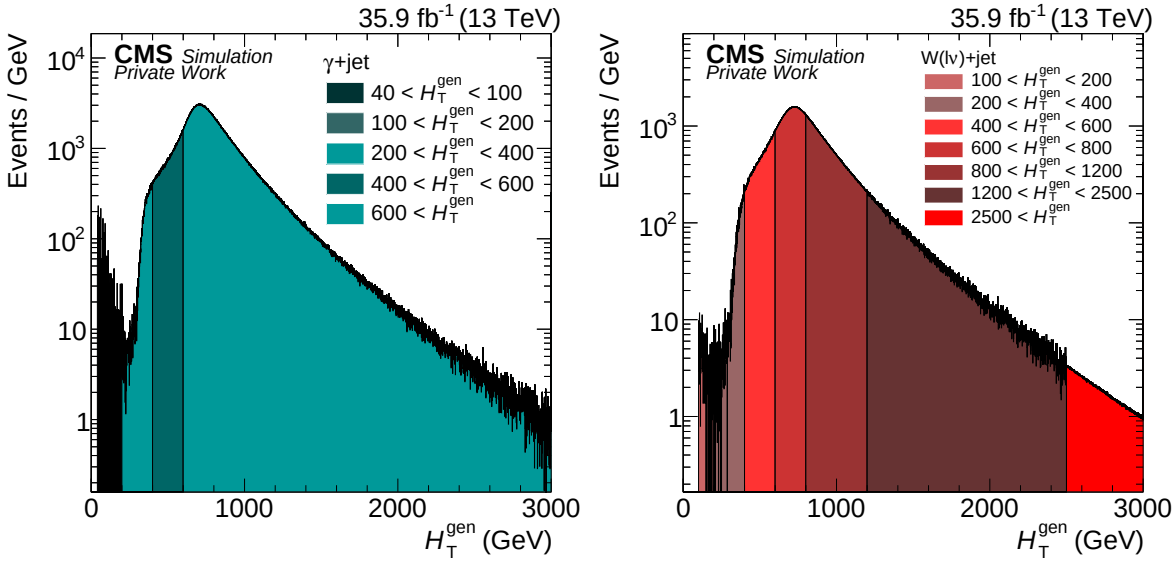

Figure 4.1: The $H_{\mathrm{T}}^{\mathrm{gen}}$ distribution for γ+jet (left) and $W(\ell\nu)$+jet (right) events. A selection is made on the reconstructed transverse momentum activity, suppressing events at lower values of $H_{\mathrm{T}}^{\mathrm{gen}}$. The colors indicate different samples. A bin width of 1 GeV is used, which results in large statistical fluctuations in less populated phase space.

The fragmentation, hadronization, and in case of signal events the decay of the gluinos and squarks is generated using the PYTHIA 8.1 [83] program. The underlying event and multiple parton interactions are simulated using the CUETP8M1 generator tune [84]. The overlap between additional jets simulated in the hard scattering and radiated jets of the parton shower is removed with the MLM method [85] for LO processes and with the FXFX method [86] for NLO samples.

There are several simultaneous proton-proton interactions (in-time pileup) in each bunch crossing due to the large amount of protons in each bunch. In addition, remnants from previous proton-proton bunch crossings can be assigned to later events (out-of-time pileup). Most of these events consist of low-energy multijet events. In addition to the simulated process of interest, several multijet events are added, and the amount of multijet events is weighted to match the amount of pileup events in data. The pileup distribution for data is computed using the total inelastic cross section and the instantaneous luminosity. Figure 4.2 shows the simulated pileup multiplicity for SM and signal simulation, and the pileup multiplicity for data. Signal samples were generated before the data taking and the pileup distribution could only be estimated with a large uncertainty. SM samples were generated at the end of the data taking, and therefore a more appropriate pileup scenario was chosen.

The detector response of SM events is simulated using GEANT4 [87]. In GEANT4, the CMS detector is described by the positions and materials of all detector components, such as the active detector material, the cables, the pipes, or the mounting structures. A large library of different models and measurements for the interactions of various particles and materials is used to simulate the interaction of particles with the CMS detector. For each iteration of the

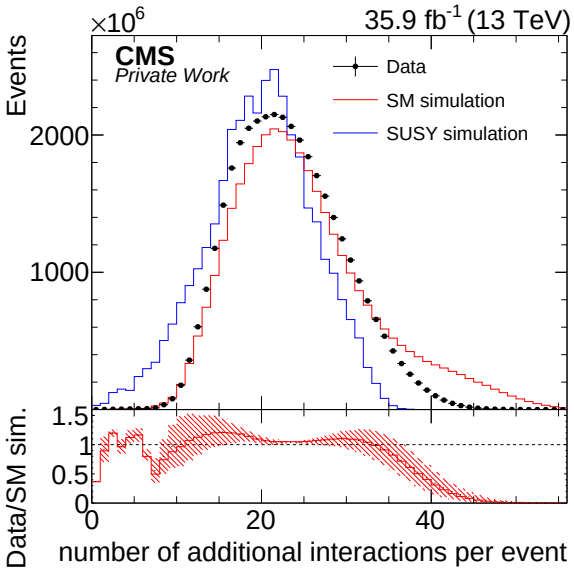

Figure 4.2: Distribution of simulated and measured pileup interactions. The bottom panel of the figure shows in addition the ratio of the measured and simulated distributions with the total inelastic cross section modified by its relative uncertainty of ±5%. Only the ratio to the pileup distribution for SM samples is shown.

algorithm, particles are either propagated to their next location, they decay, or they interact with the detector, producing new particles, which are further propagated in the next iteration of the program.

For signal simulation, large numbers of events for different models are more important than the accuracy of the simulation, and therefore the FastSim [88, 89] program is used. The detector geometry is simplified, and the particle interactions are parametrized. The geometry of the tracking system is approximated by nested layers of cylinders. The thickness of the layers is chosen such that the probability of an interaction is the same as for the Geant4 simulation. Showers in the calorimeters are simulated using the Grindhammer parametrization [90, 91]. As the Grindhammer parametrization was developed for electrons, photons undergo electron-positron pair production at their first interaction with the ECAL. The longitudinal, transversal, and radial shower shapes are parametrized depending on material constants estimated using Geant4 simulation. Within the shower shape, hits are simulated and matched to the corresponding crystals. Energy loss due to gaps and cracks between the crystals and energy leakage into other crystals is considered. The time of the energy deposition is calculated by dividing the distance of the crystal to the origin of the CMS detector by the speed of light. The energy deposited in the ECAL crystals may be modified depending on the position of the crystal to improve the agreement with the Geant4 simulation. The corrections are derived by scaling the uncorrected simulated energy to the energy of crystals in Geant4 for the same processes [92]. For the HCAL, the Grindhammer parametrization for sampling calorimeters is used. Only multiple scattering and the energy loss by ionization are simulated for muons. Simulated hits are positioned at the crossing of muons with muon chambers. For prompt muons, this results in a good agreement between FastSim and the Geant4 simulation. In total, the computing time for the FastSim simulating is reduced by a factor of 10 to 100 comparing to the Geant4 simulation. The agreement of the simulation of main variables with both simulation packages is monitored.

4.2 Event reconstruction

To improve the object resolution, the inner tracking system is aligned using cosmic ray and collision data [93]. The energy depositions in the calorimeters are calibrated to improve the energy resolution [94].

The particle flow (PF) algorithm [95] is used for a global event description of simulated and measured events. Track pieces and calorimeter clusters are reconstructed in each subdetector separately, and are linked to reconstruct all particles in each event without double counting. The resolution of quantities extracted from the calorimeters is improved by using the more accurate momentum measurement in the tracker for particles both reconstructed in the tracker and calorimeters. In addition, this approach allows the efficient reconstruction of photons which undergo pair production in the tracker.

The reconstruction of tracks in the inner tracking system is done iteratively using the combinatorial track finder algorithm [72]. It starts with the clustering of two or three hits in the pixel detector to "pixel-seeds". The ones with three hits are then used to seed high-p_{T} tracks with tight quality criteria. Eight further iterations with looser track quality criteria are run subsequently, in which hits associated to tracks by one of the previous iterations are not used by the subsequent iterations. Tracks which could be electron tracks are refitted using a Gaussian-sum filter (GSF), taking bremsstrahlung into account. Hits in the muon detectors are combined to *standalone muons*. Tracks in the inner tracking system are matched to the standalone muons, and the hits from the inner tracking systems and in the muons system are fitted to reconstruct *global muons*. Each track from the inner tracking system with $p_{\mathrm{T}} > 0.5\,\mathrm{GeV}$ and $p > 2.5\,\mathrm{GeV}$ is also propagated to the muon system, and if there are fitting hits, the muon candidate is called *tracker muon*.

In the calorimeters, cells exceeding a threshold energy with their four directly neighbouring cells (HCAL) or eight diagonal and directly neighbouring cells (ECAL) are used as seed cluster. This seed cluster is expanded with further neighbouring cells, if the energy in these cells exceeds a second threshold. The energy distribution of the cluster is assumed to originate from several sources with different energies. In the next step, an expectation-maximization fit is performed to find the energy and position of each source, assuming a Gaussian distribution of the energy for each source.

Geometrically matching objects are then linked together to reduce the number of combinations. This decreases the computing time of the next step. As muons have the cleanest signal, they are reconstructed first. Additional tracks and energy deposits fitting the muon candidate are assigned to the muon candidate. Their tracks in the muons system, inner tracker and energy deposits in the calorimeters are not considered for the reconstruction of further particles. Next, the electron and photon reconstruction follows, and the corresponding tracks and ECAL and preshower energy clusters (including the ones from bremsstrahlung photons for electrons and e^+e^- tracks in case of photon conversion) are also ignored in further reconstruction steps. All residual elements are reconstructed as charged hadrons, neutral hadrons and photons from fragmentation of jets. In the post-processing step, the events are checked for possible misreconstructed or misidentified particles, for example cosmic muons which are reconstructed as two muons originating from the collision point and flying in opposite directions.

To reconstruct vertices, high-quality tracks from charged particles are selected and a deterministic annealing algorithm is used to cluster the tracks to vertices [72,96]. The positions of the vertices are determined from a fit to the track clusters. If more than four tracks are used in the fit, and the position of the vertex is consistent with the luminous region defined by $r < 2\,\mathrm{cm}$ and $|z| < 24\,\mathrm{cm}$, it is denoted as good primary vertex. With a vertex reconstruction efficiency

of 70% (100%) for pileup (hard scattering) vertices, the average number of good primary vertices N_{PV} is about 23 in the data recorded in 2016. The primary (hard scattering) vertex is defined as the vertex with the largest $\sum p_{\mathrm{T}}^2$, where the sum includes all tracks assigned to the vertex under consideration. All other vertices are denoted as pileup vertices.

Jets are reconstructed by sequentially clustering particles with the anti-k_t algorithm [97]. The anti-k_t algorithm is collinear and infrared safe, meaning that it is e.g. invariant under the emission of collinear or soft gluons [98]. In each step, the two input objects i and j with the smallest distance d_{ij} are merged. If the smallest d_{ij} is equal to the distance to the beam d_{iB}, the object i is called a jet and removed from the list of objects. The algorithm proceeds until all objects are clustered to jets. The distance between objects is defined by

$$d_{ij} = \min\left(p_{\mathrm{T},i}^{2p}, p_{\mathrm{T},j}^{2p}\right)\frac{\Delta R^2}{R^2}$$

and the distance to the beam by

$$d_{iB} = p_{\mathrm{T},i}^{2p},$$

where the parameter R governs the typical size of a jet and is 0.4 in this analysis, and p determines the relative power of the energy versus geometrical scales. The k_t algorithm [99] is defined by $p = 1$, the Cambridge/Aachen algorithm [100,101] is defined by $p = 0$, and the anti-k_t algorithm (used in this analysis) by $p = -1$. The time complexity of the anti-k_t algorithm is $\mathcal{O}\left(N^{3/2}\right)$ for N input objects. In this analysis the FastJet 3.0.1 [102] implementation is used, resulting in a computing time similar to the one of the k_t algorithm with a time complexity of $\mathcal{O}(N\ln(N))$ for $N < 20\,000$ input objects.

The anti-k_t algorithm is used to cluster particle candidates reconstructed with the PF algorithm, but omitting charged particles associated to pileup vertices [103]. Omitting these charged particles is called charged hadron subtraction (CHS). To improve the jets' resolution and to correct for remaining pileup effects, the raw jet momentum $p_{\mathrm{T}}^{\mathrm{raw}}$ is corrected by a product of sequentially applied scale factors:

$$p_{\mathrm{T}} = C_{\mathrm{pileup}}(p_{\mathrm{T}}^{\mathrm{raw}}) \cdot C_{L2L3}(p_{\mathrm{T}}^{\text{pu corr}}, \eta) \cdot C_{\mathrm{Residual}-\eta}(\eta) \cdot C_{\mathrm{Residual}-p_{\mathrm{T}}}(p_{\mathrm{T}}^{L2L3})\, p_{\mathrm{T}}^{\mathrm{raw}}$$

The pileup correction C_{pileup} is determined from simulated multijet events processed with and without additional pileup interactions. They are parameterized as a function of the energy density (ρ), the jet area A, η, and $p_{\mathrm{T}}^{\mathrm{raw}}$. The ρ is the median energy of cells in a η-ϕ grid. No lower momentum or energy cutoff is used. By using the median instead of the mean, the hard scattering jets do hardly contribute, and ρ is dominated by multiple low-energy pileup energy deposits. To correct for pileup differences in data and simulation, the pileup offset in p_{T} is also measured using the random cone method [104]. To do so, low-energy multijet events recorded with triggers that select random events without requirements on the physics objects are used. In these events and in pileup simulation, jet cones are randomly distributed in the η-ϕ plane. The p_{T} of these jets corresponds to the pileup offset and is shown in figure 4.3 (left). The ratio of the measured to simulated pileup offset is used to correct jets in data.

The response correction C_{L2L3} ensures that the reconstructed momentum corresponds closely to the generated momentum. In simulation, all stable generated particles with a decay length of at least 1 cm, excluding only weakly interacting particles, are clustered to jets using the anti-k_t algorithm with a distance parameter of 0.4 and matched to the reconstructed jets. Correction factors depending on the pileup corrected transverse momentum $p_{\mathrm{T}}^{\text{pu corr}}$ and η are taken from multijet simulation, such that the p_{T}^{L2L3} of the corrected reconstructed jets is the same as the generated jet $p_{\mathrm{T}}^{\mathrm{gen}}$. Figure 4.3 (right) shows the simulated jet energy response (ratio between reconstructed and generated jet p_{T}) as a function of $|\eta|$ for various values of

p_T. For data, two residual corrections $C_{\text{Residual}-\eta}$ and $C_{\text{Residual}-p_T}$ are applied to eliminate differences between data and simulation. Firstly, events with one central jet in $|\eta| < 1.3$ and one additional jet are selected, and the response of the additional jet is corrected relative to the central jet, depending on η. Secondly, p_T-depending corrections are estimated using $Z(\mu\mu)$+jet, $Z(ee)$+jet, and γ+jet events. For simulated jets, the residual corrections are $C_{\text{Residual}-\eta} = C_{\text{Residual}-p_T} = 1$.

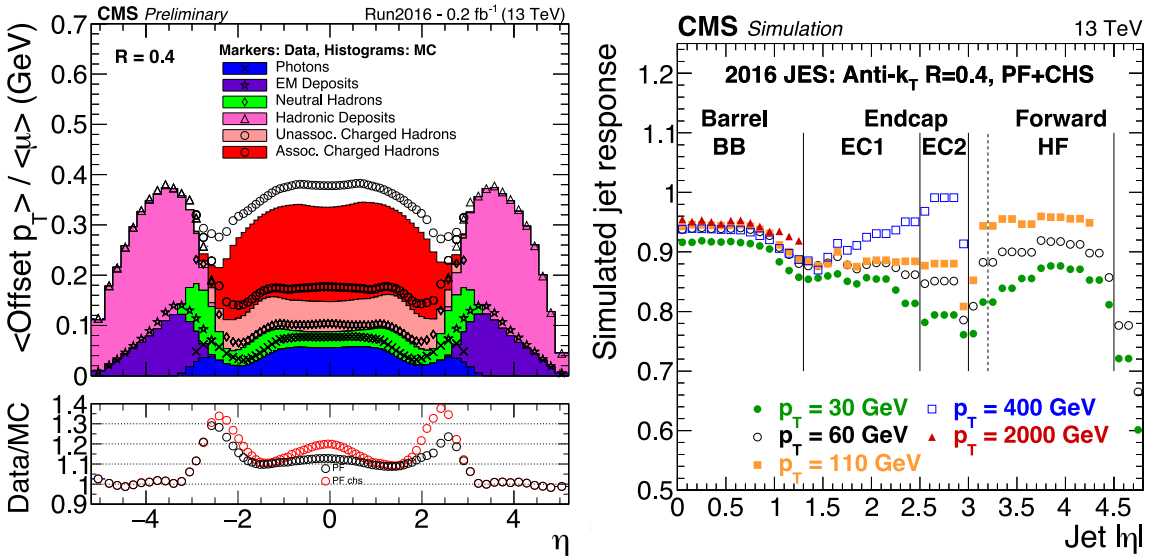

Figure 4.3: Left: The pileup jet correction per additional interaction as a function of η [105]. For CHS jets, the pileup corrections would be much larger (black circles and dark-red histogram). Right: The simulated jet response as a function of $|\eta|$ for various p_T [105]. In this figure the endcap part which overlaps with the acceptance of the tracker is denoted as EC1, while the endcap part which does not overlap with the tracker is denoted as EC2.

The jet energy resolution is shown in figure 4.4 as a function of p_T for different number of additional vertices. For $p_T \approx 30\,\text{GeV}$, it is about 15–26%, while for $p_T \approx 100\,\text{GeV}$, it ranges from 10 to 12%.

Jets are also required to fulfill some loose identification criteria to suppress objects which do not origin directly from strong interacting particles [106]: For $|\eta| < 2.7$, they must consist of two or more particles, and both the neutral hadron and neutral electromagnetic energy fraction must not exceed 99%. For $|\eta| < 2.4$, jets must also have a charged component, and the energy fraction from electrons must be below 99%. For jets in $2.7 < |\eta| < 3.0$, there have to be at least three particles, and the neutral electromagnetic energy fraction is not allowed to exceed 90%.

The missing transverse momentum $\vec{p}_T^{\,\text{miss}}$ is defined as negative vectorial sum of the $\vec{p}_T$ of all reconstructed particles. Its resolution is improved by propagating the jet energy corrections:

$$\vec{p}_T^{\,\text{miss}} = \vec{p}_{T,\text{uncorrected}}^{\,\text{miss}} + \sum_{\text{jet } i} \vec{p}_{T,\text{uncorrected}}^{\,i} - \sum_{\text{jet } i} \vec{p}_{T,\text{corrected}}^{\,i}$$

All jets with $p_T > 10\,\text{GeV}$ and an electromagnetic energy fraction smaller than 90% are considered for the correction. Jets with a large electromagnetic energy fraction have usually different jet energy corrections compared to average jets and would therefore lead to artificial $\vec{p}_T^{\,\text{miss}}$. The magnitude of $\vec{p}_T^{\,\text{miss}}$ is denoted as p_T^{miss}.

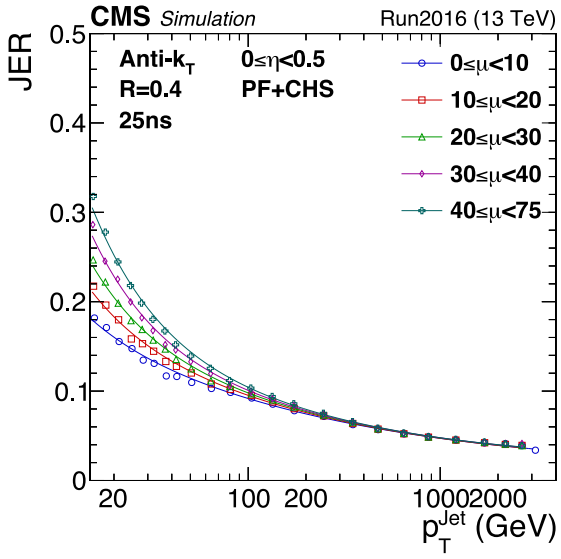

Figure 4.4: Jet energy resolution for $0 \leq \eta < 0.5$ as a function of p_T for different number of pileup vertices μ [105].

Jets can also be reconstructed from ECAL and HCAL energy depositions. As they lack any track information, these calorimetric jets have a worse energy resolution, they cannot be assigned to a primary or secondary vertex, and the charged energy fraction cannot be determined.

Detector- and machine-induced background events are identified and removed by several event filters [107]: Beam halo (upstream proton-proton collisions) produces calorimeter deposits and often a track in the muon chambers at constant ϕ parallel to the beam axis. The position, energy deposits and the timing information is used to reject such events. Noise in the HCAL electronics and direct particle interactions with the HCAL light fibres can lead to spurious energy deposits which are filtered using the timing and the pulse shape information or by combining tracking with ECAL and HCAL information. Five ECAL endcap supercrystals with anomalously large energies in several channels are masked. If the crystal-by-crystal readout is unavailable for some ECAL trigger towers, the energy calculated by the trigger is used. However, the trigger information saturates above 127.5 GeV, so events where such saturations occur are filtered out. Low-quality muon tracks can be identified as high-momentum charged hadrons, and are filtered based on the purity of the reconstructed tracks and the relative p_T uncertainty of the muons. At least one good primary vertex is required for each event. The p_T^{miss} distribution of dijet events is shown in figure 4.5 with and without the filters. Detector- and machine-induced events tend to have extremely large values of p_T^{miss} and can be removed with the filters, leading to a much better agreement of data and simulation. Multijet (QCD) events dominate the region of low p_T^{miss}, while events with neutrinos dominate the high-p_T^{miss} region. In this figure, the electroweak (EWK) processes include $Z \to \ell\ell$, $Z \to \nu\nu$, $W \to \ell\nu$, and diboson simulation. The top quark includes top quark pair production and single top quark production.

For vividness, a simulated single squark event is shown in figure 4.6. The photon p_T is 1.7 TeV, p_T^{miss} is 672 GeV, and the three leading jets have transverse momenta of 1560, 630, and 514 GeV, respectively. The photon is also reconstructed as a jet, but for simplicity this jet is not drawn.

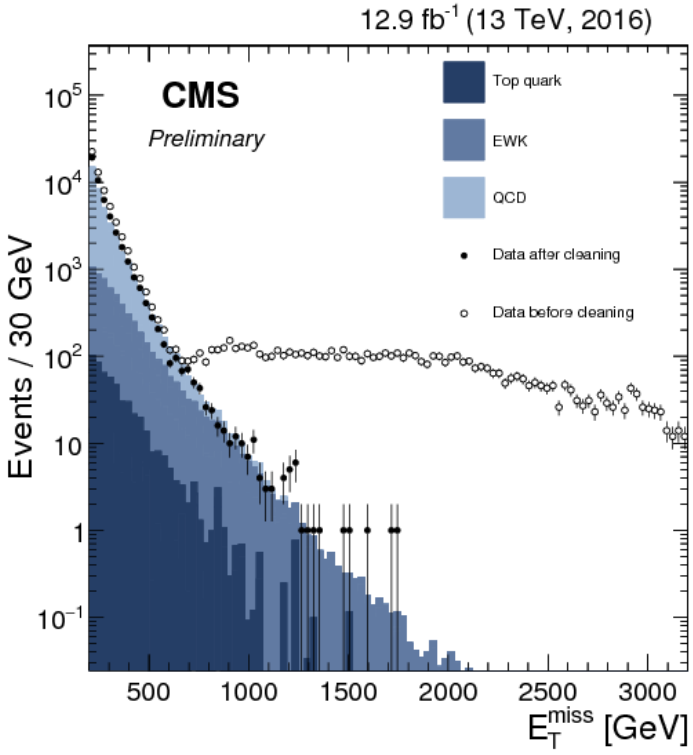

Figure 4.5: Distribution of $p_{\mathrm{T}}^{\mathrm{miss}}$ (denoted as $E_{\mathrm{T}}^{\mathrm{miss}}$) in dijet events with (filled markers) and without (open markers) cleaning algorithms applied, and from simulation (filled histograms) [107].

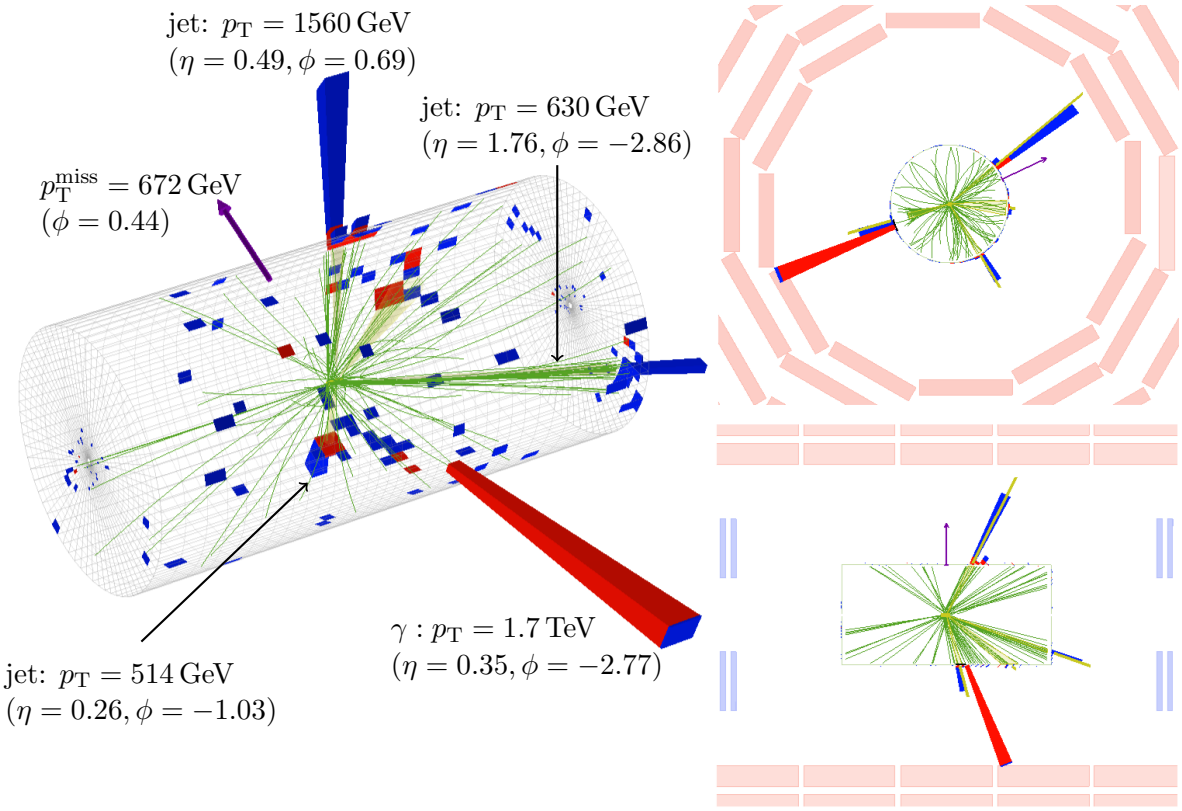

Figure 4.6: Display of energy depositions in the ECAL (red cuboid), energy depositions in the HCAL (blue cuboid), tracks (green lines), vertices (yellow dots), p_T^{miss} (purple arrow), and jets (yellow cones). The left plot shows a tree-dimensional representation of the CMS detector, the top right plot shows the x-y plane, and the bottom right plot shows the x-z plane. The front surface of the ECAL is displayed as grid, and the muon chambers as red and blue rectangles (right plots only). The size of the boxes corresponds to the amount of deposited energy.

4.3 Particle identification and variable definitions

The PF algorithm reconstructs particle candidates as inclusively as possible, such that the reconstruction efficiency but also the misidentification probability are very large. Hence, particles can be reconstructed simultaneously as several object candidates. An electron, for example, is usually reconstructed as electron candidate, photon candidate, and jet candidate. It is analysis dependent for which object types the selection efficiency is maximized. In this analysis, first photons are identified, and all other object candidates that are matched to the photon are rejected in the further analysis.

Photons

To discriminate photons from jets or electrons, several identification variables are defined:

Hadronic energy fraction H/E: Photons mainly deposit their energy in the ECAL. Hadrons deposit a part of their energy in the HCAL, so the energy in the HCAL towers directly behind the ECAL cluster of the photon object (H) divided by the energy of the photon (E) is small for real photons.

Shower width $\sigma_{i\eta i\eta}$: The magnetic field points in z-direction, bending charged particles in ϕ-direction. The shower width in η is unaffected by the magnetic field, and is used to discriminate photons from neutral hadrons, which deposit their energy in a larger cone. It is derived from the 5×5 ECAL crystals (index i) surrounding the crystal with the largest energy deposit. Quadratic differences between the mean cluster position $\langle\eta\rangle$ and the position of the considered crystal η_i are weighted by an energy dependent weight $w_i = \max\left(0, 4.7 + \ln\frac{E_i}{E_{5\times5}}\right)$:

$$\sigma^2_{i\eta i\eta} = \frac{\sum_i^{5\times5} w_i \left(\eta_i - \langle\eta\rangle\right)^2}{\sum_i^{5\times5} w_i}$$

The weight ensures that crystals which contain less than 0.9% of the cluster energy are not considered in the calculation.

Isolation $I_\pm, I_0, I_\gamma$: The transverse momenta of charged hadrons consistent with the primary vertex, neutral hadrons, and photons (excluding the considered photon) within a cone of $\Delta R < 0.3$ around the photon are summed up and define the charged hadron isolation $I_\pm$, the neutral hadron isolation I_0, and the photon isolation I_γ, respectively. The isolation values I_0 and I_γ are corrected for contributions from pileup events by subtracting the effective area times ρ from the isolation values. The effective area depends on η and is estimated using γ+jet events. The charged hadron isolation is not corrected for pileup as the particles taken into account originate from the primary vertex.

Most of the prompt photons are isolated, meaning that they have low isolation values, while photons radiated in jets are produced alongside other particles, leading to larger isolation values.

Number of pixel-seeds $N_{\text{pixel-seed}}$: The hadronic response and the isolation are similar for photons and electrons. In contrast to photons, electrons produce hits in the pixel detector. Photons are required to be reconstructed without matching pixel-seeds.

The range in pseudorapidity is restricted by the geometry of the detector. To compute shower shapes, it is required that the photon is separated at least two crystals from the ECAL boundaries. To effectively discriminate photons from electrons, information from the pixel detector is required, defining the maximal pseudorapidity. The thresholds on the identification variables are studied on simulated photon and jet samples, and were tuned to have a high signal efficiency and a high background rejection. The background rejection is defined as one minus

the efficiency that a photon candidate with very loose identification criteria (geometrically matched to a generated jet) is falsely selected as a photon. In addition the thresholds are chosen such that the efficiency and background rejection are constant with respect to p_T, η, and other variables. For this analysis, the "loose" working point with a high signal efficiency of 91% and a moderate background rejection of 83% is chosen. The thresholds of this working point are shown in table 4.1.

Table 4.1: Upper thresholds on photon identification variables.

	EB ($|\eta| < 1.4442$)	EE ($1.566 < |\eta| < 2.5$)
H/E (%)	5.97	4.81
$\sigma_{i\eta i\eta}$	0.01031	0.03013
$I_{\pm}$ (GeV)	1.295	1.011
I_0 (GeV)	$10.910 + 1.48\frac{p_T}{100\,\text{GeV}} + 0.17\left(\frac{p_T}{100\,\text{GeV}}\right)^2$	$5.931 + 1.63\frac{p_T}{100\,\text{GeV}} + 0.14\left(\frac{p_T}{100\,\text{GeV}}\right)^2$
I_γ (GeV)	$3.630 + 0.47\frac{p_T}{100\,\text{GeV}}$	$6.641 + 0.34\frac{p_T}{100\,\text{GeV}}$
$N_{\text{pixel-seed}}$	0	0

The performance of the photon reconstruction is studied using $Z \to \mu\mu \to \mu\mu\gamma$ events [108]. This final state is selected with high purity by requiring $70 < m(\mu\mu\gamma) < 110\,\text{GeV}$, $m(\mu\mu\gamma) + m(\mu\mu) < 180\,\text{GeV}$, and $0.1 < \Delta R(\mu, \gamma) < 0.8$. The data compared to simulation for several variables are shown in figures 4.7 and 4.8. The number of events with high photon p_T reconstructed in the barrel is slightly underestimated by the simulation. In the following, p_T and η depending scale factors are applied to simulation as will be discussed in section 5.4.1. The simulated $\sigma_{i\eta i\eta}$ is shifted downwards by about 0.001 with respect to the data. For most events H/E, $I_{\pm}$, and I_0 are zero. For larger values, these variables are described reasonably by the simulation.

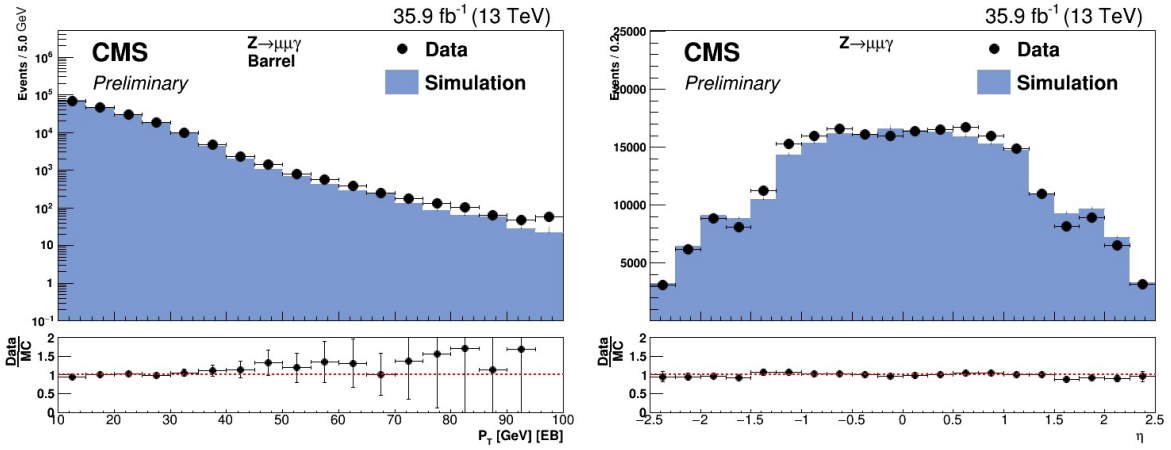

Figure 4.7: Distributions of p_T and η for photons in data and simulation [108]. The nomenclature in the figures is adopted to match the one in this thesis.

Electrons

In this analysis, two methods are used to reconstruct electrons: Firstly, electrons can be reconstructed similarly to photons, except that at least one pixel-seed is required. This leads to objects which are very similar to photon objects, but lack a high signal efficiency and lack good momentum resolution for candidates with small momenta.

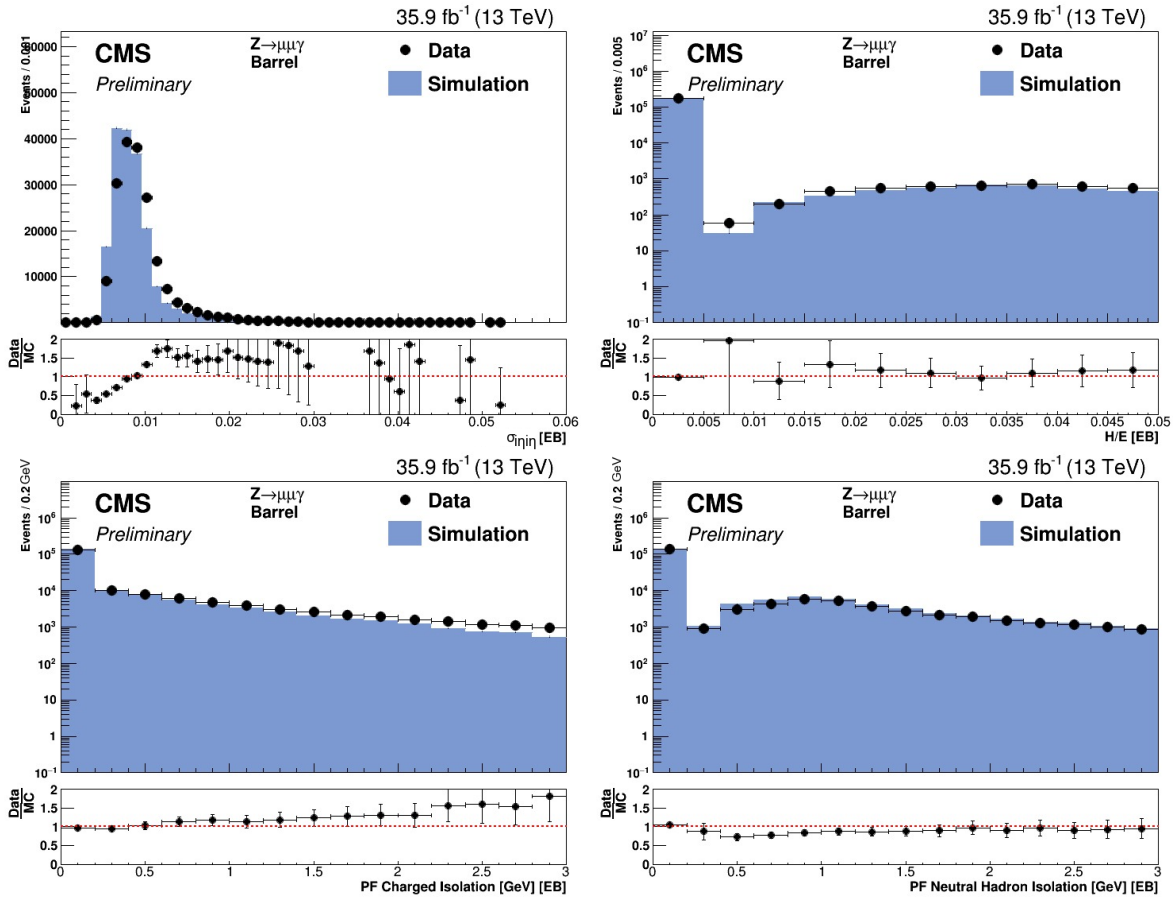

Figure 4.8: Distributions of $\sigma_{i\eta i\eta}$, H/E, $I_{\pm}$, and I_0 for photons in data and simulation [108]. The nomenclature in the figures is adopted to match the one in this thesis.

Secondly, electrons can be reconstructed from PF electron candidates, where the GSF track fit is combined with an energy deposition in the ECAL. To ensure a low background contribution from other objects, strict cuts are made on the identification variables defined above, as well as additional variables sensitive to the track and the matching of the track to the ECAL cluster. The signal efficiency is about 70%, while the background rejection with respect to non-prompt electrons is about 99.9%. These electrons are called GSF electrons throughout this thesis.

Muons

All tracks identified as global muons or tracker muons by the PF algorithm are used as muons. This ensures a very efficient reconstruction of muons.

Transverse event activity

All jets with $p_{\mathrm{T}} > 30\,\mathrm{GeV}$ and $|\eta| < 3$ are selected, and their scalar p_{T} is added to define the transverse event activity H_{T}^{γ}. In case a photon as defined above with $p_{\mathrm{T}} > 100\,\mathrm{GeV}$ is found in the event, the photon p_{T} is included instead of the matching jet. Electrons, taus, and other objects can be reconstructed as jets as well, and thus are included in H_{T}^{γ} as well. This definition is therefore similar to the definition of H_{T}^{γ} in the HLT.

The SUSY particles targeted in this analysis are heavy, and deposit most of their energy through decay products in the detector. H_{T}^{γ} is therefore expected to be higher than for SM processes.

4.4 Online event selection

To select events resulting from SUSY signal processes, the *photon-H_{T}^{γ} trigger* is used. Events are selected by the L1 trigger if at least one electromagnetic object with $p_{\mathrm{T}} > 36$ or 40 GeV, depending on the instantaneous luminosity, is reconstructed. At the HLT, a simplified version of the PF algorithm is used to cluster the energy in the ECAL [109]. Events in which no reconstructed cluster can be geometrically matched to the corresponding L1 cluster are rejected. In addition, at least one cluster must exceed $p_{\mathrm{T}} > 90$ GeV. In the next step, the cluster shape variable $\sigma_{i\eta i\eta}$ is computed for each cluster. Events are rejected if there is no cluster with $\sigma_{i\eta i\eta} < 0.014\,(0.035)$ for EB (EE). In a next step, photons are also required to have less than 15%(10%) of their EB (EE) ECAL energy reconstructed in the hadronic calorimeter in the same η-ϕ region.

After an event passes the photon filter, the transverse event activity is computed. Calorimetric jets are reconstructed from calorimeter clusters, and their scalar p_{T} is added for jets with $p_{\mathrm{T}} > 30$ GeV and $|\eta| < 3$. This transverse momentum sum must exceed 400 GeV, before a simplified version of the PF algorithm is used to reconstruct particle flow jets. Like in the offline reconstruction, jets must fulfill loose identification criteria and their momenta are corrected. However, the jet transverse momentum corrections differ slightly between the offline and trigger reconstruction due to an improved calibration for the offline reconstruction. Again, the transverse momentum sum is computed using jets with $p_{\mathrm{T}} > 30$ GeV and $|\eta| < 3$, but this time it must exceed 600 GeV. Due to the requirement of the calorimetric transverse event activity, the PF track reconstruction is only done for a fraction of the events, reducing the confined computing time. No information about the photon enters the computation of the transverse event activity reconstruction on trigger level, and as the photon is clustered in a jet in most of the cases, it is mostly also added to the transverse event activity.

To select events not necessarily containing photons, the H_{T}^{γ} *trigger* is used, based on an H_{T}^{γ} requirement only. Events with 160, 200, 220, 240, 255, 270, 280, 300, or 320 GeV of transverse event activity on L1 are passed to the HLT. All of these triggers are strongly prescaled. The threshold is adjusted to the instantaneous luminosity. The HLT algorithm is the same as for the H_{T}^{γ} requirement of the trigger described above and events with $H_{\mathrm{T}}^{\gamma} > 600$ GeV are selected.

To study the trigger efficiency of the photon-H_{T}^{γ} trigger, the *photon trigger* is used, which selects events similar to the photon-H_{T}^{γ} trigger, except that instead of an H_{T}^{γ} requirement, the trigger is prescaled.

For the background estimation, the *electron trigger* is used to select events induced by the $Z \to ee$ process. At L1, the event has to pass at least one of more than 20 filters, each selecting events with at least one electromagnetic object with p_{T} larger than 22 to 36 GeV. At the HLT, energy clusters in the ECAL are reconstructed, and events with at least one cluster with $p_{\mathrm{T}} > 27$ GeV and $|\eta| < 2.1$ are kept. Similarly to the photon reconstruction at HLT, the shower shape $\sigma_{i\eta i\eta}$ and the hadronic activity in the same η-ϕ region relative to the ECAL cluster energy are required to be small. To even lower the trigger rate, restrictions on the three isolation values are made at HLT level. First, the ECAL energy in a cone around the ECAL cluster is summed up (ignoring the energy of the ECAL cluster itself) and divided by the ECAL cluster energy. If the ECAL isolation is below a threshold, a similar isolation

calculation is performed using the HCAL energy in a cone around the position of the ECAL cluster, and also here the value must not exceed a threshold. Next, tracks are reconstructed in a cone around the position of the ECAL cluster, using a simplified but faster version of the offline track reconstruction. The sum of the p_T of all tracks in this cone, excluding the track matched to the ECAL shower, is also required to be small. If the ECAL cluster is found to be well isolated, a GSF fit is performed to the track matched to the ECAL cluster, and only events with a good track fit are kept.

The trigger efficiency of all triggers is constantly monitored while data taking as a function of several diagnostic variables like p_T, η, or H_T^γ, allowing to quickly respond to errors during the recording of data. The CMS internal names are given in appendix A.1.

Trigger efficiency

The trigger efficiency is the probability that an event which satisfies the criteria in the offline selection is also triggered by the HLT. For most events, the offline selection is tighter than the selection at trigger level. However, due to different energy corrections and slightly different reconstruction algorithms that are used in the analysis compared to the trigger level, some events are not recorded by a certain trigger path, even if they fulfill the offline requirement for this path. The photon-H_T^γ trigger used to select possible events originating from SUSY has a photon criterion and an H_T^γ criterion. The efficiencies for both criteria are assumed to be independent and are measured individually using data.

To measure the effect of the H_T^γ criterion, events are selected by the photon trigger, which has the same photon requirement as the photon-H_T^γ trigger. The offline selection for photons is applied, and events with at least one photon with $p_T > 100\,\text{GeV}$ are used as baseline selection. Figure 4.9 shows the ratio of the number of events also triggered by the photon-H_T^γ trigger to the number of events in the baseline selection as a function of H_T^γ. The turn-on of the trigger is not sharp, since the objects from which H_T^γ is calculated have different calibrations at trigger level and offline reconstruction. The trigger efficiency and its statistical uncertainty for $H_T^\gamma > 700\,\text{GeV}$ are $(99.93^{+0.04}_{-0.09})\%$.

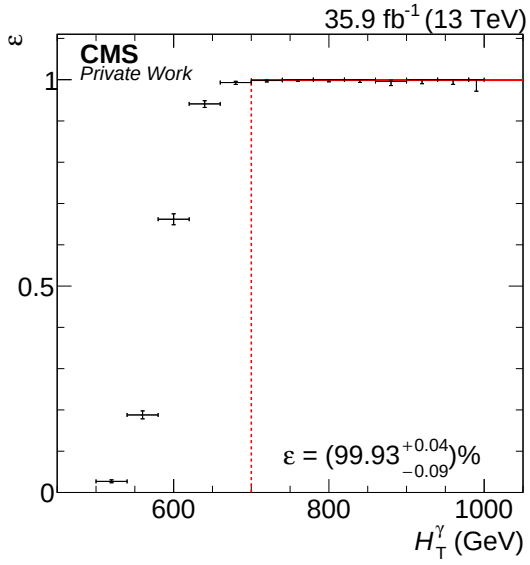

Figure 4.9: The trigger efficiency of the H_T^γ criterion as a function of H_T^γ.

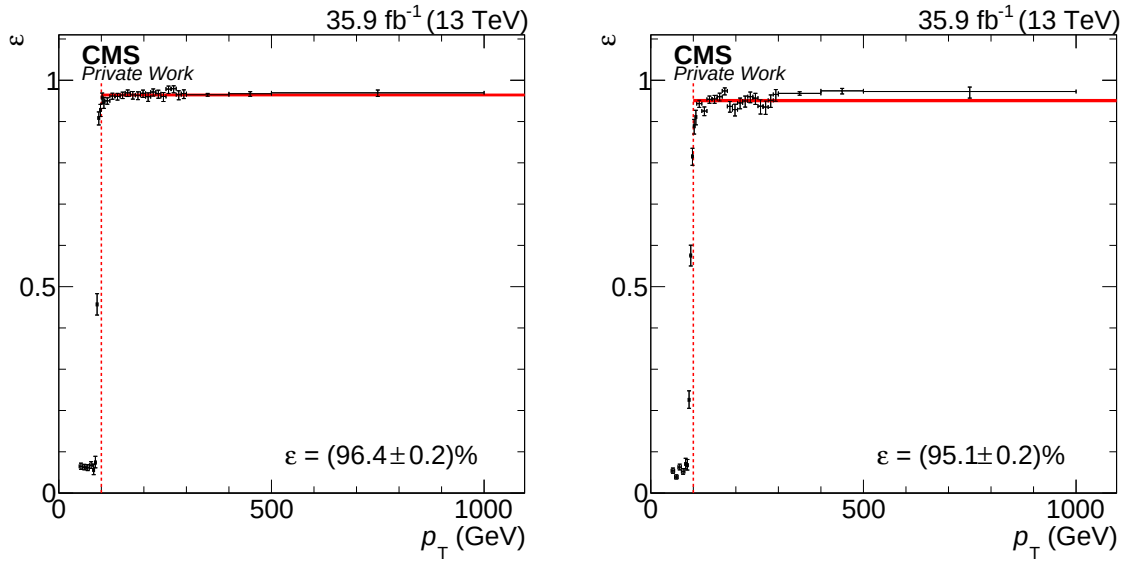

Figure 4.10: The trigger efficiency of the photon part of the trigger as a function of the photon p_{T} for photons reconstructed in the barrel (left) and endcap (right).

The trigger efficiency of the photon criterion of the photon-H_{T}^{γ} trigger is measured in a similar way, using events recorded by the H_{T}^{γ} trigger. At the HLT, H_{T}^{γ} is calculated in the same way as for the photon-H_{T}^{γ} trigger, and the baseline offline selection is defined by requiring $H_{\mathrm{T}}^{\gamma} > 700\,\mathrm{GeV}$. The ratio of the events also triggered by the photon-H_{T}^{γ} trigger to the events in the baseline selection is shown in figure 4.10 as a function of the photon p_{T} in the EB (left) and the EE (right). The trigger efficiencies for photons with $p_{\mathrm{T}} > 100\,\mathrm{GeV}$ in the EB and EE and their statistical uncertainties are $(96.4 \pm 0.2)\%$ and $(95.1 \pm 0.2)\%$, respectively.

The trigger efficiency is found to be independent of all major variables. Figure 4.11 shows the trigger efficiency for events containing at least one photon with $p_{\mathrm{T}} > 100\,\mathrm{GeV}$ and $H_{\mathrm{T}}^{\gamma} > 700\,\mathrm{GeV}$ as a function of $|\eta|$ and $p_{\mathrm{T}}^{\mathrm{miss}}$ for the H_{T}^{γ} baseline selection. The trigger efficiency is independent of these variables. Several other variables are tested, all satisfying the expectation. In figure 4.12, the trigger efficiency versus the run number is shown, covering the data taking period in 2016. Successive runs are combined to decrease the statistical uncertainty. The trigger efficiency is slightly lower in the first quarter of the data taking period.

To cover this effect and remaining turn-on effects an additional relative systematic uncertainty of 4% is assumed. However, the trigger efficiency is capped at a maximum of 100%. The total trigger efficiency for events with a photon with $p_{\mathrm{T}} > 100\,\mathrm{GeV}$ and $H_{\mathrm{T}}^{\gamma} > 700\,\mathrm{GeV}$ is the product of the trigger efficiencies of the H_{T}^{γ} criterion and the photon criterion and is

$$(96.3^{+3.7}_{-3.9})\%$$

for photons reconstructed in the EB and $(95.0 \pm 3.8)\%$ in the EE, respectively. The yields of all simulated samples are weighted according to these efficiencies depending on the pseudorapidity of the reconstructed photon.

4.5 Software

The events selected by the HLT are reconstructed at the Tier-0 computing center at CERN. Copies of the data, as well as simulation, are transferred to various computing centers in the Worldwide LHC computing grid [110, 111]. In this analysis, the reconstruction version

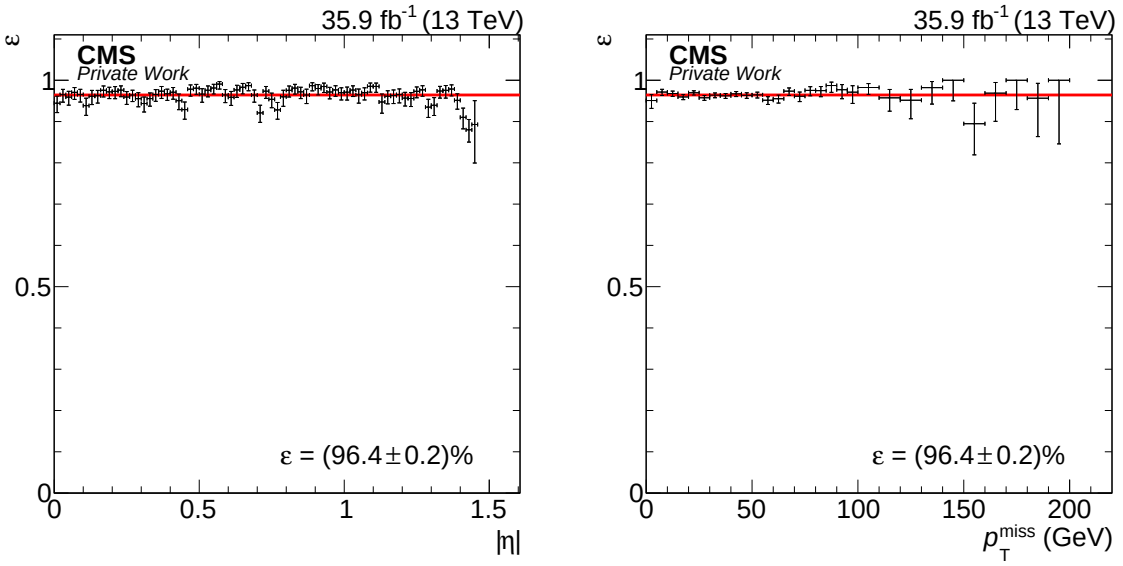

Figure 4.11: Trigger efficiency versus $|\eta|$ of the leading photon (left) and $p_{\mathrm{T}}^{\mathrm{miss}}$ (right).

`03Feb2017` was used, including the latest alignment results, calibrations, and corrections. The data sets used are listed in appendix A.1.

The data are processed with the CMS Software `CMSSW 8.0.26_patch1` [73], using the compacted analysis object data format (`MINIAOD`) [112]. Preselected events are processed using the `ROOT` framework [113, 114]. The preselection is done using the `TreeWriter` software[2], and the last step of filling histograms and plotting them is done using `PyROOT` scripts[3].

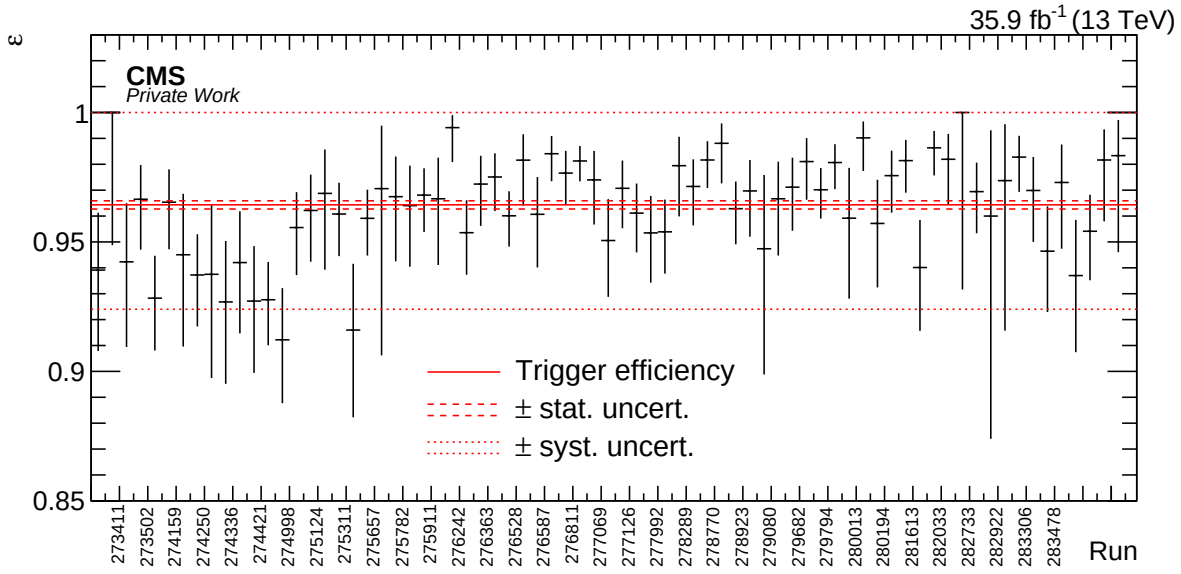

Figure 4.12: Trigger efficiency versus the run number. The trigger efficiency and its statistical and systematical uncertainties (see text) are drawn in addition.

[2] `github:cms-susy-photon-rwth-1b/TreeWriter`
[3] `github:kkiesel/phd`

5 Analysis strategy and background estimation

Six search regions are defined, and in each of them, the observed data are compared to the expected SM background. In the presence of some SUSY or other BSM models, an excess of observed events over the number of predicted SM events is expected. This section describes the estimation of the SM background in the search regions.

5.1 Event selection

Events with at least one photon, reconstructed in the EB with $p_{\mathrm{T}} > 100\,\mathrm{GeV}$, $H_{\mathrm{T}}^{\gamma} > 700\,\mathrm{GeV}$, $p_{\mathrm{T}}^{\mathrm{miss}} > 350\,\mathrm{GeV}$, and $|\Delta\Phi(\vec{p}_{\mathrm{T}}^{\,\gamma}, \pm\vec{p}_{\mathrm{T}}^{\,\mathrm{miss}})| > 0.3$ are selected, where $\vec{p}_{\mathrm{T}}^{\,\gamma}$ is the transverse momentum vector of the leading photon. To further increase the sensitivity, these events are classified into six search regions. The reason for theses selections is discussed in the following.

To be recorded by the HLT, the considered events must have at least one photon with $p_{\mathrm{T}} > 90\,\mathrm{GeV}$ and $H_{\mathrm{T}}^{\gamma} > 600\,\mathrm{GeV}$. To ensure a constant trigger efficiency, $p_{\mathrm{T}} > 100\,\mathrm{GeV}$ is required for the photon and $H_{\mathrm{T}}^{\gamma} > 700\,\mathrm{GeV}$, as discussed in section 4.4. Events are also recorded if the photon is reconstructed in the EE, while in the search regions, a photon is required to be reconstructed in the EB. The separation of real photons and other objects is worse in the EE since the granularity of the ECAL is coarser. In addition, a high energy is needed to pair produce heavy squarks and gluons, so that little energy is available to boost the decaying outgoing particles compared to most SM processes. The particles produced in SUSY events are therefore more central (smaller in $|\eta|$) with increasing squark or gluino mass. Figure 5.1 shows the normalized distribution of the $|\eta|$ of the leading photon for γ+jet, γZ, γW, and two gluino-single-photon scenarios with a gluino mass of 1600 GeV and gaugino masses of 100 and 1500 GeV for events containing at least one photon with $p_{\mathrm{T}} > 100\,\mathrm{GeV}$ and $H_{\mathrm{T}}^{\gamma} > 700\,\mathrm{GeV}$. The ratio of signal over SM events is much larger in the EB than in the EE.

To increase the sensitivity, further selections are applied to the events. Simple and well defined variables allow for an easier reinterpretation of the analysis and an easier understanding of the selected events and the background estimation methods, while complex variables (for example the razor variables [115, 116] or the α_T variable [117, 118]) provide a better discrimination of signal to background for some scenarios. In this analysis, further selections are made based on H_{T}^{γ} and $p_{\mathrm{T}}^{\mathrm{miss}}$. The first is sensitive to massive sparticles, and the second is sensitive to the presence of undetected particles. Figure 5.2 shows the expected Asimov significance [119]

$$\sqrt{2((s+b)\log(1+s/b)-s)}$$

for various minimal requirements on H_{T}^{γ} and $p_{\mathrm{T}}^{\mathrm{miss}}$ for two gluino-single-photon models with a gluino mass of 1600 GeV and gaugino masses of 100 and 1500 GeV and signal yield s. The background yield b is estimated using simulation only.

For signal scenarios with low gaugino mass, a selection of $H_{\mathrm{T}}^{\gamma} > 2000\,\mathrm{GeV}$ and $p_{\mathrm{T}}^{\mathrm{miss}} > 300$–$400\,\mathrm{GeV}$ yields the best significance. For signal scenarios with high gaugino masses, hardly any other H_{T}^{γ} requirement than $H_{\mathrm{T}}^{\gamma} > 700\,\mathrm{GeV}$ is necessary, and the best sensitivity can be achieved with a search region defined by $p_{\mathrm{T}}^{\mathrm{miss}} > 800\,\mathrm{GeV}$. Search regions are not defined for

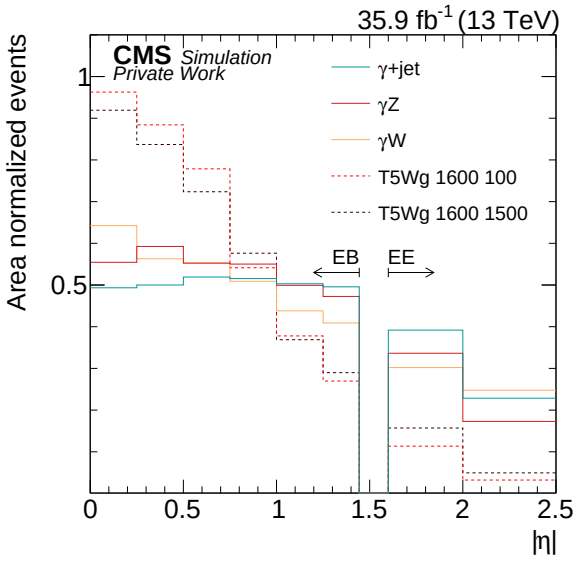

Figure 5.1: Unit area normalized $|\eta|$ distribution of the leading photon for simulated SM processes (solid lines) and two gluino-single-photon scenarios (dashed lines) with a gluino mass of 1600 GeV and gaugino masses of 100 and 1500 GeV.

each signal hypothesis independently, but one definition for all signal hypotheses is used. As signal scenarios with high gaugino masses are covered by the electroweak analysis [60], this analysis focuses on scenarios with low gaugino masses and therefore large H_{T}^{γ}.

The events are classified as low-H_{T}^{γ} ($H_{\mathrm{T}}^{\gamma} < 2\,\mathrm{TeV}$) and high-$H_{\mathrm{T}}^{\gamma}$ ($H_{\mathrm{T}}^{\gamma} > 2\,\mathrm{TeV}$). Boundaries of the search regions in $p_{\mathrm{T}}^{\mathrm{miss}}$ are defined such that the sensitivity is maximized in the high-H_{T}^{γ} selection, using the gluino-single-photon signal model with a gluino mass of 1600 GeV and a gaugino mass of 100 GeV. Firstly, the value of the lower $p_{\mathrm{T}}^{\mathrm{miss}}$ requirement of the highest-$p_{\mathrm{T}}^{\mathrm{miss}}$ search region is changed such that the sensitivity in this region is maximized. Loosening the $p_{\mathrm{T}}^{\mathrm{miss}}$ requirement decreases the signal-to-background ratio, while tightening the requirement

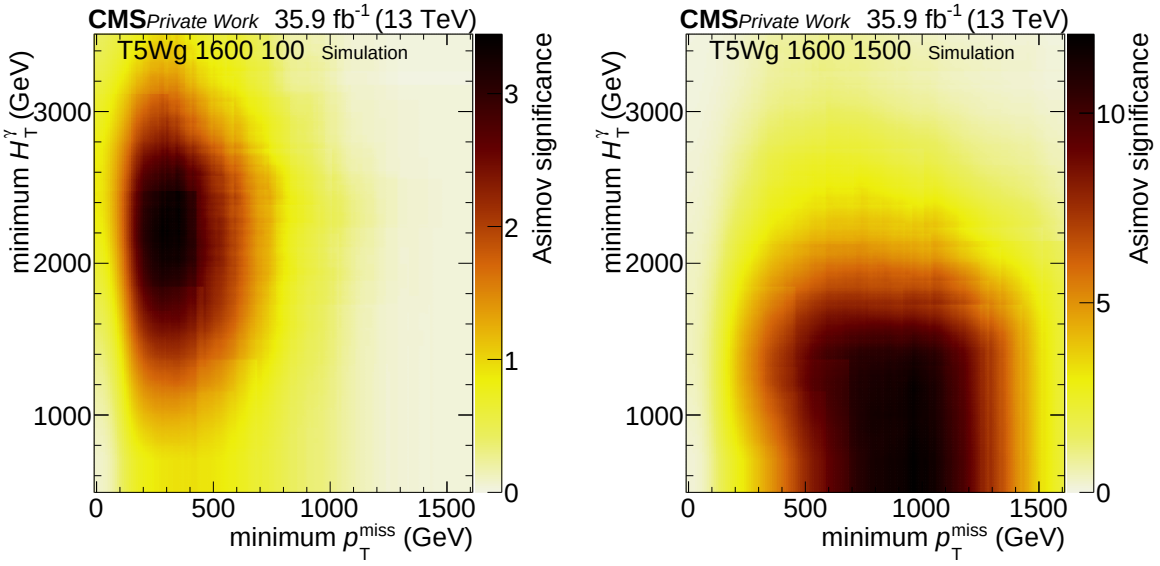

Figure 5.2: Asimov significance for various minimal $p_{\mathrm{T}}^{\mathrm{miss}}$ and H_{T}^{γ} requirements with simulated background estimation and a gluino-single-photon signal scenario with a gluino mass of 1600 GeV and a gaugino mass of 100 (1500) GeV on the left (right).

would lead to increased uncertainties. Secondly, the next lower search region in $p_{\mathrm{T}}^{\mathrm{miss}}$ is defined. The upper $p_{\mathrm{T}}^{\mathrm{miss}}$ limit of this search region is defined by the lower limit of the highest-$p_{\mathrm{T}}^{\mathrm{miss}}$ search region, while the lower limit is defined in the same way as for the highest-$p_{\mathrm{T}}^{\mathrm{miss}}$ search region. The procedure is repeated once more for the third search region in $p_{\mathrm{T}}^{\mathrm{miss}}$, yielding three search regions defined by $350 < p_{\mathrm{T}}^{\mathrm{miss}} < 450\,\mathrm{GeV}$, $450 < p_{\mathrm{T}}^{\mathrm{miss}} < 600\,\mathrm{GeV}$, and $600\,\mathrm{GeV} < p_{\mathrm{T}}^{\mathrm{miss}}$. Adding further search regions hardly increases the sensitivity and is therefore not needed. For simplicity, the same $p_{\mathrm{T}}^{\mathrm{miss}}$ boundaries are also used in the low-H_{T}^{γ} region. The definition of the search regions as a function of H_{T}^{γ} and $p_{\mathrm{T}}^{\mathrm{miss}}$ is displayed in figure 5.3.

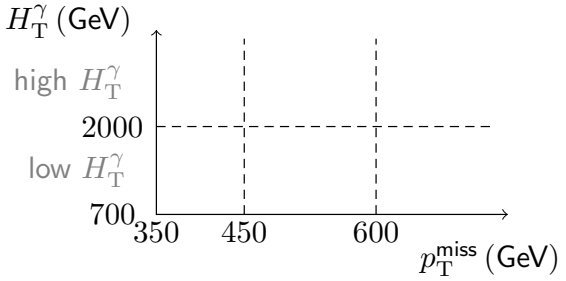

Figure 5.3: Definition of the six search regions in $p_{\mathrm{T}}^{\mathrm{miss}}$ and H_{T}^{γ}.

In the current reconstruction version, the energy of some high-energy photons is estimated inaccurately if the energy in at least one ECAL crystal is very high. The source of this mismeasurement is well understood and will be solved in future reconstruction versions, which was however not accessible to the time of the publication. If the energy mismeasurement is large, $\vec{p}_{\mathrm{T}}^{\mathrm{miss}}$ is parallel or antiparallel to the photon $\vec{p}_{\mathrm{T}}$. To suppress such events, $|\Delta\Phi(\vec{p}_{\mathrm{T}}^{\gamma}, \pm\vec{p}_{\mathrm{T}}^{\mathrm{miss}})| > 0.3$ is required.

Figure 5.4 (left) shows the distribution of $|\Delta\Phi(\vec{p}_{\mathrm{T}}^{\gamma}, \pm\vec{p}_{\mathrm{T}}^{\mathrm{miss}})|$ for simulated SM and signal events for events entering the signal selection criteria discussed above except for the $|\Delta\Phi(\vec{p}_{\mathrm{T}}^{\gamma}, \pm\vec{p}_{\mathrm{T}}^{\mathrm{miss}})| > 0.3$ requirement. The $|\Delta\Phi(\vec{p}_{\mathrm{T}}^{\gamma}, \pm\vec{p}_{\mathrm{T}}^{\mathrm{miss}})| > 0.3$ requirement reduces the acceptance for both SM and signal events. However, the loss in acceptance is largest for γ+jet events. These events have jets antiparallel to the photon, which is reconstructed with too large p_{T} and therefore also have large reconstructed $p_{\mathrm{T}}^{\mathrm{miss}}$ parallel to the photon.

In signal scenarios with low gaugino masses, the signal over SM background ratio is hardly increased, while for signal scenarios with large gaugino masses the signal over SM background ratio is increased significantly. In figure 5.4 (right), the change in significance by the $|\Delta\Phi(\vec{p}_{\mathrm{T}}^{\gamma}, \pm\vec{p}_{\mathrm{T}}^{\mathrm{miss}})| > 0.3$ requirement for the gluino-single photon model is shown for the search region with highest $p_{\mathrm{T}}^{\mathrm{miss}}$ and highest H_{T}^{γ} values. This is the most sensitive search region. Using $|\Delta\Phi(\vec{p}_{\mathrm{T}}^{\gamma}, \pm\vec{p}_{\mathrm{T}}^{\mathrm{miss}})| > 0.3$, the significance is lowered by about 20% for low gaugino masses, but increased by up to 50% for medium and high gaugino masses. The change in significance is similar for all signal models. As the uncertainty in the background yield is known, the significance is calculated as $s/\sqrt{b+\sigma_b}$, where s (b) is the signal (SM background) yield in a single search region, and σ_b the total background uncertainty. The background yield and its uncertainty are estimated using the methods described in this chapter.

5.2 Background from events with nongenuine $p_{\mathrm{T}}^{\mathrm{miss}}$

If the vectorial sum of the p_{T} of non-detectable particles, for example neutrinos or gravitinos, is small compared to the reconstructed $p_{\mathrm{T}}^{\mathrm{miss}}$, the $p_{\mathrm{T}}^{\mathrm{miss}}$ is nongenuine. The contribution of SM processes with large nongenuine $p_{\mathrm{T}}^{\mathrm{miss}}$ is estimated using data control regions (CR). The $p_{\mathrm{T}}^{\mathrm{miss}}$

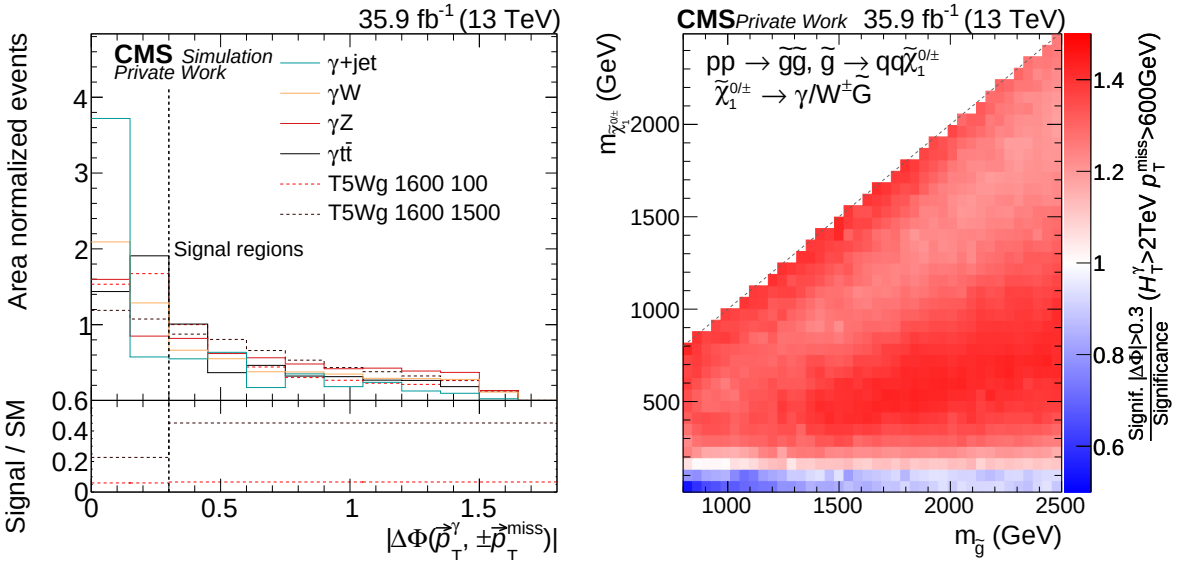

Figure 5.4: Unit area normalized $|\Delta\Phi(\vec{p}_{\mathrm{T}}^{\,\gamma}, \pm\vec{p}_{\mathrm{T}}^{\,\mathrm{miss}})|$ distribution for simulated SM processes (solid lines) and two gluino-single-photon scenarios (dashed lines) with a gluino mass of 1600 GeV and gaugino masses of 100 and 1500 GeV for events in the six search regions (except of the $|\Delta\Phi(\vec{p}_{\mathrm{T}}^{\,\gamma}, \pm\vec{p}_{\mathrm{T}}^{\,\mathrm{miss}})| > 0.3$ selection). The bottom plot shows the ratio of signal over total SM event yield for $|\Delta\Phi(\vec{p}_{\mathrm{T}}^{\,\gamma}, \pm\vec{p}_{\mathrm{T}}^{\,\mathrm{miss}})| > 0.3$ and $|\Delta\Phi(\vec{p}_{\mathrm{T}}^{\,\gamma}, \pm\vec{p}_{\mathrm{T}}^{\,\mathrm{miss}})| < 0.3$. Right: Significance with the selection on $|\Delta\Phi|$ over significance without this requirement for the squark-diphoton (gluino-single-photon) model in the highest-$p_{\mathrm{T}}^{\mathrm{miss}}$ and H_{T}^{γ} search region on the left (right).

distribution of multijet events without photons (jet CR) is modified and normalized to the number of events with at least one photon and small $p_{\mathrm{T}}^{\mathrm{miss}}$ values (photon CR). The modified and normalized event yield of the multijet events is used as a prediction for the background from events with large nongenuine $p_{\mathrm{T}}^{\mathrm{miss}}$ and a photon.

5.2.1 Characterization of the background

There are no undetectable particles in the hard scattering of multijet, γ+jet, $W \to qq$, or $Z \to qq$ events, so there is no genuine $p_{\mathrm{T}}^{\mathrm{miss}}$. Multijet events are events comprised uniquely of jets produced through the strong interaction. However, due to the limited detector resolution, nongenuine $p_{\mathrm{T}}^{\mathrm{miss}}$ may be reconstructed. Jets are the objects with the largest energy resolution of around 10%, depending on p_{T} and η [120]. In addition, neutrinos can be produced in the fragmentation of quarks and gluons, but the contribution of neutrinos to $p_{\mathrm{T}}^{\mathrm{miss}}$ is small in events with large $p_{\mathrm{T}}^{\mathrm{miss}}$. The probability of exceeding $p_{\mathrm{T}}^{\mathrm{miss}} > 350$ GeV is small, but the cross section of multijet and γ+jet events is large, leading to a considerable amount of events of these types in the search regions.

To enter the search region, a photon must be reconstructed. The photon can either be part of the hard scattering, it can be radiated from a charged particle in the initial or final state, it can be produced in the fragmentation of quarks in multijet events, or it can be a particle misidentified as a photon. Neutral pions usually decay into a photon pair, yielding a similar calorimetric signals as photons from the hard interaction. The p_{T} resolution for these photons and photons from the hard interaction is around 1% [94].

Most of the events with a photon and a single dominating jet are balanced, thus H_{T}^{γ} is about twice the photon p_{T}. In events with a photon and several jets, the contribution of the photon

to H_{T}^{γ} is suppressed. In generated γ+2jet events, the photon is the leading, next-to-leading, and trailing object in 20%, 30%, and 50% of the events, respectively. The H_{T}^{γ} of most of the γ+jet events is dominated by the jet p_{T}, and not by the photon p_{T}.

5.2.2 Definition of the control regions

The jet CR is defined by selecting events with $H_{\mathrm{T}}^{\gamma} > 700\,\mathrm{GeV}$, and no photon with $p_{\mathrm{T}} > 100\,\mathrm{GeV}$ reconstructed in the EB. The shape of the $p_{\mathrm{T}}^{\mathrm{miss}}$ distribution is used as prediction in the search regions.

The trigger used to select these events requires $H_{\mathrm{T}}^{\gamma} > 600\,\mathrm{GeV}$. As the rate of this trigger would be very high, this trigger is prescaled, such that on average 4% of the events were recorded. No unexpected differences in the trigger efficiencies with respect to the trigger used for the search regions are observed, as shown in appendix A.2.

The jet CR is dominated by multijet events, as shown in figure 5.5 for simulated events. A negligible number of γ+jet events is also selected for which the photon p_{T} is too low or when the photon is not reconstructed in the EB. For high $p_{\mathrm{T}}^{\mathrm{miss}}$ values, events from W+jet, $t\bar{t}$+jet, and $Z(\nu\nu)$+jet processes dominate the CR. The fraction of multijet events in the jet CR is larger in the high-H_{T}^{γ} selection than in the low-H_{T}^{γ} selection, as the electroweak bosons are produced at lower scales and therefore populate the low-H_{T}^{γ} selection.

The method is designed to predict the background from events with nongenuine $p_{\mathrm{T}}^{\mathrm{miss}}$, so events with genuine $p_{\mathrm{T}}^{\mathrm{miss}}$ distort the prediction of the background estimation method. The event yield from simulated W+jet, $t\bar{t}$+jet, and $Z(\nu\nu)$+jet processes is subtracted from the jet CR in data to have a CR containing multijet events only.

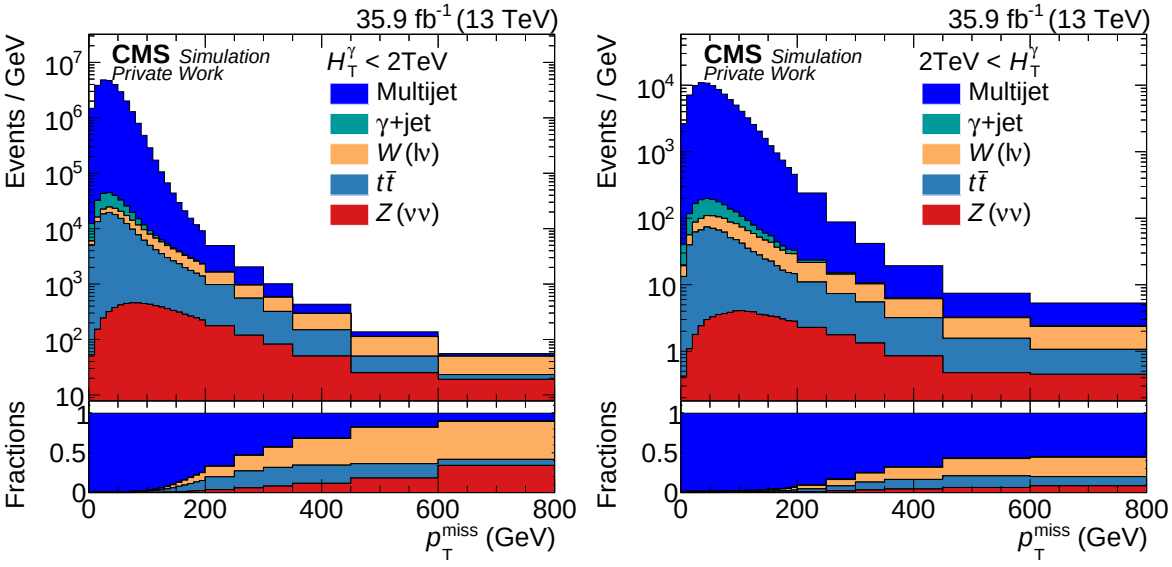

Figure 5.5: Simulated distribution of $p_{\mathrm{T}}^{\mathrm{miss}}$ for events in the jet CR for low H_{T}^{γ} (left) and high H_{T}^{γ} (right) values. The size of the last three bins correspond to the definition of the search regions. In this figure and the following ones, the last bin includes the overflow, i.e. all events with $p_{\mathrm{T}}^{\mathrm{miss}} > 600\,\mathrm{GeV}$. At the bottom, the relative fractions of all contributing processes are displayed.

To normalize the jet CR, the photon CR is defined similarly to the search regions, except that $p_{\mathrm{T}}^{\mathrm{miss}}$ is required to be smaller than 100 GeV: At least one photon with $p_{\mathrm{T}} > 100\,\mathrm{GeV}$ reconstructed in the EB is required, as well as $|\Delta\Phi(\vec{p}_{\mathrm{T}}^{\,\gamma}, \pm\vec{p}_{\mathrm{T}}^{\,\mathrm{miss}})| > 0.3$ and $H_{\mathrm{T}}^{\gamma} > 700\,\mathrm{GeV}$.

Figure 5.6 shows a sketch of the search region, jet CR, and photon CR as function of the photon multiplicity and $p_{\mathrm{T}}^{\mathrm{miss}}$.

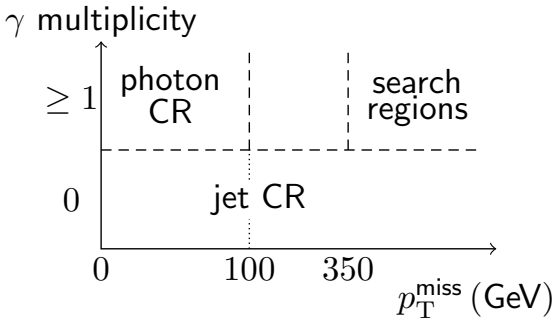

Figure 5.6: Sketch of the photon CR, the jet CR, and the search regions.

Similar to the search regions, the photon and the jet CRs are split into a low-H_{T}^{γ} region ($700\,\mathrm{GeV} < H_{\mathrm{T}}^{\gamma} < 2000\,\mathrm{GeV}$) and a high-$H_{\mathrm{T}}^{\gamma}$ selection ($H_{\mathrm{T}}^{\gamma} \geq 2000\,\mathrm{GeV}$), and the background estimation method is performed in both low- and high-H_{T}^{γ} selections independently.

5.2.3 Modification of the $p_{\mathrm{T}}^{\mathrm{miss}}$ spectrum

The $p_{\mathrm{T}}^{\mathrm{miss}}$ distribution of the photon CR (black dots) and the jet CR (blue lines) can be seen for events with $p_{\mathrm{T}}^{\mathrm{miss}} < 100\,\mathrm{GeV}$ in figure 5.7 in the low-H_{T}^{γ} (high-H_{T}^{γ}) selection on the left (right). All $p_{\mathrm{T}}^{\mathrm{miss}}$ distributions of the jet CR are normalized to the event yield in the photon CR. While the $p_{\mathrm{T}}^{\mathrm{miss}}$ distribution of the photon and the jet CRs are similar in shape, they do not match within their uncertainties. As photons have better resolutions than jets, the mean of the $p_{\mathrm{T}}^{\mathrm{miss}}$ in the photon CR is smaller than the one in the jet CR.

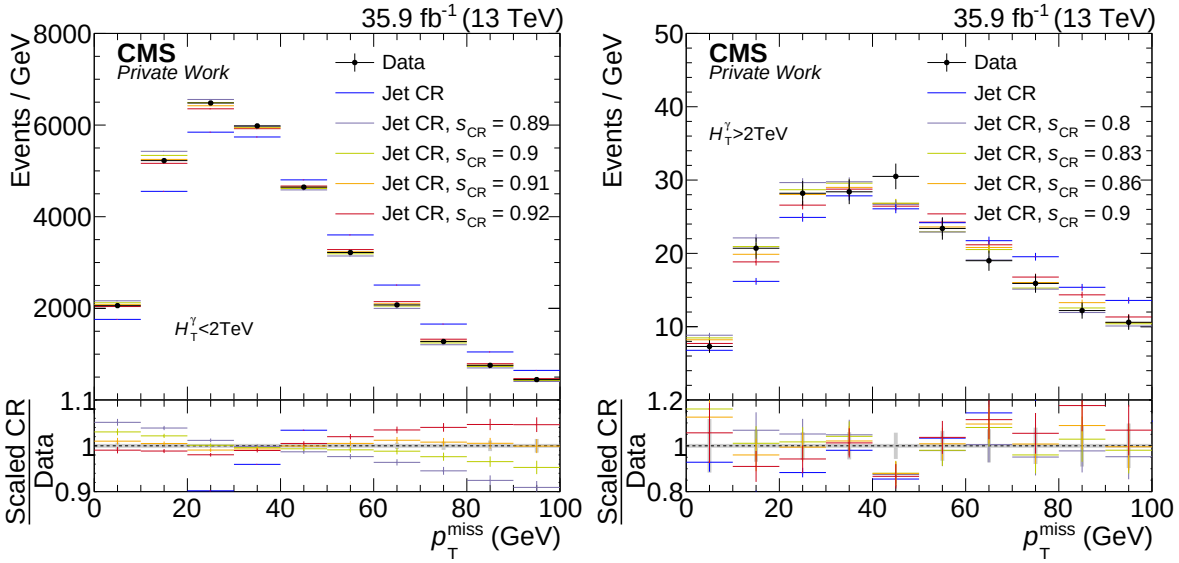

Figure 5.7: Distribution of $p_{\mathrm{T}}^{\mathrm{miss}}$ for the photon and the jet CRs for $p_{\mathrm{T}}^{\mathrm{miss}} < 100\,\mathrm{GeV}$ in the low-H_{T}^{γ} selection (left) and the high-H_{T}^{γ} selection (right). The $p_{\mathrm{T}}^{\mathrm{miss}}$ values of the jet CR are scaled by different values.

To improve the matching, each $p_{\mathrm{T}}^{\mathrm{miss}}$ value of the jet CR is multiplied by the scale factor s_{CR}:

$$\tilde{p}_{\mathrm{T}}^{\mathrm{miss}} = s_{\mathrm{CR}} \cdot p_{\mathrm{T}}^{\mathrm{miss}}$$

This moves the $\tilde{p}_{\mathrm{T}}^{\mathrm{miss}}$ distribution to lower or higher $p_{\mathrm{T}}^{\mathrm{miss}}$ values, without changing the normalization. As seen in figure 5.7, the $\tilde{p}_{\mathrm{T}}^{\mathrm{miss}}$ distribution of the jet CR scaled by 0.91 (0.84) in the low-H_{T}^{γ} (high-H_{T}^{γ}) selection agrees much better to the $p_{\mathrm{T}}^{\mathrm{miss}}$ distribution of the photon CR than the unscaled one. The agreement between the $p_{\mathrm{T}}^{\mathrm{miss}}$ distribution of the photon CR and the $\tilde{p}_{\mathrm{T}}^{\mathrm{miss}}$ of the jet CR is evaluated by calculating

$$\chi^2 = \sum_{\text{bin } i=1}^{10} \left(\frac{n_i^{\text{photon CR}} - n_i^{\text{jet CR}}}{\sigma_i} \right)^2 ,$$

where n_i are the event yields in bin i and σ_i is the combined uncertainty of the event yields of the photon CR and the jet CR [121]. Ten equidistant bins are used from 0 to 100 GeV in $p_{\mathrm{T}}^{\mathrm{miss}}$ ($\tilde{p}_{\mathrm{T}}^{\mathrm{miss}}$), as displayed in figure 5.7. The χ^2 values for different s_{CR} are shown in figure 5.8. The scale factor s_{CR}^0 of the minimal χ^2 yields in the best agreement between photon CR and jet CR, while the statistical uncertainty σ_{stat} in the s_{CR}^0 is evaluated by

$$\chi^2(s_{\mathrm{CR}}^0 \pm \sigma_{\mathrm{stat}}) = \chi^2(s_{\mathrm{CR}}^0) + 1.$$

To find the minimum and the statistical uncertainty, a parabola is fitted to the χ^2 values. The statistical uncertainty interval (two times the uncertainty) is displayed by the red area below the minimum of the parabola in the figure.

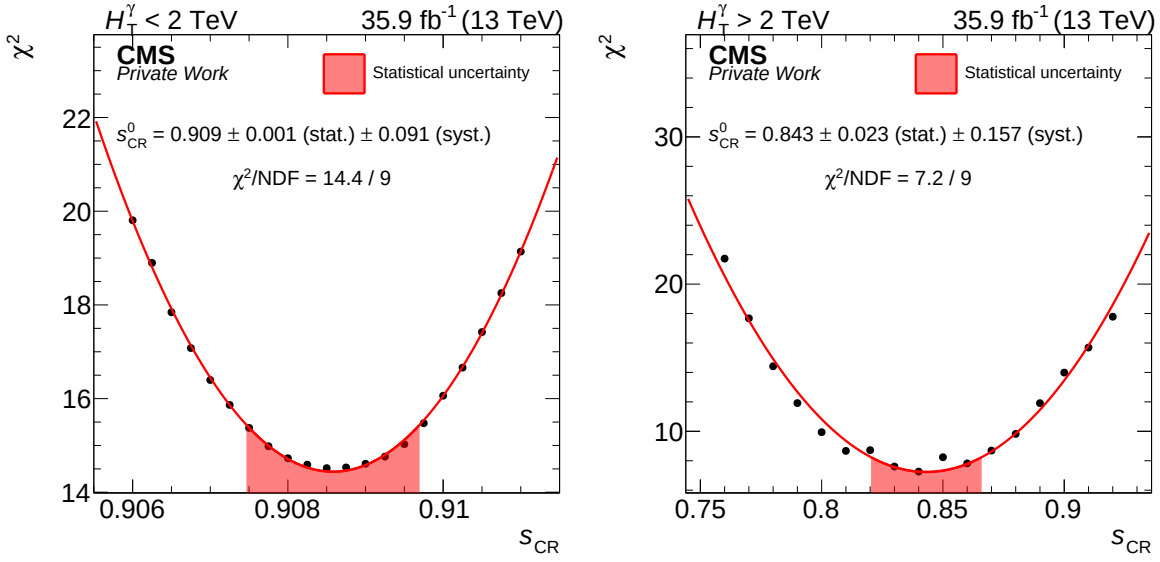

Figure 5.8: The χ^2 between the photon CR and jet CR as a function of s_{CR} for the low- (high-) H_{T}^{γ} selection on the left (right).

The number of degrees of freedom (NDF) corresponds to the number of bins of the $p_{\mathrm{T}}^{\mathrm{miss}}$ distributions minus one and is nine in all fits. The best χ^2 over NDF is close to one. The best s_{CR} is smaller than one, reflecting the better resolution of photons compared to jets. The full difference of s_{CR} to unity is taken as a systematic uncertainty. Studies on simulated samples showed that the associated uncertainty is reasonable (see section 5.2.5).

There are fewer events in the high-H_{T}^{γ} selection as in the low-H_{T}^{γ} selection, leading to more fluctuations in the χ^2 fit for the high-H_{T}^{γ} selection as shown in figure 5.8. By default, the $p_{\mathrm{T}}^{\mathrm{miss}}$ distribution is filled into ten uniform bins, as shown in figure 5.7. The effect of different bin choices on s_{CR}^0 is studied and found to be negligible, as shown for the high-H_{T}^{γ} selection in figure 5.9. The determination of s_{CR} is repeated with a bin width of 20 GeV and 30 GeV, and

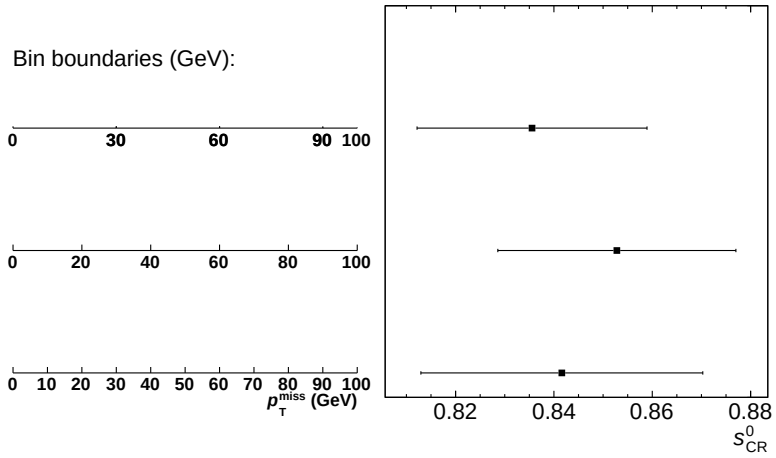

Figure 5.9: Scale factors and their statistical uncertainty (right) for different bin choices of the $p_{\mathrm{T}}^{\mathrm{miss}}$ spectrum (left) in the high-H_{T}^{γ} selection.

the s_{CR} factors are well compatible within their statistical uncertainty. Smaller bin widths are not studied, as the statistical uncertainty in each bin would increase even further.

The scaled $\tilde{p}_{\mathrm{T}}^{\mathrm{miss}}$ distribution of the jet CR is normalized by

$$n_{\gamma/\mathrm{jet}} = N^{\text{photon selection}}_{p_{\mathrm{T}}^{\mathrm{miss}}<100\,\mathrm{GeV}} / N^{\text{jet selection}}_{\tilde{p}_{\mathrm{T}}^{\mathrm{miss}}<100\,\mathrm{GeV}} = \begin{cases} (1.290 \pm 0.014) \cdot 10^{-3} & \text{for low } H_{\mathrm{T}}^{\gamma} \\ (3.71 \pm 0.34) \cdot 10^{-3} & \text{for high } H_{\mathrm{T}}^{\gamma} \end{cases} \tag{5.1}$$

where the numerator (denominator) is the number of events in the photon (jet) CR with $p_{\mathrm{T}}^{\mathrm{miss}}(\tilde{p}_{\mathrm{T}}^{\mathrm{miss}}) < 100\,\mathrm{GeV}$. Since the number of events in the jet CR is much larger than the number of events in the photon CR, $n_{\gamma/\mathrm{jet}}$ is small. The uncertainty includes the statistical uncertainty of both numerator and denominator. In addition, differences in $N^{\text{jet selection}}_{\tilde{p}_{\mathrm{T}}^{\mathrm{miss}}<100\,\mathrm{GeV}}$ due to the uncertainty in s^0_{CR} are added quadratically to this uncertainty. For $p_{\mathrm{T}}^{\mathrm{miss}} < 100\,\mathrm{GeV}$, the shape and the normalization of the jet and the photon CRs are in agreement. For $p_{\mathrm{T}}^{\mathrm{miss}} > 100\,\mathrm{GeV}$, the $\tilde{p}_{\mathrm{T}}^{\mathrm{miss}}$ distribution of the jet CR is used as prediction for the $p_{\mathrm{T}}^{\mathrm{miss}}$ distribution in the search regions.

5.2.4 Uncertainties

Three sources of uncertainties are considered: The uncertainty in the shape, the uncertainty in the normalization in $p_{\mathrm{T}}^{\mathrm{miss}} < 100\,\mathrm{GeV}$, and the statistical uncertainty in the jet CR at high $\tilde{p}_{\mathrm{T}}^{\mathrm{miss}}$.

The uncertainty in s^0_{CR} is propagated to the prediction by scaling the $\tilde{p}_{\mathrm{T}}^{\mathrm{miss}}$ values of the jet CR by s^0_{CR} shifted upwards and downwards by its uncertainty. Like the nominal shifted $\tilde{p}_{\mathrm{T}}^{\mathrm{miss}}$ distribution, the upwards and downwards shifted distributions are also normalized to the photon CR at low $p_{\mathrm{T}}^{\mathrm{miss}}$ values. In each search region, half of the difference between the upwards and downwards corrected distribution is taken as systematic uncertainty. As displayed in the ratio plot in the bottom panels of figure 5.7, this leads to a smaller uncertainty for $p_{\mathrm{T}}^{\mathrm{miss}} \approx 35(55)\,\mathrm{GeV}$ in the low- (high-) H_{T}^{γ} selection. This uncertainty is fully correlated in the three search regions of the low- and high-H_{T}^{γ} selection.

The second uncertainty source results from the accuracy of the normalization given in equation 5.1. Due to the large number of events in low $p_{\mathrm{T}}^{\mathrm{miss}}$, this uncertainty is the smallest

uncertainty considered. It is also correlated in the three search regions the low- and high-H_{T}^{γ} selection.

The last source of uncertainty is given by the statistical uncertainty of the jet CR for large $\tilde{p}_{\mathrm{T}}^{\mathrm{miss}}$, and is uncorrelated between all search regions. In the search regions, the total relative uncertainty varies between 56 and 250%. However, in the search region with a relative uncertainty of this background of 250%, the nongenuine $p_{\mathrm{T}}^{\mathrm{miss}}$ background accounts only for about 4% of the total SM background.

5.2.5 Validation with simulated events

The method is validated using γ+jet and multijet simulation. No W, Z, or $t\bar{t}$ events are added, so in contrast to the application on data, these background processes do not need to be subtracted from the jet CR. In figure 5.10, the simulated $p_{\mathrm{T}}^{\mathrm{miss}}$ distribution for γ+jet and multijet events is shown as black dots. The simulated jet CR, scaled and normalized in low $p_{\mathrm{T}}^{\mathrm{miss}}$, is shown as filled histogram. An upper Poisson uncertainty is added in bins where events are expected but due to the limited number of simulated events, no simulated events are selected. No deviation is expected as no signal processes are present in this study by construction. The overall agreement within the uncertainties suggests that the method performs as expected. The scale factor determination (similar to figure 5.8) for the validation is shown in appendix A.3.

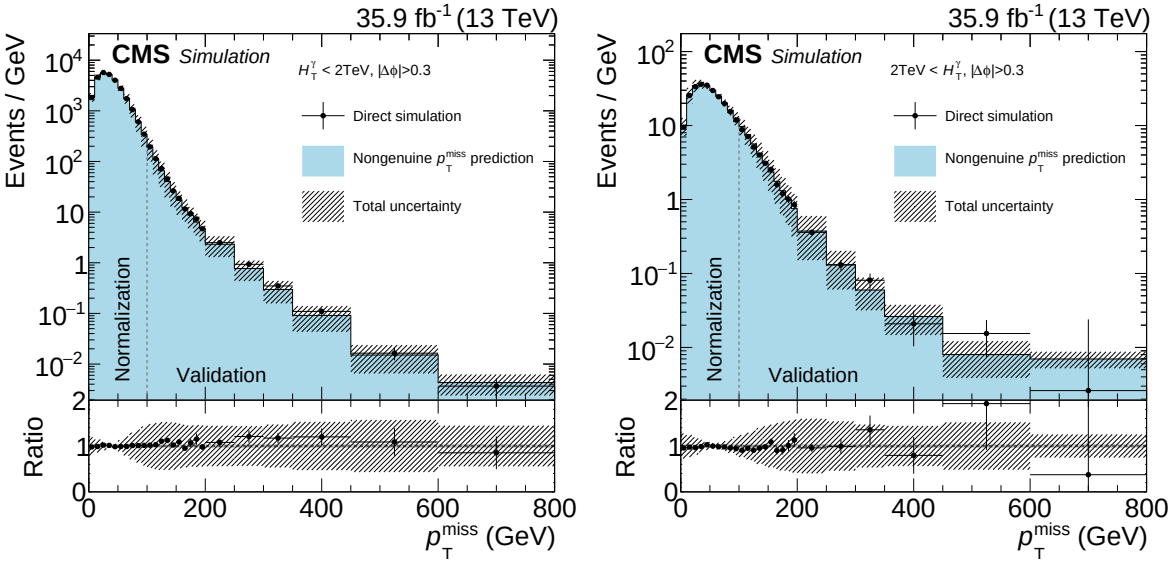

Figure 5.10: Comparisons of the $p_{\mathrm{T}}^{\mathrm{miss}}$ distributions as simulated (back dots) and the prediction as estimated from simulation (filled histograms). The low- (high-) H_{T}^{γ} selection is shown on the left (right) [1].

5.3 Background from events with electrons

The signature of electrons and photons in the calorimeters is indistinguishable, but photons are required to be reconstructed without matching pixel-seeds. Electrons without reconstructed pixel-seeds can therefore be misidentified as photons. In $W \to e\nu$ events, the electron is produced in association with a neutrino, leading to considerable $p_{\mathrm{T}}^{\mathrm{miss}}$ values, therefore allowing

such events to enter the search regions. The W bosons can be produced directly in proton-proton interactions, or as decay products in $t\bar{t}$ events.

The contribution of this background is estimated using the electron control region, which is defined similarly to the search region, except that instead of requiring at least one photon, at least one electron is required. The electron is reconstructed similarly to the photon, except that at least one pixel-seed is required. Doing so, mainly $W \to e\nu$ and $t\bar{t}$ events are selected. The event yield of the electron control region is scaled by a normalization factor, which is estimated using $Z \to ee$ events.

5.3.1 Measurement of $R_{\gamma/e}$

The $R_{\gamma/e}$ ratio is defined as the probability that a true electron is reconstructed as a photon over the probability that a true electron is reconstructed as an electron:

$$R_{\gamma/e} = \frac{p(e \to \gamma)}{p(e \to e)}$$

For measured electrons in data, it is not known if a reconstructed electron results from a real electron, so the tag-and-probe method [94] is used to select real electrons with a high purity from $Z \to ee$ decays. If the invariant mass of a GSF electron (tag) and a second electron (probe) is close to the Z boson mass, the second electron is most likely a real electron.

Online, the electron trigger system selects events with at least one GSF electron with $p_{\mathrm{T}} > 27\,\mathrm{GeV}$ and $|\eta| < 2.1$. Tight identification criteria are required on trigger level to reduce the triggered event rate. Offline, all GSF electrons with $p_{\mathrm{T}} > 30\,\mathrm{GeV}$ and $|\eta| < 2.1$, which geometrically match a triggered electron within $\Delta R < 0.2$ are used as *tag* objects. Both electrons and photons are categorized as *probe* objects, their only discriminating feature being the number of pixel-seeds.

All tags are combined with all probes, excluding the combinations where tag and probe are separated by $\Delta R < 0.3$ and are presumably the same object. A typical $Z \to ee$ event is reconstructed with both electrons being reconstructed as a tag and probe, resulting in four combinations, of which two are rejected due to the criterion of $\Delta R > 0.3$. A $Z \to ee$ event in which one electron is misidentified as a photon is reconstructed with one tag (the GSF electron) and two probes, of which one coincides with the tag. If the probe is reconstructed with a pixel-seed, the pair is classified as an ee event, elsewise it is classified as an $e\gamma$ event.

The double counting is intended and reflects the fact that both electrons of the Z decay can be reconstructed as photon. The number of ee events from Z boson decays is given as

$$\begin{aligned} N_{ee} &= N_{Z\to ee}\left[p(e_1 \to e)p(e_2 \to e_{\mathrm{tag}}) + p(e_2 \to e)p(e_1 \to e_{\mathrm{tag}})\right] \\ &= 2N_{Z\to ee}p(e \to e)p(e \to e_{\mathrm{tag}}), \end{aligned}$$

where $p(e \to e_{\mathrm{tag}})$ is the probability that a true electron is reconstructed as a tag object. The order of the two electrons is denoted as indices. As the order of electrons is irrelevant for the reconstruction probabilities, the formula is simplified in the last step. The same equation can be used to express the number of $e\gamma$ events, such that $R_{\gamma/e}$ can be calculated as

$$R_{\gamma/e} = \frac{N_{Z\to ee}\left[p(e_1 \to \gamma)p(e_2 \to e_{\mathrm{tag}}) + p(e_2 \to \gamma)p(e_1 \to e_{\mathrm{tag}})\right]}{N_{Z\to ee}\left[p(e_1 \to e)p(e_2 \to e_{\mathrm{tag}}) + p(e_2 \to e)p(e_1 \to e_{\mathrm{tag}})\right]} = \frac{p(e \to \gamma)}{p(e \to e)}$$

If no match to the trigger objects as described above would be performed, the $R_{\gamma/e}$ would be calculated by

$$R_{\gamma/e} = \frac{p(e \to \gamma)\,[tr(e_{\text{tag}})tr(\gamma) + tr(e_{\text{tag}})\overline{tr}(\gamma) + \overline{tr}(e_{\text{tag}})tr(\gamma)]}{p(e \to e)\,[tr(e_{\text{tag}})tr(e) + tr(e_{\text{tag}})\overline{tr}(e) + \overline{tr}(e_{\text{tag}})tr(e)]} = \frac{p(e \to \gamma)\,[tr(e_{\text{tag}}) + \overline{tr}(e_{\text{tag}})tr(\gamma)]}{p(e \to \gamma)\,[tr(e_{\text{tag}}) + \overline{tr}(e_{\text{tag}})tr(e)]}$$

where $tr(x)$ is the probability that object x fulfills the electron criteria of the electron trigger, and $\overline{tr}(x)$ the probability that it does not fulfill the trigger criteria. It is assumed that the tag or the probe fulfills the trigger criteria, and so no term of the form $\overline{tr}(x)\overline{tr}(x)$ enters in the first step. In the last step, $tr(\gamma) + \overline{tr}(\gamma) = 1$ and $tr(e) + \overline{tr}(e) = 1$ are used. To eliminate the dependency on the trigger efficiencies, the match of the tag object to a trigger electron is required, setting $\overline{tr}(e_{\text{tag}}) = 0$.

The distributions of the invariant mass for the ee and $e\gamma$ categories are shown in figure 5.11 as black dots. In addition to the component from the Z boson resonance with a clear peak around the Z boson mass, combinatorial background is selected.

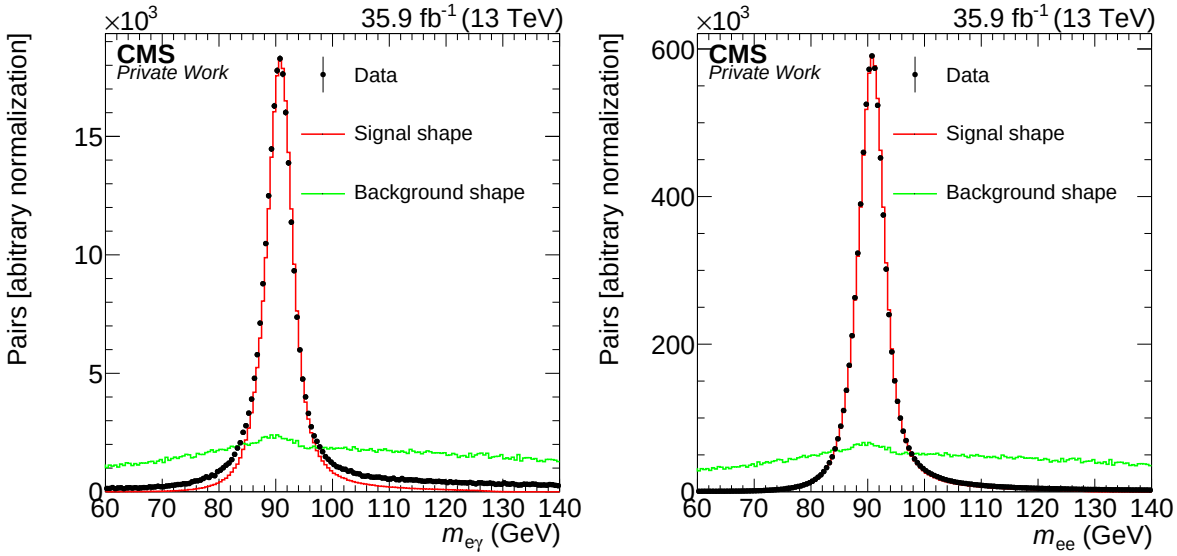

Figure 5.11: Invariant mass of tag and probe pairs for the $e\gamma$ selection (left) and ee selection (right). The background and signal shapes are drawn with arbitrary normalizations.

To subtract the background component, fits to the invariant mass distributions are performed. The dominant processes contributing as background are W boson events, where one jet is misidentified as a photon, γW events, and $\gamma t\bar{t}$ events. For all of these, the invariant mass does not peak at the Z boson resonance. To describe the background shape, the distribution of the invariant mass of tags combined with muons ($e\mu$) is used. Muons are selected with the same kinematic criteria as the probes, leading to similar combinatorial events. The shape of the tags and muons is shown as a green line in figure 5.11 with arbitrary normalization. To minimize possible biases due to low statistics, the background shape is smeared using a kernel density estimator with Gaussian cores [122]. The uncertainty of a uniformly distributed bin is taken as width of the Gaussians to achieve a smooth background shape.

The signal shape is taken from Z boson simulation, where both tag and probe are required to be matched to a generated electron from the Z boson decay. It is convolved with a Gaussian,

taking differences between simulation and measurement into account. The convolution is performed using a fast Fourier implementation [123].

The signal shape from simulation and the combinatorial background shape from $e\mu$ events are fitted to the invariant mass distribution selected for data events, independently for the $e\gamma$ and the ee sample. The number of signal events (N_γ or N_e), the number of background events, the mean, and the width of the convolved Gaussian are free parameters of the fit. The fitted curves are shown in figure 5.12, and the parameters of the fits in table 5.1.

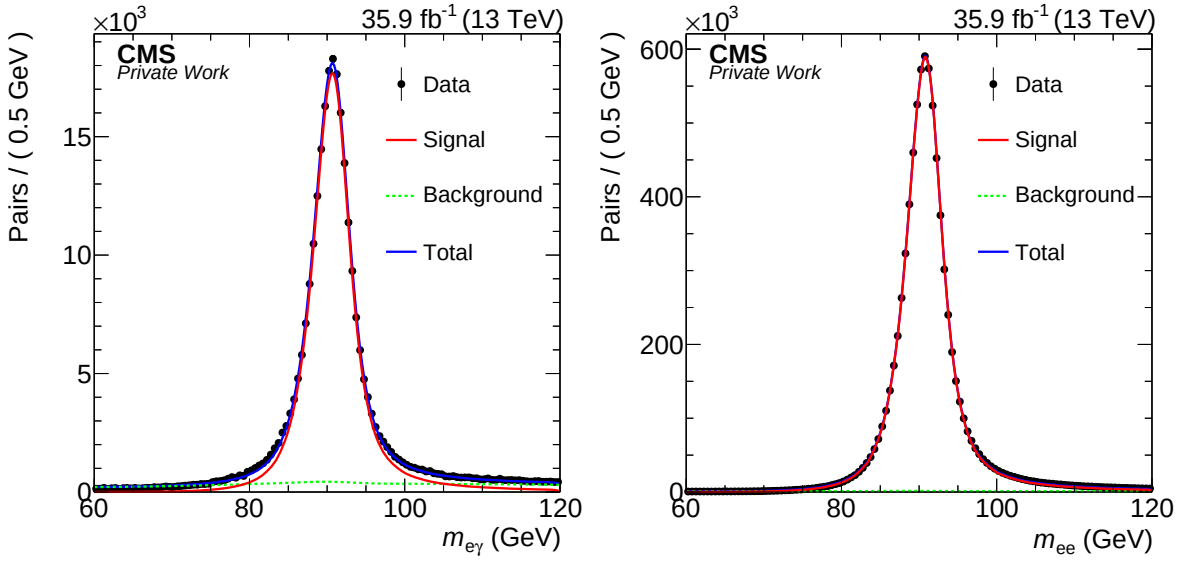

Figure 5.12: The signal and background shape fitted to the invariant mass of tag and probe pairs for the $e\gamma$ selection (left) and ee selection (right) displayed as blue line. The red line shows the signal component, while the green dashed line the background component. As the background contribution is small, the blue line is often overlaid by the red line.

Table 5.1: Fitted number of background events ($N_{\text{background}}$), mean (μ_{smear}) and width (σ_{smear}) of the convolved Gaussian for the estimation of $R_{\gamma/e}$.

	$N_{e/\gamma}$	$N_{\text{background}}$	μ_{smear} (GeV)	σ_{smear} (GeV)
$e\gamma$	246750 ± 550	38950 ± 320	-0.1307 ± 0.0066	0.432 ± 0.033
ee	8053300 ± 3000	133700 ± 940	-0.0242 ± 0.0011	0.0954 ± 0.0037

The parameters of the convolution are small compared to the Z boson mass and the width of the distribution. The uncertainties are statistical only. While the background fraction is 2% for the ee selection, it is 15% for the $e\gamma$ selection. From the number of signal events, $R_{\gamma/e}$ and its statistical uncertainty can be calculated:

$$R_{\gamma/e} = \frac{N_\gamma}{N_e} = (3.0639 \pm 0.0068)\%$$

In previous versions of this analysis, the probability that an electron is misreconstructed as a photon was measured by

$$f_{e\to\gamma} = \frac{N_\gamma}{N_e + N_\gamma} = \frac{R_{\gamma/e}}{1 + R_{\gamma/e}} \overset{R_{\gamma/e}\ll 1}{\approx} R_{\gamma/e},$$

where a single fit to a mix of ee and $e\gamma$ events was performed to evaluate the denominator of the fraction. The electron CR was then scaled by $f_{e\to\gamma}/(1 - f_{e\to\gamma})$. Using $R_{\gamma/e}$ instead of

$f_{e\to\gamma}$ has two advantages: Firstly, $R_{\gamma/e}$ can be applied directly to the electron CR. Secondly, the fits of the numerator and the denominator can be performed independently, reducing the complexity. As $R_{\gamma/e}$ is usually small, the numerical values of $R_{\gamma/e}$ and $f_{e\to\gamma}$ are similar.

The studies are repeated using simulated $Z \to ee$ events only. The selection is the same as the selection for the signal shape, meaning that both tag and probe are required to be match a generated electron. No background subtraction is needed, and the ratio of $e\gamma$ to ee events with $60 < m_{e\gamma/ee} < 120\,\text{GeV}$ yields

$$R^{\text{sim}}_{\gamma/e} = 1.54\%$$

with negligible statistical uncertainty. Instead of using the tag and probe method, $R^{\text{sim}}_{\gamma/e}$ can also be computed by calculating the ratio of generated electrons reconstructed as photons to generated electrons reconstructed as electrons. The results are compatible to the tag and probe evaluation of the simulated $R^{\text{sim}}_{\gamma/e}$. The disagreement between the simulated and the measured $R_{\gamma/e}$ was already observed in former analyses [54, 59]. The simulation is optimized to simulate particles correctly, but it is more difficult to simulate the misidentification of particles. This motivates the background prediction using data control regions instead of using SM simulation to estimate the background.

5.3.2 Systematic uncertainties

The measurement of $R_{\gamma/e}$ is performed on $Z \to ee$ events and will be applied to the electron CR dominated by W and $t\bar{t}$ events with high $p_{\text{T}}^{\text{miss}}$, H_{T}^{γ}, and high electron p_{T}. The dominant uncertainty in the background estimation is the extrapolation from the Z boson region to the electron CR. Instead of computing $R_{\gamma/e}$ inclusively as done above, it is done in bins of several variables. For event variables as the vertex multiplicity, the jet multiplicity, $p_{\text{T}}^{\text{miss}}$, or H_{T}^{γ}, the selection is applied to the ee, the $e\gamma$, and the $e\mu$ events, while for kinematic variables like p_{T}, ϕ, or η, the selection is applied to the probes and the muons. The fits to some example bins are shown in figure 5.13. The fraction of background processes is higher than in the inclusive selection, but is still well described by the background shape from $e\mu$ events.

In figure 5.14, $R_{\gamma/e}$ is shown as a function of several variables, where the computation of $R_{\gamma/e}$ is performed independently in each bin. The dependency in η and ϕ is due to the layout and status of the pixel detector. At $\eta \approx 0$, the modules on which the pixels are mounted are pieced together, leaving a gap since the active pixel sensors do not cover the margin of the modules. Higher $R_{\gamma/e}$ are also observed for $|\eta| > 2.4$, as the acceptance for the pixel detector decreases since only two layers are geometrically accessible, as shown in figure 3.3. The inefficiency at $|\phi| \approx 1.6$ is caused by a larger gap in the layout of the pixel detector, while the inefficiency at $\phi \approx 2.6$ is caused by a dead module. The electrons from $Z \to ee$ and the electrons in the electron CR are expected to have the same η-ϕ distribution, and therefore a parametrization in this variable has negligible effect.

The $R_{\gamma/e}$ slightly decreases with the electron p_{T}. This is also observed using generator information to calculate $R_{\gamma/e}$ and in W or $t\bar{t}$ processes.

For the tag-and-probe method, $R_{\gamma/e}$ increases with $p_{\text{T}}^{\text{miss}}$ in $Z \to ee$ events, in which the $p_{\text{T}}^{\text{miss}}$ is caused by the detector resolution. The dependency of $R_{\gamma/e}$ and $p_{\text{T}}^{\text{miss}}$ is not observed in simulated W boson decays or $t\bar{t}$ events, in which $p_{\text{T}}^{\text{miss}}$ is caused by the presence of neutrinos. As the electron CR with $p_{\text{T}}^{\text{miss}} > 350\,\text{GeV}$ is dominated by W boson and $t\bar{t}$ events, the dependency of $R_{\gamma/e}$ with nongenuine $p_{\text{T}}^{\text{miss}}$ is assumed to be negligible.

There is a large dependency of $R_{\gamma/e}$ on the vertex multiplicity. The reconstruction of pixel-seeds matching to the ECAL cluster is more difficult with more vertices in an event, leading to

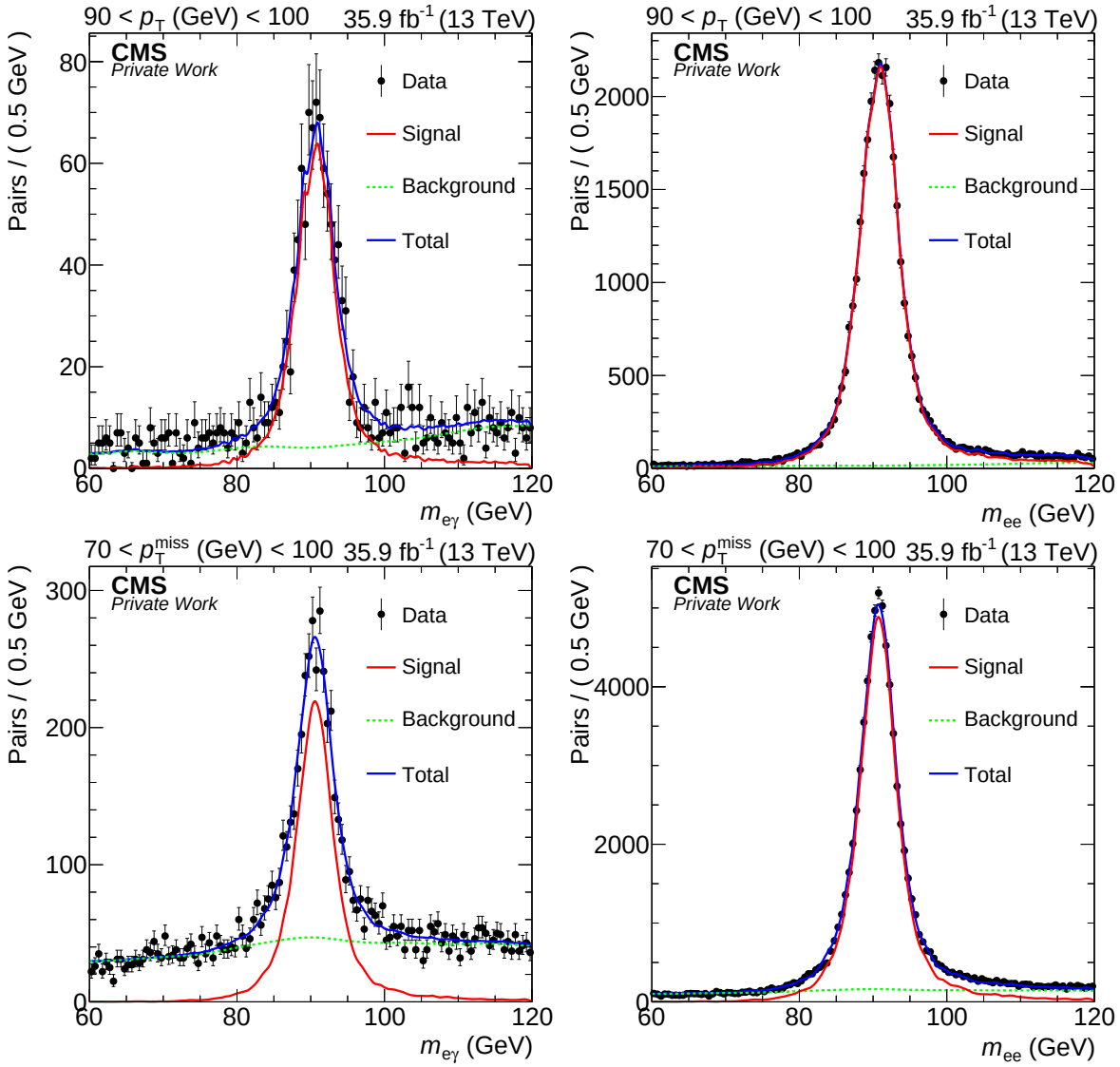

Figure 5.13: The signal and background shape fitted to the invariant mass of tag and probe pairs for the $e\gamma$ selection (left) and ee selection (right) for events with $90 < p_T < 100\,\text{GeV}$ (top) and $70 < p_T^{\text{miss}} < 100\,\text{GeV}$ (bottom).

a strong correlation between vertex multiplicity and $R_{\gamma/e}$. Parametrizing $R_{\gamma/e}$ as a function of the vertex multiplicity however is not necessary, as the vertex multiplicity is the same in the $Z \to ee$ selection, the electron CR, and in the search region.

No dependency on H_T^γ or the jet multiplicity is observed. As the background is small compared to the other backgrounds, a relative uncertainty of 30% is used to cover all possible dependencies.

For the estimated of $R_{\gamma/e}$ in the published analysis [1], the latest energy corrections and calibrations at that time were used. In this section, the calculation was redone using the latest energy corrections and calibrations. To be consistent with the published results, the value used in the published paper is used:

$$R_{\gamma/e} = (2.7 \pm 0.8)\%.$$

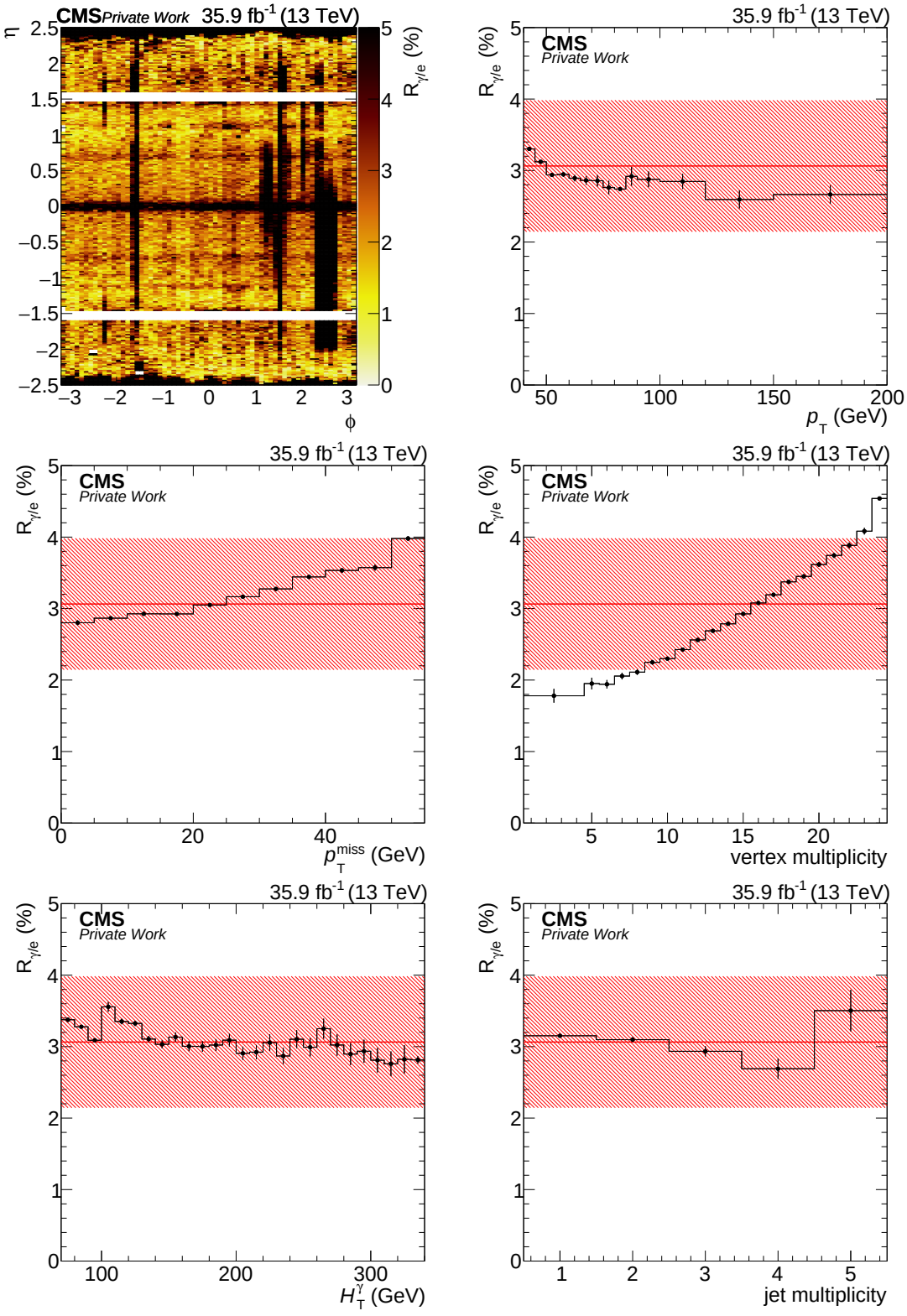

Figure 5.14: The $R_{\gamma/e}$ as a function of η and ϕ (top left), p_{T} (top right), $p_{\mathrm{T}}^{\mathrm{miss}}$ (middle left), vertex multiplicity (middle right), H_{T}^{γ} (bottom left), and jet multiplicity (bottom right). The mean value of the $R_{\gamma/e}$ is displayed as red horizontal line, while the relative systematic uncertainty is displayed as red hatched area.

This value is consistent with the updated value within its uncertainty, and as the contribution of this background is small, the updated values of $R_{\gamma/e}$ does not change the final results significantly.

5.3.3 Validation with simulated events

The method is applied to simulated W boson and $t\bar{t}$ events. The contributions of other processes, like multijet events or $Z \to ee$ events are negligible. The electron CR from simulation is scaled by $R^{\text{sim}}_{\gamma/e}$ and compared to the direct simulation of electrons reconstructed as photons without pixel-seeds. A match of the reconstructed photon to a generated electron within $\Delta R < 0.15$ and

$$\left| \frac{p_{\text{T}}^{\text{reconstructed photon}}}{p_{\text{T}}^{\text{generated electron}}} - 1 \right| < 15\%$$

is required to omit photons radiated from electrons or photons radiated from initial state particles.

The comparison of the direct simulation to the prediction from simulation is shown in figures 5.15 and 5.16. The statistical uncertainty in the prediction is negligible, as the number of events in the electron CR is much larger than the number of events in which an electron is misreconstructed as a photon. Agreement is observed within the uncertainty. The trend seen in $R_{\gamma/e}$ as a function of $p_{\text{T}}^{\text{miss}}$ in $Z \to ee$ events in data cannot be confirmed. There is also no trend with respect to the jet multiplicity, reflecting the same behavior as in the $R_{\gamma/e}$ measurement in data. As in the measurement of $R_{\gamma/e}$ as a function of p_{T}, there is a small trend in the validation as a function of p_{T}. The validation was done in several more variables all justifying the value and the uncertainty in $R_{\gamma/e}$.

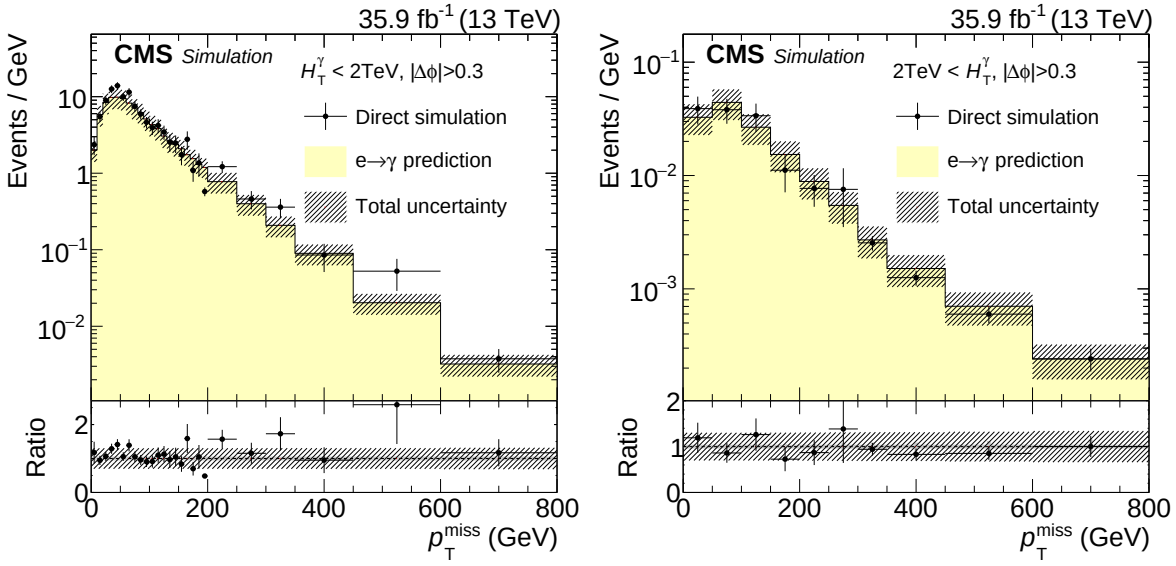

Figure 5.15: Validation of the background estimation method for electrons misreconstructed as photons using W and $t\bar{t}$ simulation. The $p_{\text{T}}^{\text{miss}}$ distribution in the low- (high-) H_{T}^{γ} selection is shown on the left (right) [1].

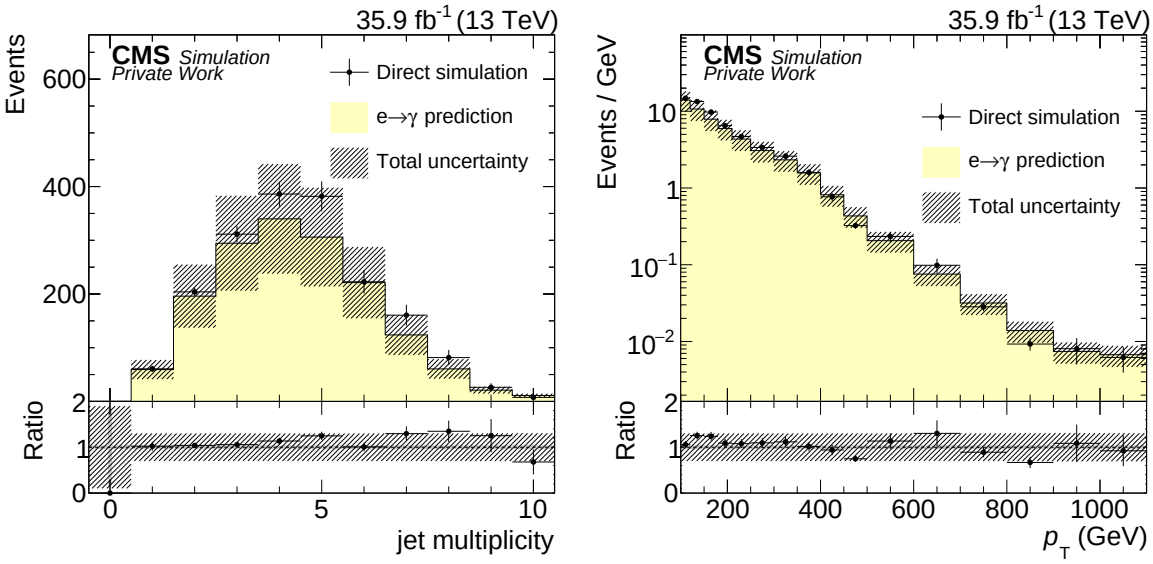

Figure 5.16: Validation of the background estimation method for electrons misreconstructed as photons using simulated W and $t\bar{t}$ events as a function of jet multiplicity (left) and electron p_{T} (right). To decrease the statistical uncertainty, no requirement on $p_{\mathrm{T}}^{\mathrm{miss}}$ is made.

5.4 Residual background contribution

SM processes contributing to the search regions not estimated with the methods described above are $\gamma W \to \gamma\ell\nu$, $\gamma Z \to \gamma\nu\nu$, and $\gamma t\bar{t}$. If a jet is misidentified as a photon, also $W \to \ell\nu$, $Z \to \nu\nu$, and $t\bar{t}$ processes can contribute.

The following processes are generated at hard scattering level: $t\bar{t}$, $\gamma t\bar{t}$, $W(\ell\nu)$, $\gamma W \to \gamma\ell\nu$, $Z \to \nu\nu$, and $\gamma Z \to \gamma\nu\nu$. Events without photons in the hard scattering can still radiate photons in the showering step of the event generation. The overlap between the direct simulation in the hard scattering and the photon production in the shower is considered by removing all prompt photons from the samples without generated photon in the hard scattering. Prompt photons are photons which are separated from generated quarks, gluons and leptons by $\Delta R > 0.4$. Approximately 1% of the events without photons in the hard scattering are removed by this requirement. In the following, events with and without photons in the hard scattering are grouped. Events in which the selected photon is matched to a generated electron are removed, as the contribution of such events is covered by the background estimation method described in section 5.3.

The contributions of a single top with associated photon production and $Z \to \ell\ell$ processes was studied and found to be negligible. Processes with hadronically decaying W or Z bosons enter the search region through nongenuine $p_{\mathrm{T}}^{\mathrm{miss}}$, and are covered by the background estimation method discussed in section 5.2.

For events with real photons and genuine $p_{\mathrm{T}}^{\mathrm{miss}}$, the simulation agrees very well with the measured data [124–126]. In addition, the processes discussed in this section are theoretically well understood, and the cross sections can be calculated with at least NLO accuracy.

Simulation is not used to predict the event yield of SM processes with non-genuine $p_{\mathrm{T}}^{\mathrm{miss}}$ as described in the section 5.2, as non-genuine $p_{\mathrm{T}}^{\mathrm{miss}}$ is not as well modeled as genuine $p_{\mathrm{T}}^{\mathrm{miss}}$ by the simulation. Also no simulation is used to predict the event yield of events with electrons

misreconstructed as photons, as the probability of the misreconstruction differs between data and simulation.

The simulated event yield for the processes discussed in this section is scaled by the trigger efficiency described in section 4.4. In addition, the simulated efficiencies for the identification and reconstruction differ, which is also corrected for using scale factors. This is discussed in the following subsection.

5.4.1 Efficiency corrections for simulation

The reconstruction and identification efficiencies differ between data and simulation. To improve the matching between data and simulation, simulated events are weighted by the ratio of the measured to simulated reconstruction and identification efficiencies.

As photons and electrons behave similarly in their calorimetric response, the reconstruction and identification efficiencies excluding the pixel-seed veto are determined using the tag-and-probe method on $Z \to ee$ events. To estimate the selection efficiency of the pixel-seed veto, a tag-and-probe method is used on $Z \to \mu\mu\gamma$ events as described in section 4.3.

The reconstruction and identification efficiency excluding the electron veto is around 90% for both simulation and data. The efficiency ratio is around 1.02 ± 0.03, depending on p_{T} and η [108]. The efficiency ratio for the pixel-seed veto is 0.998 ± 0.013 for photons reconstructed in the barrel and 0.993 ± 0.025 for photons reconstructed in the endcaps [127].

5.4.2 Systematic uncertainties

The uncertainties in the trigger efficiency and in the simulated selection efficiency are the same in each of the six search regions, as is the uncertainty in the luminosity (2.5%). The uncertainties discussed in this section are evaluated in each search region and for each process independently.

The uncertainty in the renormalization scale μ_r and factorization scale μ_f is estimated by varying the scales by 0.5 and 2 [128, 129]. The largest upward variations are obtained with $\mu_r = \mu_f = 0.5$, and the largest downward variation with $\mu_r = \mu_f = 2$. Half of the difference is taken as systematic uncertainty, which corresponds to a relative uncertainty of about 20%. The $p_{\mathrm{T}}^{\mathrm{miss}}$ distributions for γW events in the low-H_{T}^{γ} region for various μ_r and μ_f are shown in figure 5.17 (top left). In the bottom panel of each plot, the relative systematic (statistical) uncertainty is shown as hatched area (vertical line) in each interval of $p_{\mathrm{T}}^{\mathrm{miss}}$.

The uncertainty in the PDF is estimated according to the PDF4LHC recommendations [130]. Before the incorporation of the LHC data of the year 2012, the most popular PDF sets did not agree with each other, and the uncertainty in the PDFs was estimated using several PDF sets. As now the LHC data are dominating most of the phase space, the most popular PDF sets agree within the uncertainties. For this analysis, the NNPDF 3.0 [82] set is used. To evaluate the uncertainty, 100 replicas of the nominal PDF set are generated using the MC method. The event yield in the search regions is calculated for each replica, and the uncertainty in a search region corresponds to the standard deviation of the event yields from the 100 replicas. In the top right plot of figure 5.17, the $p_{\mathrm{T}}^{\mathrm{miss}}$ distribution of the 100 PDF replicas is shown for γW events in the low-H_{T}^{γ} region, while the ratio plot shows the uncertainty. The relative uncertainty is about 5–10%.

As explained in section 4.1, simulated events are reweighted such that their pileup distribution matches the measured one. The pileup distribution of the data depends on the total inelastic

proton-proton cross section. The reweighting is done with the cross section shifted by its uncertainty up- and downwards, and the reweighted $p_{\mathrm{T}}^{\mathrm{miss}}$ distributions are used to determine the uncertainty in the search regions, which is about 0.2–6%. This is shown in the bottom left plot of figure 5.17 for γW events in the low-H_{T}^{γ} region.

The uncertainties in the jet energy scale and resolution are propagated to $p_{\mathrm{T}}^{\mathrm{miss}}$ and the event yields with upward and downward shifted jet energy scale and resolution are used to derive the uncertainty, as shown in the bottom right of figure 5.17 for γW events in the low-H_{T}^{γ} region. The size of this uncertainty is about 2–20%.

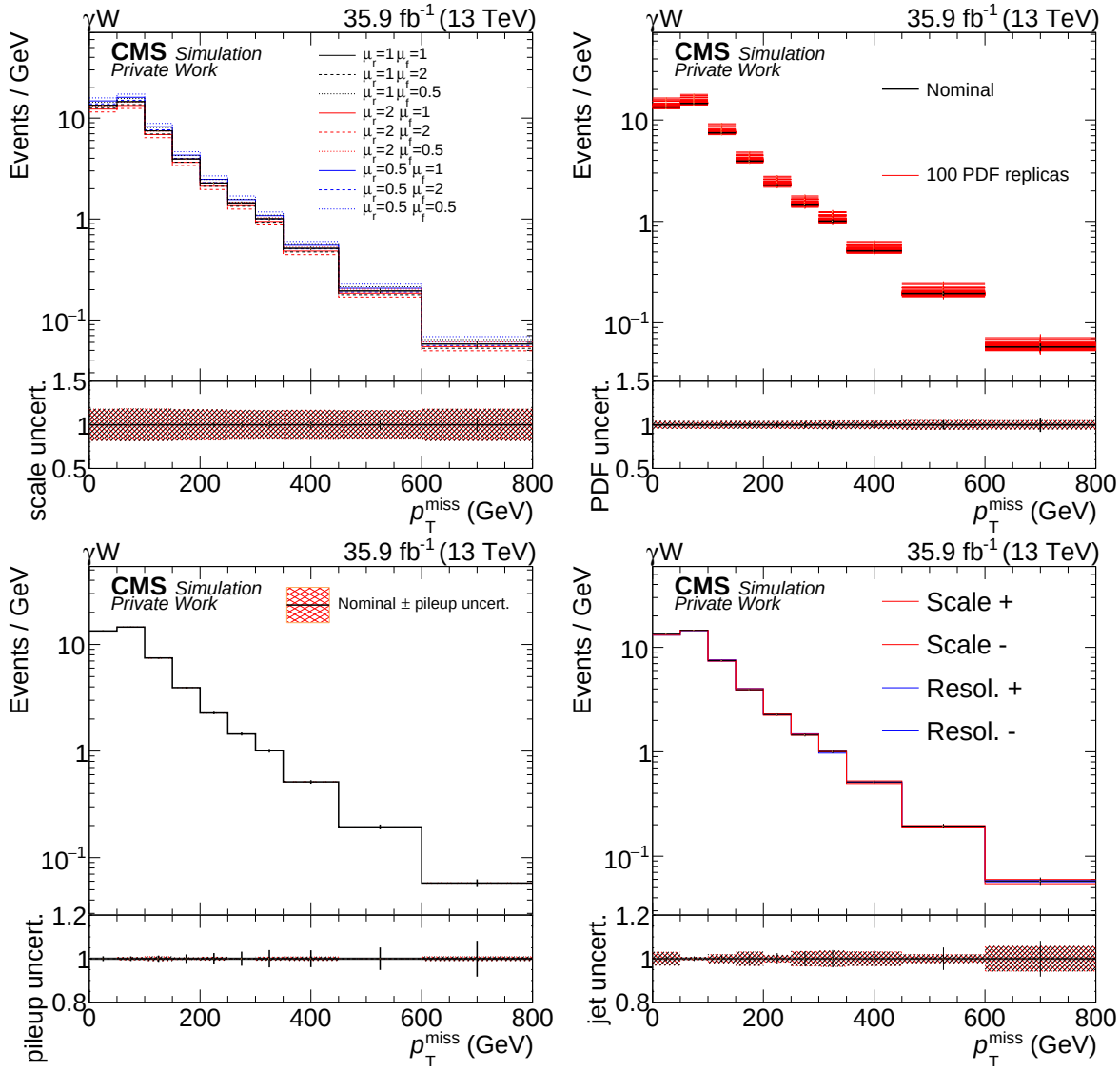

Figure 5.17: The $p_{\mathrm{T}}^{\mathrm{miss}}$ distributions for variations in the scale (top left), the PDF (top right), the pileup (bottom left), and the jet energy scale and resolution (bottom right) for γW simulation in the low-H_{T}^{γ} selection. In the ratio plots, the relative uncertainties are given in each interval of $p_{\mathrm{T}}^{\mathrm{miss}}$. The nominal distribution is not changed, and the uncertainties are defined to be symmetrical with respect to the nominal value in each interval. Similar plots for other processes and the high-H_{T}^{γ} selection are shown in appendix A.4.

For comparison, the statistical uncertainty for each process in the high-H_{T}^{γ} selection is about 20–50%. For the low-H_{T}^{γ} selection, the statistical uncertainty in γW and γZ is about 4–8%, and for $\gamma t\bar{t}$ about 10–20%.

5.5 Further validation of the background estimation methods

The background estimation and definition of the search regions was developed before data yields in the search regions were known (blind analysis). This ensures that the analysis team is not biased due to the knowledge of the results. Before the event yields in the search regions were counted, the methods were applied to event selections which have no or only minor signal contribution (estimated from signal simulation), but are as close as possible to the search regions. In doing so, the correctness of the background estimation methods can be checked.

In the previous sections, the validation of the background estimation methods relying on CRs was performed on a subset of simulated events. In addition, three further tests are done: Firstly, all methods are applied to all simulated samples simultaneously, to check for possible effects due to the mixing of different processes. Secondly, the background estimation methods are applied in a signal depleted validation region in data with medium $p_{\mathrm{T}}^{\mathrm{miss}}$, and thirdly the methods are applied using data events in which the photon was reconstructed in the EE.

5.5.1 Validation using simulated events

Similar to the validation in sections 5.2.5 and 5.3.3, simulated events are treated like data, and compared to the prediction from simulation. In this test, all SM samples are added, and no further generator information of the CR is used. This means that the electron CR and the jet CR are populated by events not included in the validation tests shown in sections 5.2.5 and 5.3.3. The comparison of direct simulation and prediction from simulation is shown in figure 5.18. The $p_{\mathrm{T}}^{\mathrm{miss}}$ distributions in the presence of two signal scenarios are shown in addition. The good agreement between direct simulation and prediction from simulation shows that the methods works as expected, even if the CRs are populated by events not present in the separate validations of the individual background estimation methods.

5.5.2 Validation using moderate-$p_{\mathrm{T}}^{\mathrm{miss}}$ events

The normalization of the nongenuine $p_{\mathrm{T}}^{\mathrm{miss}}$ background is estimated from events with photons and $p_{\mathrm{T}}^{\mathrm{miss}} < 100\,\mathrm{GeV}$, while $p_{\mathrm{T}}^{\mathrm{miss}} > 350\,\mathrm{GeV}$ is required for the search region. This allows the definition of a validation region using events with $100 < p_{\mathrm{T}}^{\mathrm{miss}} < 350\,\mathrm{GeV}$. The agreement in this region with the background prediction is shown in figure 5.19. The data yield is not shown in the three highest $p_{\mathrm{T}}^{\mathrm{miss}}$ intervals, as they correspond to the search regions. A small excess of events with $p_{\mathrm{T}}^{\mathrm{miss}} \approx 180\,\mathrm{GeV}$ is observed in the low-H_{T}^{γ} selection, which is however fully covered by the background uncertainty.

5.5.3 Validation using events with endcap photons

Events in the search regions are required to have at least one photon reconstructed in the EB. Events in which no photon with $p_{\mathrm{T}} > 100\,\mathrm{GeV}$ is reconstructed in the EB, but in the EE are used as a further validation region (EE selection). As shown in section 5.1, photons from signal events tend to be reconstructed in the EB instead of the EE.

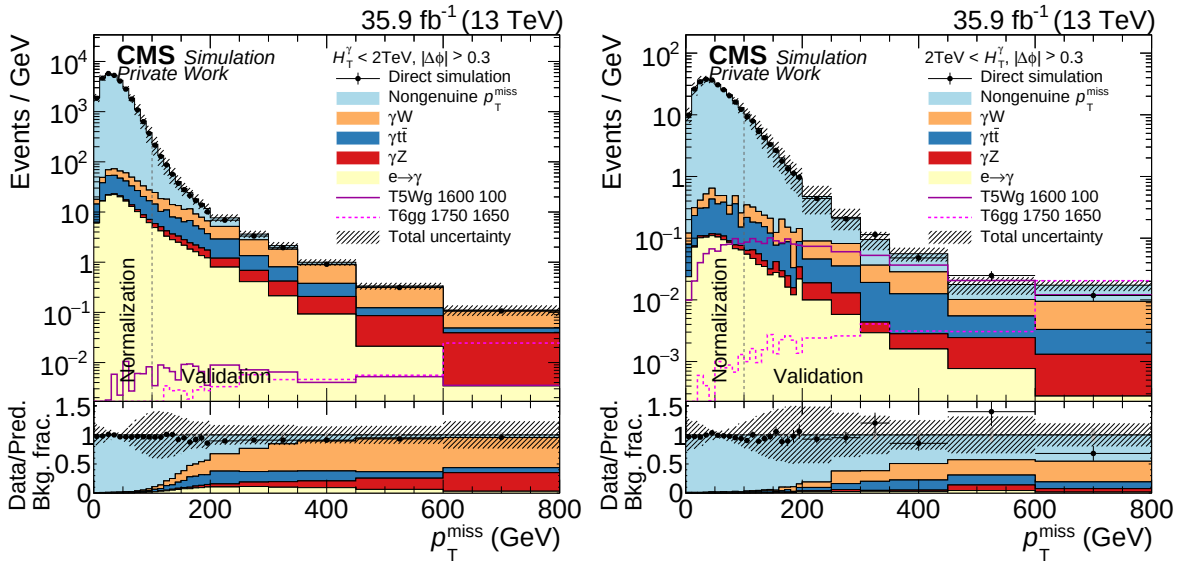

Figure 5.18: Comparison of the p_T^{miss} distribution as simulated (black dots) to the prediction as estimated from simulation (filled histograms) for the low- (high-) H_T^γ selection on the left (right). The expectation for the gluino-single-photon signal scenario with a gluino mass of 1600 GeV and a gaugino mass of 100 GeV and the squark-diphoton signal scenario with a squark mass of 1750 GeV and a neutralino mass of 1650 GeV are shown in addition [1].

The analysis is repeated with the EE selection. The jet CR is the same as for the nominal selection, however, different scale and normalization factors are used. The scale factor determination (similar to figure 5.8) for the validation is shown in appendix A.3. The electron CR is defined with an electron reconstructed in the same EE η range as photon candidates. The $R_{\gamma/e}$ is evaluated using the electrons in the same η range, and is $(2.4 \pm 0.7)\%$. For the residual background contribution, which is estimated from simulation, the trigger efficiency of $(95.0 \pm 3.8)\%$ is used for photons reconstructed in the EE. The evaluation of the yields and uncertainties of the residual background contributions estimated using simulation is estimated similarly to the yields and the uncertainties for the search region. The comparison of the data to the predicted SM background and two signal scenarios is shown in figure 5.20.

As expected, the contribution of the SUSY models to the EE validation region is small. The observed data agree with the SM prediction. In the low-H_T^γ selection for $p_T^{miss} \approx 140$ GeV, the observed data are systematically below the prediction, but still within the systematic uncertainty assigned to the prediction. In this p_T^{miss} region, the background prediction looks smoother in this region than the observed data, hinting that this may be a statistical fluctuation of the data and no effect of the background prediction.

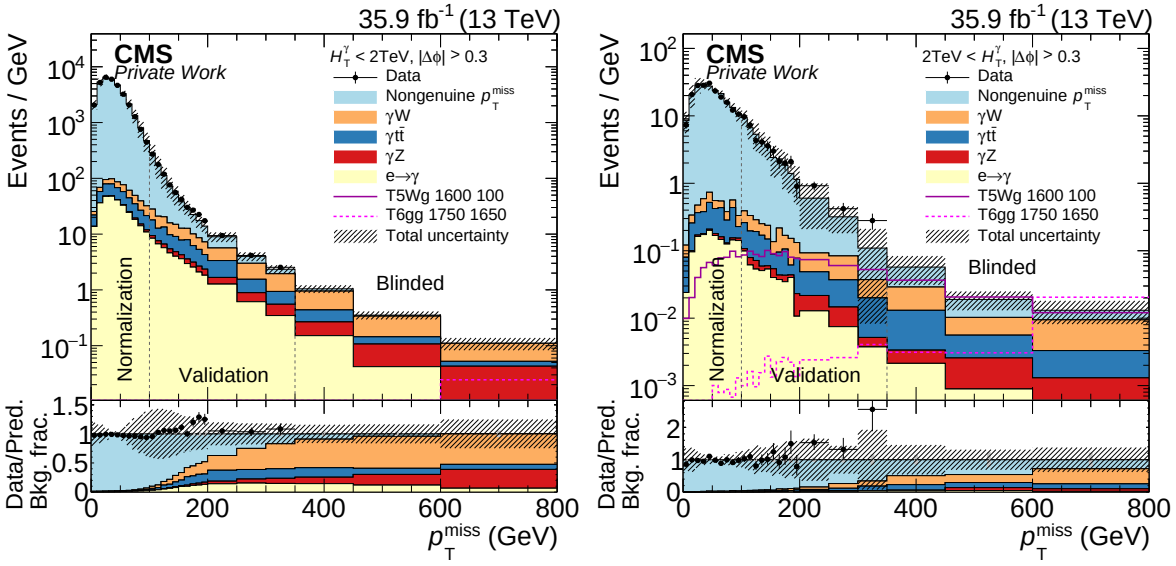

Figure 5.19: Observed data in the low-$p_{\mathrm{T}}^{\mathrm{miss}}$ region and the moderate-$p_{\mathrm{T}}^{\mathrm{miss}}$ validation region compared to the background prediction for the low-H_{T}^{γ} selection (left) and the high-H_{T}^{γ} selection (right). The data event yields for $p_{\mathrm{T}}^{\mathrm{miss}} > 350\,\mathrm{GeV}$ are not shown. The expectation for the gluino-single-photon signal scenario with a gluino mass of 1600 GeV and a gaugino mass of 100 GeV and the squark-diphoton signal scenario with a squark mass of 1750 GeV and a neutralino mass of 1650 GeV are shown in addition. Only the latter of the signal scenarios contributes non-negligibly to the highest $p_{\mathrm{T}}^{\mathrm{miss}}$ search region of the low-H_{T}^{γ} selection.

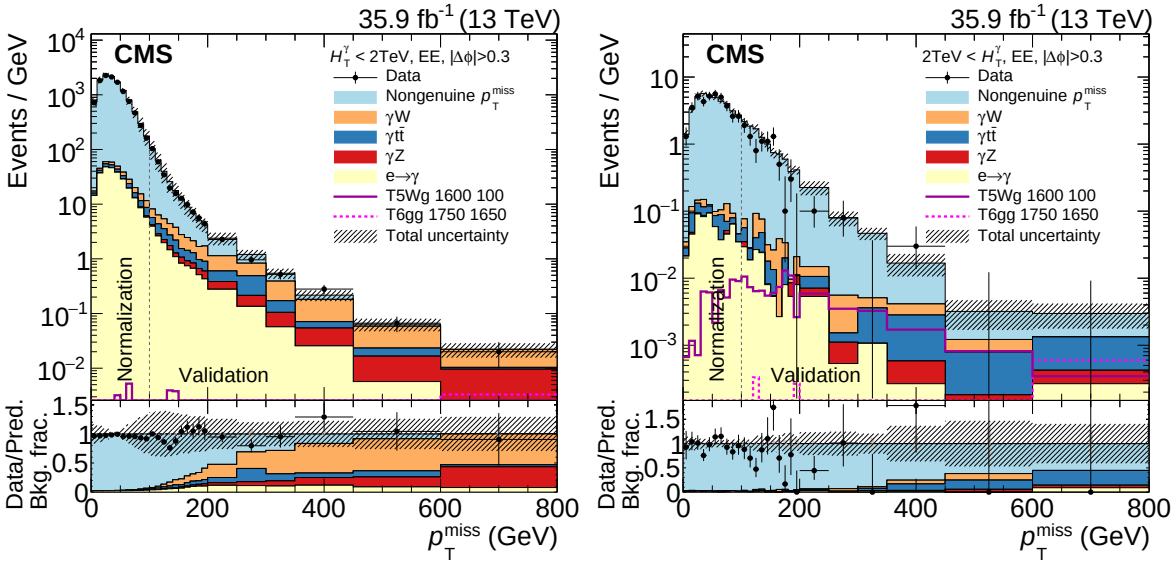

Figure 5.20: Observed events with photons reconstructed in the EE compared to the SM prediction for the low- (high-) H_{T}^{γ} selection on the left (right). The expectation for the gluino-single-photon signal scenario with a gluino mass of 1600 GeV and a gaugino mass of 100 GeV and the squark-diphoton signal scenario with a squark mass of 1750 GeV and a neutralino mass of 1650 GeV are shown in addition [1].

6 Results and interpretation

In this section, the results of the analysis in the search region are reported and the interpretation in terms of SUSY models is discussed. All figures are created by the author, and some of them are also published in reference [1].

6.1 Results

The data compared to the SM background expectation are shown in figure 6.1. The last three bins define the search regions, while the intermediate $p_{\mathrm{T}}^{\mathrm{miss}}$ region is used to validate the background estimation methods. The event yield in the search regions, the background composition and the expected signal yield for one of the models are presented in table 6.1. The low-H_{T}^{γ} search regions are dominated by γW events, while the high-H_{T}^{γ} search regions by events with nongenuine $p_{\mathrm{T}}^{\mathrm{miss}}$ and γW. The relative contribution of $\gamma Z \to \gamma\nu\nu$ increases with increasing $p_{\mathrm{T}}^{\mathrm{miss}}$, and is more dominant in the low-H_{T}^{γ} selection than in the high-H_{T}^{γ} selection. The relative contribution of $\gamma t\bar{t}$ events is larger in the high-H_{T}^{γ} selection than in the low-H_{T}^{γ} selection. The contribution of electrons reconstructed as photons is small in all search regions. For the SM background expectation, the quadratic sum of statistical and systematic uncertainties is given.

Table 6.1: Observed data compared to the background prediction and the expected signal yields for the gluino-single-photon model with $m_{\tilde{g}} = 1600\,\mathrm{GeV}$ and $m_{\tilde{\chi}_1} = 100\,\mathrm{GeV}$. The quadratic sum of statistical and systematic uncertainties are given. For the signal model, only experimental uncertainties are stated.

H_{T}^{γ} (GeV)	<2000			>2000		
$p_{\mathrm{T}}^{\mathrm{miss}}$ (GeV)	(350, 450)	(450, 600)	>600	(350, 450)	(450, 600)	>600
Nong. $p_{\mathrm{T}}^{\mathrm{miss}}$	$9.6\,^{+\,11.1}_{-\,9.6}$	$2.2\,^{+\,5.5}_{-\,2.2}$	< 0.1	2.83 ± 2.51	1.31 ± 0.74	$0.73\,^{+\,0.86}_{-\,0.73}$
γW	51.3 ± 9.7	29.1 ± 5.5	11.6 ± 2.5	1.58 ± 0.58	0.70 ± 0.37	1.23 ± 0.43
$\gamma t\bar{t}$	17.1 ± 5.4	5.6 ± 2.6	1.9 ± 0.4	0.97 ± 0.38	0.45 ± 0.29	0.40 ± 0.22
γZ	11.5 ± 2.4	9.7 ± 1.8	7.1 ± 1.4	0.12 ± 0.07	0.25 ± 0.11	0.21 ± 0.10
$e \to \gamma$	15.1 ± 4.6	6.3 ± 1.9	1.4 ± 0.5	0.21 ± 0.10	0.13 ± 0.07	0.05 ± 0.04
Total bkg.	104.6 ± 16.5	53.0 ± 8.6	22.0 ± 3.0	5.72 ± 2.60	2.84 ± 0.89	2.62 ± 0.99
Data	103	82	21	6	10	4
Signal	0.4 ± 0.1	0.8 ± 0.1	0.7 ± 0.1	3.66 ± 0.40	3.09 ± 0.40	2.41 ± 0.32

The observed data agree within the expectation within the uncertainties, except for $450 < p_{\mathrm{T}}^{\mathrm{miss}} < 600\,\mathrm{GeV}$ for both the low- and the high-H_{T}^{γ} selection, where 1.9 and 2.7 local standard deviations are observed, respectively. Due to the fact that there is no excess for events with larger $p_{\mathrm{T}}^{\mathrm{miss}}$, it is assumed to be a statistical fluctuation. Typical BSM scenarios cause a broad excess in $p_{\mathrm{T}}^{\mathrm{miss}}$, and not a peak-like structure as a function of $p_{\mathrm{T}}^{\mathrm{miss}}$.

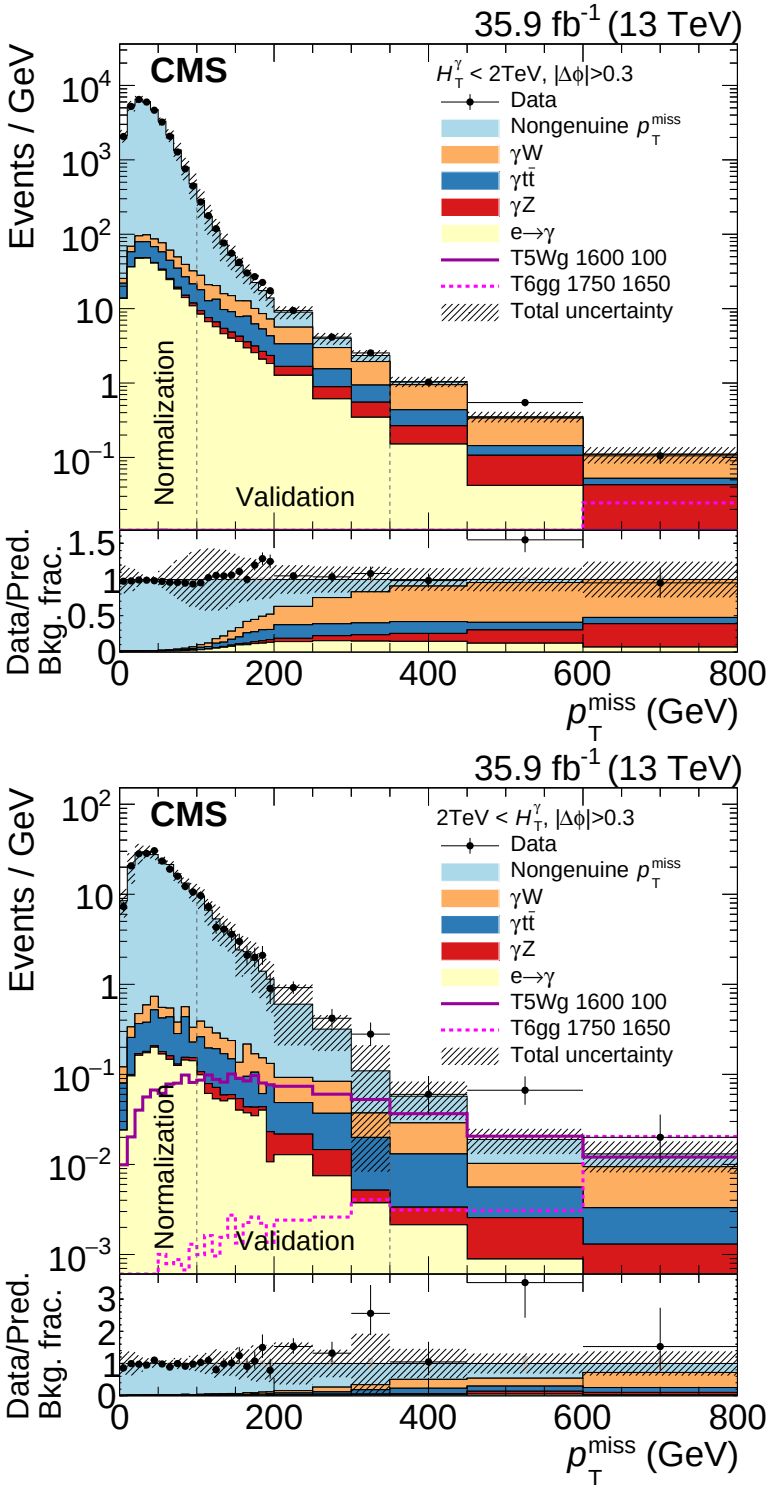

Figure 6.1: Observed data compared to the background prediction for the low-H_{T}^{γ} selection (top) and the high-H_{T}^{γ} selection (bottom). The expectation for the gluino-single-photon signal scenario with a gluino mass of 1600 GeV and a gaugino mass of 100 GeV and the squark-diphoton signal scenario with a squark mass of 1750 GeV and a neutralino mass of 1650 GeV are shown in addition. Only the latter of the signal scenarios contributes non-negligibly to the highest $p_{\mathrm{T}}^{\mathrm{miss}}$ search region of the low-H_{T}^{γ} selection [1].

6.2 Signal acceptance and uncertainties

The expected signal yield is predicted using simulation. Squark (gluino) production with squark (gluino) masses from 1000–2050 (800–2500) GeV is simulated in steps of 50 or 100 GeV. Events are generated with gaugino masses in steps of 100 GeV. To improve the description at very low and very high gaugino masses, gaugino masses of 10, 25, 50, 150, $m_{\tilde{g}/\tilde{q}} - 150$, $m_{\tilde{g}/\tilde{q}} - 50$, $m_{\tilde{g}/\tilde{q}} - 25$, and $m_{\tilde{g}/\tilde{q}} - 10$ GeV are simulated in addition, where $m_{\tilde{g}/\tilde{q}}$ is either the corresponding gluino or squark mass. Charginos with $m_{\tilde{\chi}_1^\pm} < m_W$ decay in a three-body decay into two SM fermions and a gravitino, with branching fractions mirroring the SM W boson decay.

The event yield for the gluino-single-photon model with $m_{\tilde{g}} = 1600$ GeV and $m_{\tilde{\chi}_1} = 100$ GeV is shown in figure 6.2 after the most important analysis selections for an integrated luminosity of 35.9 fb^{-1}. The number of events which would have been produced in the collisions is given in the first bin. The second bin contains events in which a reconstructed photon with the criteria defined in the analysis is reconstructed. The third bin contains events which fulfill $H_\mathrm{T}^\gamma > 700$ GeV and contain a photon. In nearly all events of this signal point, H_T^γ exceeds 700 GeV. The fourth bin contains events with a reconstructed photon, $H_\mathrm{T}^\gamma > 700$ GeV, and $|\Delta\Phi(\vec{p}_\mathrm{T}^\gamma, \pm\vec{p}_\mathrm{T}^\mathrm{miss})| > 0.3$. The last six bins show the event yields in the search regions.

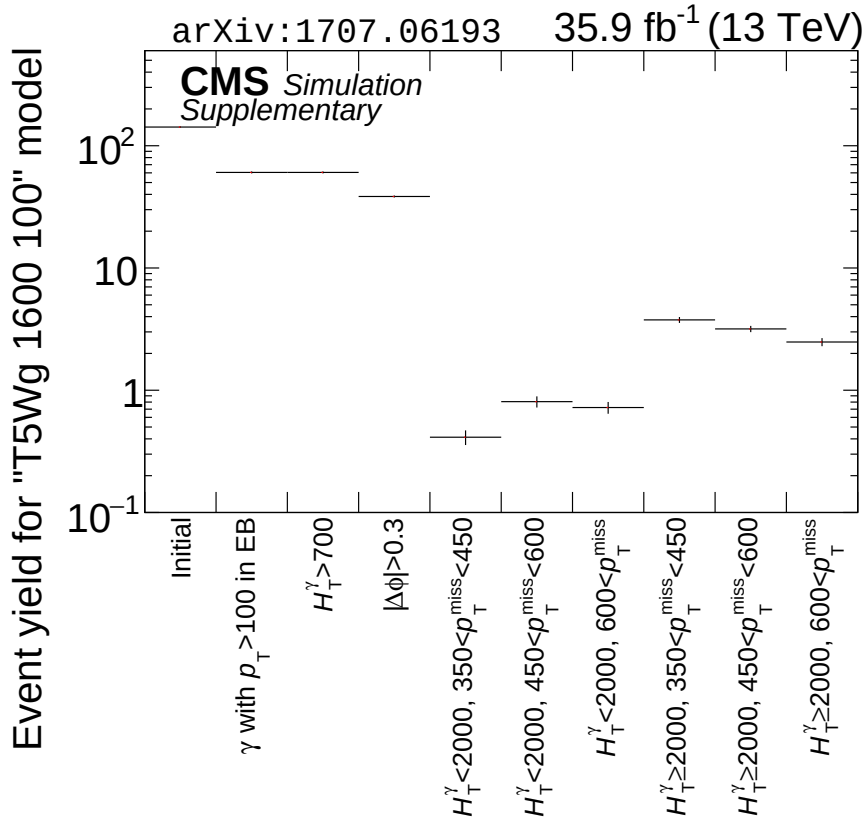

Figure 6.2: Event yields for the gluino-single-photon model with $m_{\tilde{g}} = 1600$ GeV and $m_{\tilde{\chi}_1} = 100$ GeV for various selections of the analysis for an integrated luminosity of 35.9 fb^{-1}. The values of p_T, H_T^γ, and $p_\mathrm{T}^\mathrm{miss}$ are given in GeV. This figure is also published as additional material of reference [1].

The acceptance (number of events in the corresponding search region divided by the total number of produced events) is shown in figure 6.3 as function of gluino and gaugino mass for the

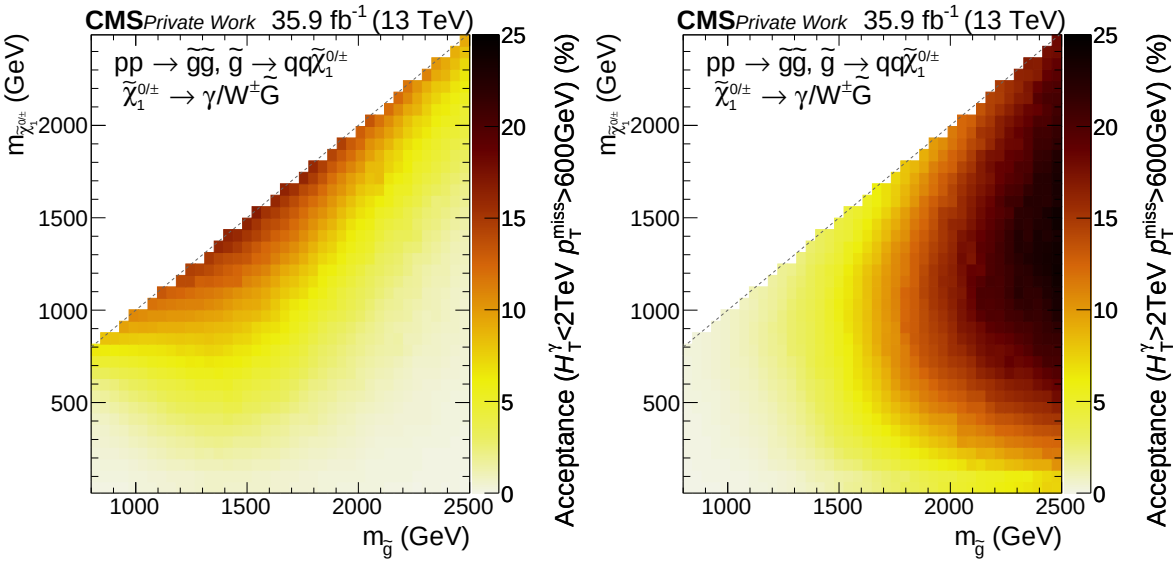

Figure 6.3: Acceptance for the gluino-single-photon model in the search regions with $p_{\mathrm{T}}^{\mathrm{miss}} > 600\,\mathrm{GeV}$, and $H_{\mathrm{T}}^{\gamma} < 2\,\mathrm{TeV}$ (left) or $H_{\mathrm{T}}^{\gamma} > 2\,\mathrm{TeV}$ (right), respectively.

gluino-single-photon model for the two search regions with $p_{\mathrm{T}}^{\mathrm{miss}} > 350\,\mathrm{GeV}$, and $H_{\mathrm{T}}^{\gamma} < 2\,\mathrm{TeV}$ or $H_{\mathrm{T}}^{\gamma} > 2\,\mathrm{TeV}$, respectively. The acceptance in the low-H_{T}^{γ} selection is large in scenarios in which the gaugino mass is close to the gluino mass, since little energy is transfered to jets and the events contain a large amount of $p_{\mathrm{T}}^{\mathrm{miss}}$. The acceptance drops for high gluino masses, as also more H_{T}^{γ} is reconstructed. The acceptance in the high-H_{T}^{γ} selection is large in scenarios with large gluino masses. It decreases with decreasing gaugino mass, but not as strongly as the acceptance of the low-H_{T}^{γ} selection. For the other models, and the search regions with mediate $p_{\mathrm{T}}^{\mathrm{miss}}$, a similar behavior is observed.

The uncertainties in the signal yield are split into experimental uncertainties and theoretical uncertainties in the SUSY production cross section. The theoretical uncertainties are taken from reference [131], based on variations of the renormalization scale, factorization scale, and PDFs. The uncertainties impact the yield of the signal scenarios, but not the shape of the distributions. The signal cross sections and their theoretical uncertainties are shown in figure 6.4. The cross sections are calculated with next-to-leading logarithmic (NLL) accuracy matched to NLO predictions [132].

The experimental uncertainties are evaluated similarly to the uncertainties in the simulated SM background: The uncertainty in the total integrated luminosity, the trigger efficiency, and jet energy scale and resolution are evaluated exactly as in section 5.4.2. The reconstruction and identification corrections for simulation also include scale factors for differences between the FastSim and the Geant4 simulation. Since all reconstructed physics objects are included in the computation of $p_{\mathrm{T}}^{\mathrm{miss}}$, it can be difficult to describe $p_{\mathrm{T}}^{\mathrm{miss}}$ with the CMS fast simulation. In the considered signal models, $p_{\mathrm{T}}^{\mathrm{miss}}$ is caused dominantly by the gravitons, so the full difference between the event yield of the reconstructed $p_{\mathrm{T}}^{\mathrm{miss}}$ distribution and the event yield of the generated $p_{\mathrm{T}}^{\mathrm{miss}}$ distribution is taken as additional uncertainty of about 0.5–6%. The uncertainties in the shape due to the renormalization and factorization scales are about 1%. For the PDFs, this uncertainty is negligible. The impact on the signal yield is covered by the theoretical uncertainties. To evaluate the uncertainty in pileup, events are divided into a high- and a low-pileup sample, and differences between these two are taken as uncertainty.

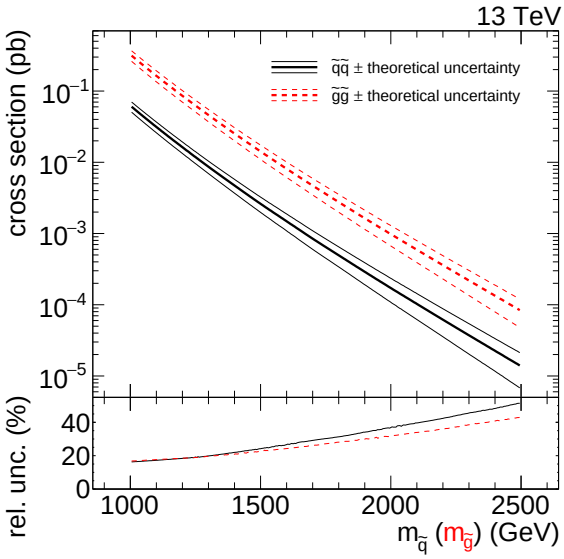

Figure 6.4: Gluino- and squark-pair production cross section as function of the sparticle mass. The bottom panel shows and the relative theoretical uncertainty in the cross section. For squark pair production, the cross section is determined assuming ten mass-degenerate squark states, corresponding to the SUSY partners of the left- and right-handed u, d, s, c, and b quarks.

The multiplicity of additional jets from initial state radiation (ISR) differs slightly between data and MadGraph simulation in $t\bar{t}$ and Z events. To improve on the MadGraph modelling of the multiplicity of ISR jets, simulated signal events are reweighted based on the number of ISR jets ($N_{\mathrm{J}}^{\mathrm{ISR}}$) so as to make the jet multiplicity in simulated $t\bar{t}$ samples agree with that in data. The reweighting factors vary between 0.92 and 0.51 for $N_{\mathrm{J}}^{\mathrm{ISR}}$ between 1 and 6. The reweighted distribution is then scaled such that the overall event yield corresponds to the event yield before the reweighting. One half of the deviation from unity is taken as the systematic uncertainty in these reweighting factors and results in an uncertainty of 0–10% in the signal efficiency. A summary of the uncertainties can be found in table 6.2. The quadratic sum of the experimental uncertainties for the gluino-single-photon model is shown in figure 6.5 for the highest-$p_{\mathrm{T}}^{\mathrm{miss}}$ and H_{T}^{γ} search region. In the region of the expected exclusion contour, the total experimental uncertainty is around 7%.

Table 6.2: Systematic uncertainties for background determined from CR in data (first two rows) and simulation (all other rows). The uncertainties marked with † affect the shape only, but not the overall normalization, as the uncertainty in the normalization is already included as theoretical uncertainty.

Source	Relative uncertainty (%) background	signal
Nongenuine $p_{\mathrm{T}}^{\mathrm{miss}}$ background	14–250	
$e \to \gamma$ background	30	
Integrated luminosity	2.5	2.5
Photon scale factors	2	2
Trigger	4	4
PDFs	5–10	0†
Renormalization/factorization scales	16–27	0–1†
Jet energy scale and resolution	2–20	1–6
Pileup	0.2–6	0.2–10
ISR		0–10
Fast simulation $p_{\mathrm{T}}^{\mathrm{miss}}$ modelling		0.5–6

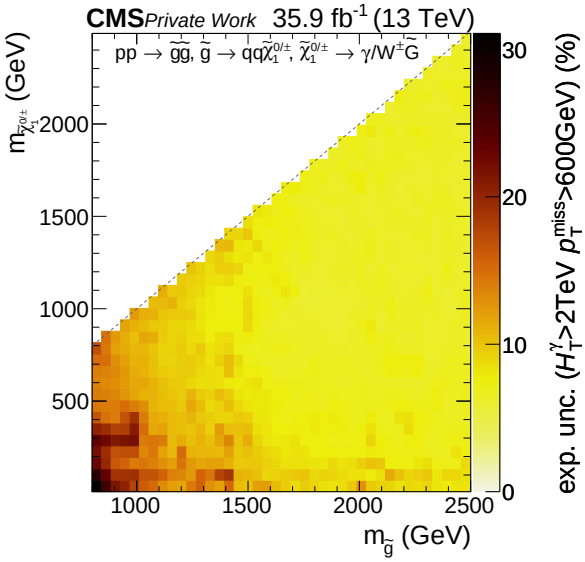

Figure 6.5: Total experimental uncertainties for the gluino-single-photon model in the highest-$p_{\mathrm{T}}^{\mathrm{miss}}$ and H_{T}^{γ} search region.

In the presence of signal, the background prediction can be altered, as data events are used for the background estimate with data CRs. Since hardly any electrons are present in the signal scenarios, the contribution from the electron CR can be neglected. If a signal event is reconstructed with all photons outside of the detector acceptance or with $p_{\mathrm{T}} < 100\,\mathrm{GeV}$, the event is selected in the jet CR. Signal events have large values of $p_{\mathrm{T}}^{\mathrm{miss}}$, therefore they do not alter the scale factor or the normalization determined in events with $p_{\mathrm{T}}^{\mathrm{miss}} < 100\,\mathrm{GeV}$. For the gluino-single-photon model with a gluino (gaugino) mass of 1600 (100) GeV, 2.5 events with $p_{\mathrm{T}}^{\mathrm{miss}} > 350\,\mathrm{GeV}$ and $H_{\mathrm{T}}^{\gamma} > 2000\,\mathrm{GeV}$ are expected in the jet CR (as many as in the corresponding search region). As there are much more events in the jet CR than in the photon CR, the normalization factor is small. This leads to a prediction of $9.27 \cdot 10^{-3}$ events in addition to the 0.73 events expected from SM processes with nongenuine $p_{\mathrm{T}}^{\mathrm{miss}}$ in the same search region. The overprediction normalized to the signal yield (signal contamination) is shown in figure 6.6 for the most sensitive bin for the squark-diphoton model and the gluino-single-photon model. It is similar in other models and search regions, and is about 0.1%, except for small gaugino masses, where the photons have less p_{T}, leading to a signal contamination of about 0.6%. E.g. for a signal contamination of 100%, there are as many additional events predicted by the background estimation methods as there are in the search region, so in this case it is impossible to find signal.

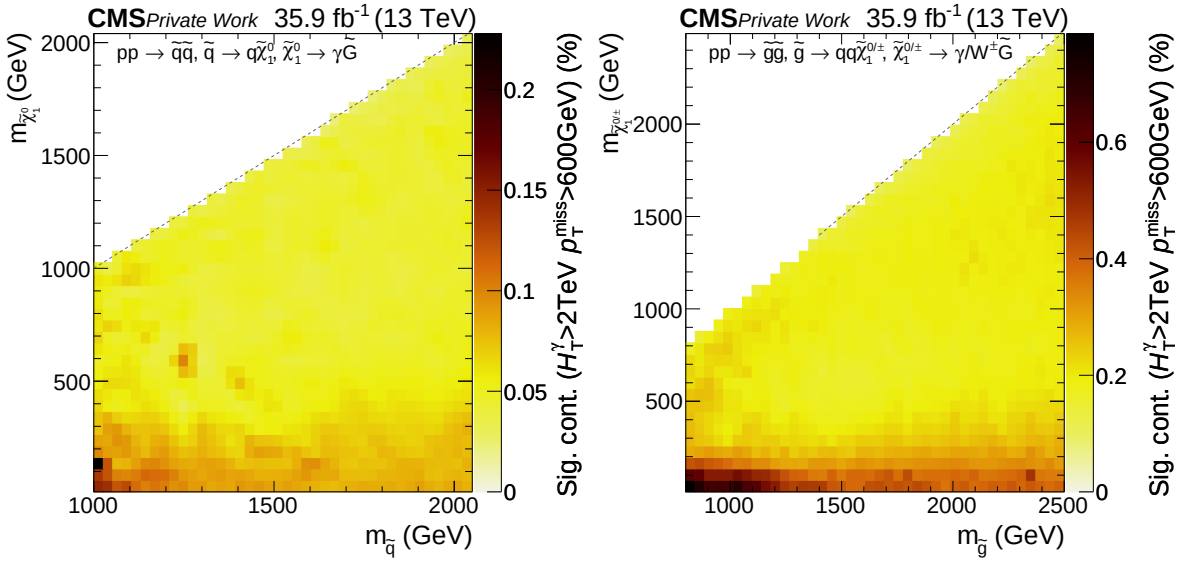

Figure 6.6: Signal contamination for the squark-diphoton (left) gluino-single-photon (right) model for the high-$p_{\mathrm{T}}^{\mathrm{miss}}$ and high-H_{T}^{γ} search region.

6.3 Calculation of the exclusion limits

The 95% confidence level (CL) upper limits on the SUSY cross sections are calculated with the $\mathrm{CL_s}$ criterion [133, 134] using the LHC-style profile likelihood ratio as test statistic [135] evaluated in asymptotic approximation [119].

The likelihood observing the data given the signal and background predictions is given by

$$L(\mathrm{data}|\mu,\theta) = \prod_{i=1}^{6} P\left(\mathrm{data}_i|\mu s_i(\theta) + b_i(\theta)\right)\ p(\tilde{\theta}|\theta),$$

where μ is the signal strength multiplier, and s_i and b_i are the expectations for the signal and background yield, in each bin i, respectively, and P is the Poisson probability [133, 134].

The uncertainties in the estimated background yields separated by source are used as nuisance parameters. The probability that nuisance parameters are measured as $\tilde{\theta} = (\tilde{\vartheta}_i, \tilde{\vartheta}_j, ...)$ under the condition that the true nuisance parameters are $\theta = (\vartheta_i, \vartheta_j, ...)$ is given as $p(\tilde{\theta}|\theta)$. The nuisance parameters are fully uncorrelated among each other, and either fully correlated or uncorrelated between the search bins. Each of the parameters ϑ is distributed according to a log-normal distribution to ensure positive event yields:

$$\rho(\tilde{\vartheta}|\vartheta) = \frac{1}{\sqrt{2\pi}\ln(\kappa)\vartheta}\ \exp\left(-\frac{1}{2}\left(\frac{\ln\left(\vartheta/\tilde{\vartheta}\right)}{\ln(\kappa)}\right)^2\right)$$

To discriminate the signal+background hypothesis against the background-only hypothesis ($\mu = 0$), the likelihood ratio

$$\tilde{q}_\mu = -2\ln\left(\frac{L(\text{data}|\mu, \hat{\theta}_\mu)}{L(\text{data}|\hat{\mu}, \hat{\theta})}\right)$$

is defined as test statistics, where $\hat{\theta}_\mu$ refers to the conditional maximum likelihood estimator of θ given μ, while $\hat{\mu}$ and $\hat{\theta}$ correspond to the global maximum of the likelihood [135].

The probability to obtain a value of $\tilde{q}_\mu$ larger than the observed test statistics is given as

$$\mathrm{CL_{s+b}}(\mu) = p(\tilde{q}_\mu \geq \tilde{q}_\mu^{\text{obs}}|\text{signal+background})$$
$$\mathrm{CL_b}(\mu) = p(\tilde{q}_\mu \geq \tilde{q}_\mu^{\text{obs}}|\text{background})$$

where the Asimov approximation is used to build the probability density functions [119].

A signal strength is excluded at a certain confidence level (CL) α if

$$\mathrm{CL_s}(\mu) = \frac{\mathrm{CL_{s+b}}(\mu)}{\mathrm{CL_b}(\mu)} \leq 1 - \alpha.$$

As common in high energy physics, a confidence level of 95% is used. The signal strength $\mu^{95\%\mathrm{CL}}$ for which a signal is barely excluded is defined by $\mathrm{CL_s}(\mu^{95\%\mathrm{CL}}) = 5\%$.

Expected limits and their uncertainties are constructed by generating pseudo-data according to the background-only hypothesis, and calculating for each of the pseudo-data yields $\mu^{95\%\mathrm{CL}}$. To speed up the computation, the distribution of the test statistics is only calculated once, as it is independent of the pseudo-data for a given μ. From the median and the width of the distribution of $\mu^{95\%\mathrm{CL}}$, the expected limits and their uncertainties can be estimated. Uncertainties in the signal cross section and therefore the signal strength μ are propagated to the observed exclusion.

To quantify an excess or deficit of observed events, the probability P_{bkg} for the background to fluctuate and give an event yield as large as the observed one is used. The distribution of the test statistics $\tilde{q}_0$ can be approximated by a χ^2 distribution for one degree of freedom, if no signal is assumed to be present [136]. Using this χ^2 distribution, P_{bkg} can be calculated as

$$P_{\text{bkg}} = \frac{1}{2}\left[1 - \mathrm{erf}\left(\sqrt{\tilde{q}_0^{\text{obs}}}\right)\right].$$

The significance Z can be calculated by

$$P_{\text{bkg}} = \frac{1}{\sqrt{2\pi}}\int_Z^\infty \exp\left(-\frac{x^2}{2}\right)\mathrm{d}x$$

and is defined positive for excesses and negative for deficits.

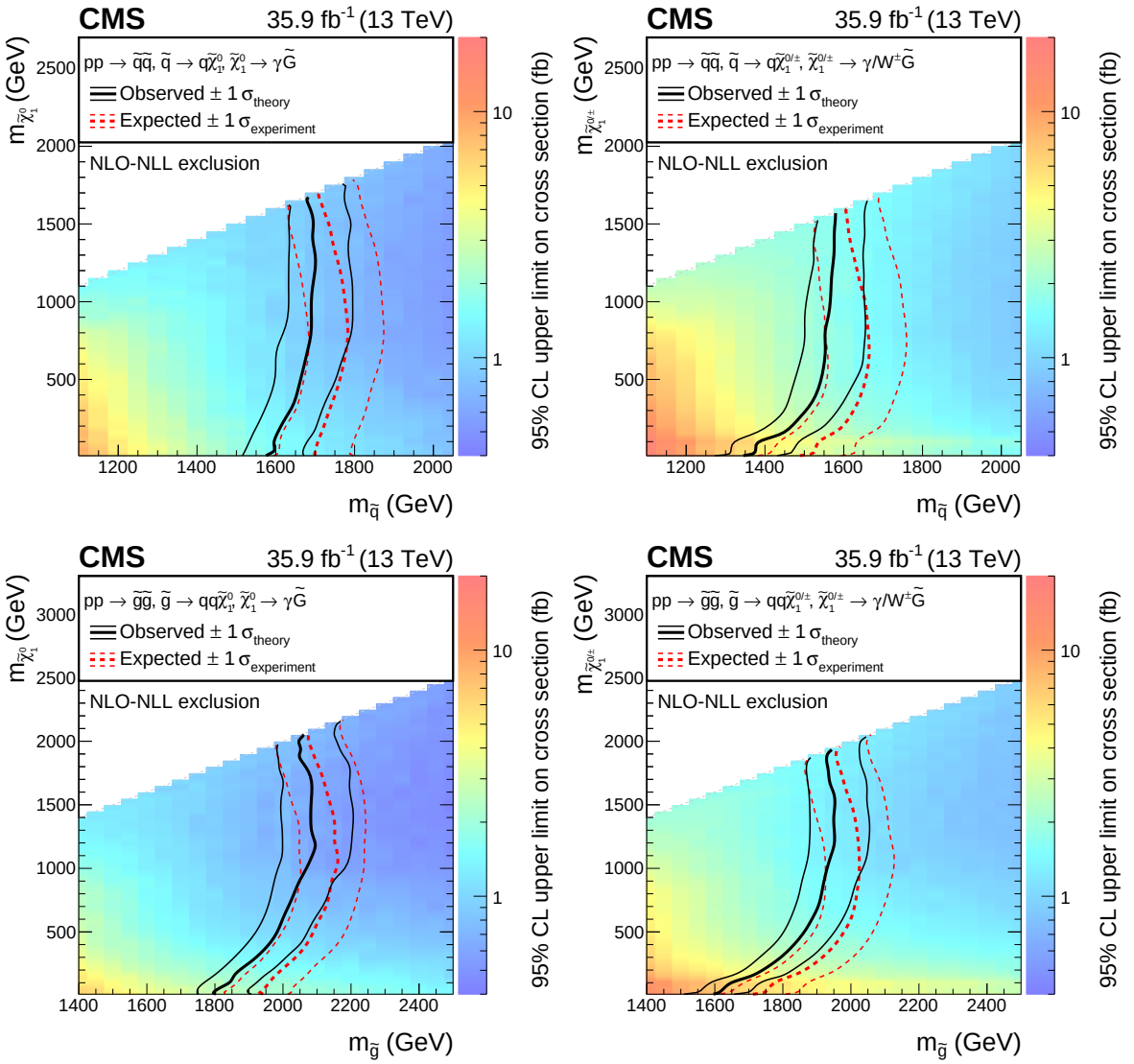

Figure 6.7: Exclusion limits at 95% CL for the squark-diphoton (top left), squark-single-photon (top right), gluino-diphoton (bottom left), and gluino-single-photon (bottom right) models. The solid black curve represents the observed exclusion contour and the uncertainty in the signal cross section. The red dashed curves represent the expected exclusion contours and the experimental uncertainties [1].

6.4 Signal model exclusion

In figure 6.7, the 95% CL SUSY cross section upper limit (SUSY cross section times $\mu^{95\%\mathrm{CL}}$) is shown as a function of the squark/gluino mass versus the gaugino mass. The observed limit and the theoretical uncertainties in the SUSY cross section are represented by black solid lines, while the expected limit and the experimental uncertainties are represented as red dashed lines. Delaunay interpolation [137] and Gaussian interpolation are used to form the exclusion contours.

The limits on gluinos are more stringent than the limits on the squarks due to the higher cross section of gluinos, as shown in figure 6.4. The limits on the diphoton models are more stringent than the limits for the single-photon models, due to the increased number of photons

in the diphoton models. The sensitivity decreases with small gaugino masses, as the photon p_T and the gravitino p_T (and therefore p_T^{miss}) is lower. At $m_{\tilde{\chi}_1^{\pm}} = m_W$, most of the energy of the chargino is transfered to the W boson, leading to events with very small p_T^{miss} and therefore low sensitivity. The observed limit is worse than the expected limit by about $1\sigma_{experiment}$, which is due to the slight excess of events with $450 < p_T^{miss} < 600$ GeV. In compressed signal scenarios, the observed and expected contours match better, due to the agreement of data and prediction in the $p_T^{miss} > 600$ GeV search regions. For the squark-diphoton model, squark masses of 1500 (1650) GeV can be excluded for low (high) gaugino masses, while for the squark-single-photon model, squark masses of 1300 (1550) GeV can be excluded for low (high) gaugino masses. For the gluino-diphoton model, gluino masses of 1750 (2000) GeV can be excluded for low (high) gaugino masses, while for the gluino-single-photon model, gluino masses of 1500 (1900) GeV can be excluded for low (high) gaugino masses.

Figure 6.8 shows the expected and observed limit contours for the gluino-single photon model for each of the six search regions independently and for the combination of the six search regions. The search region with the largest values of p_T^{miss} and H_T^{γ} dominates the limits in most of the signal scenarios. The search regions with high H_T^{γ} values and medium p_T^{miss} contribute strongly to models with large squark/gluino masses and small gaugino masses. A sizable contribution to the exclusion limits originates from the search region with low H_T^{γ} and large p_T^{miss} values. Without the division of the search region in H_T^{γ}, the limits would be less stringent, especially at low gaugino masses.

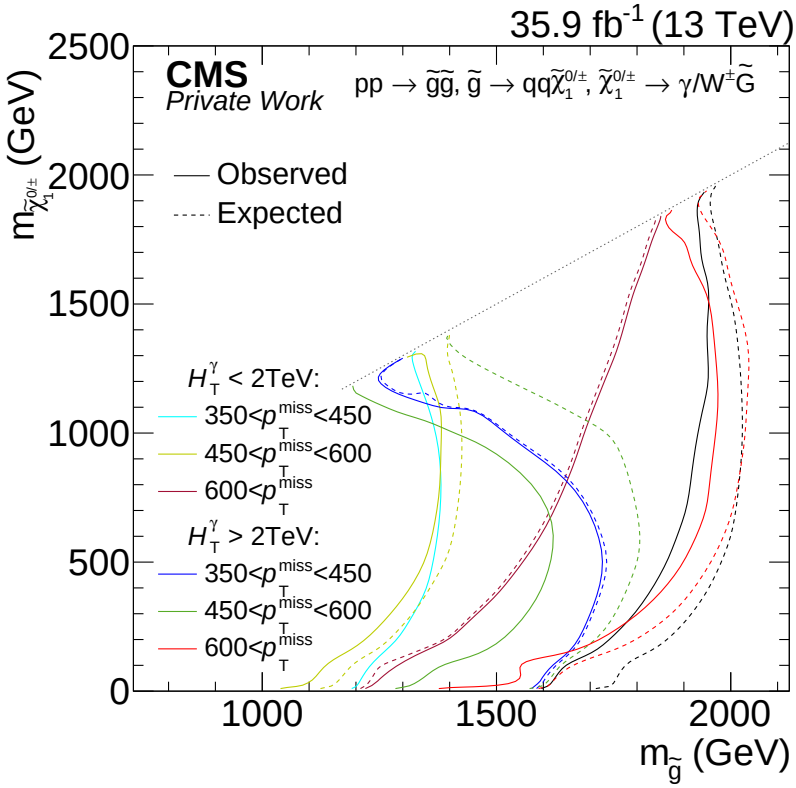

Figure 6.8: Observed and expected limit contours calculated for the six search regions independently for the gluino-single-photon model. The black lines show the combination of all search regions, and is the same as the limit contour in figure 6.7 bottom right. The p_T^{miss} interval boundaries are given in GeV.

As in figure 6.7, the expected limits are calculated taking into account the best fit of the nuisance parameter to the data, and therefore the expected limits depend slightly on the observed

data. The best fit of the nuisance parameters are different if considering the combination of the search regions or one individual search region. This can lead to a less stringent limit of the combination compared to the limit of the most significant bin, as for example at a gluino mass of about 2000 GeV and a gaugino mass of about 1300 GeV.

In figure 6.9, the significances are given for each signal scenario. Due to the slight excess of events, the significance is positive for all scenarios. For compressed scenarios, the significance is about 0.3, since this region is dominated by the highest-$p_{\mathrm{T}}^{\mathrm{miss}}$ search region, in which good agreement with the SM background is observed. For scenarios with light gauginos, the significance increases to about 2.1 due to the excesses in two of the search regions.

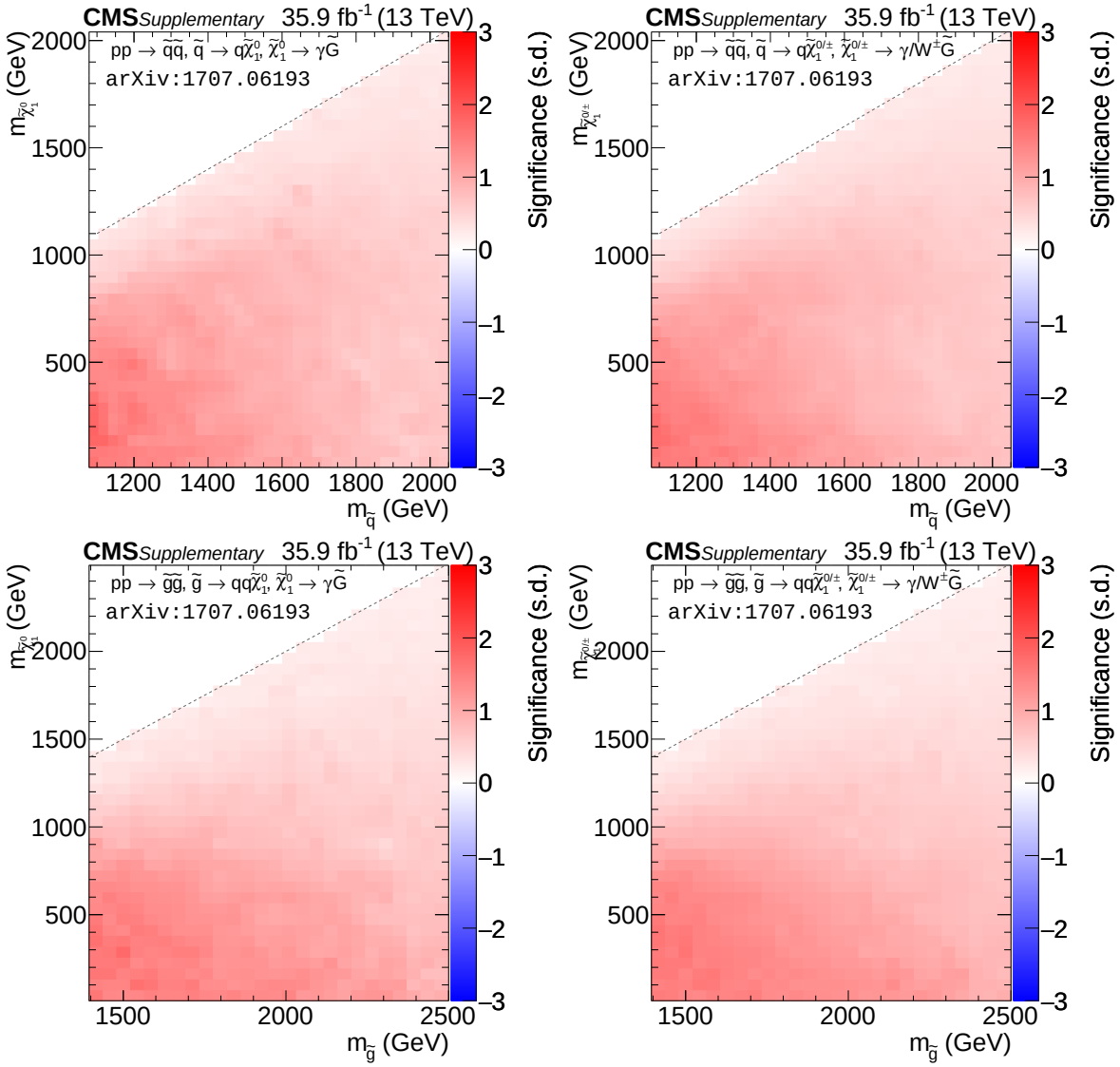

Figure 6.9: Observed significance in standard deviations for squark-diphoton (top left), squark-single-photon (top right), gluino-diphoton (bottom left), and gluino-single-photon (bottom right) models [1].

7 Comparison to other CMS analyses

In this chapter, the results and background estimation methods are compared to several other analyses performed by the CMS collaboration.

7.1 Electroweak analysis

The analysis presented in this thesis was developed in parallel to an analysis concentrating on signal scenarios induced by the electroweak force and is called electroweak analysis [60] throughout this thesis. This electroweak analysis requires at least one photon with larger p_{T}, and focus on electroweak final states with larger $p_{\mathrm{T}}^{\mathrm{miss}}$ values, but no jet or H_{T}^{γ} requirement. The background is estimated using simulation, which is scaled in a control region to the data yield.

In figure 7.1, the exclusion contours of this thesis are compared to exclusion contours of the electroweak analysis. The signal models with large gaugino masses have hardly any jets, leading to similar final states as electroweak processes. Therefore, the electroweak analysis has better limits at high gaugino masses.

The analysis discussed in this thesis was optimized for low gaugino masses in jet dominated events with little activity from photons. With the strategy described in this thesis, it is possible to exclude a wide range of models, especially for scenarios with small gaugino masses. Large gaugino masses result in large values of $p_{\mathrm{T}}^{\mathrm{miss}}$ and large photon p_{T}, allowing a better discrimination between signal and SM. Therefore, also this analysis is sensitive to scenarios with large gaugino masses.

7.2 Predecessor analysis

A similar search for SUSY with the CMS detector at $\sqrt{s} = 8\,\mathrm{TeV}$ was carried out by the author before this analysis (called 8 TeV analysis) [59, 138]. It used a data set recorded with the CMS detector during the year 2012, which corresponds to an integrated luminosity of $19.7\,\mathrm{fb}^{-1}$.

Several improvements are made, apart from the larger data set at a higher center-of-mass energy: In the 8 TeV analysis, at least two jets with $p_{\mathrm{T}} > 30\,\mathrm{GeV}$ were required, decreasing the sensitivity for compressed signal scenarios. In the 13 TeV analysis, low- and high-H_{T}^{γ} search regions are defined, also using events with less than two jets. Compressed signal scenarios result in events with high-energy photons. As the transverse momentum of the photon is included in H_{T}^{γ}, this variable does not reject such events. The additional subdivision in H_{T}^{γ} also increases the sensitivity significantly.

The most important update is the estimation of the nongenuine $p_{\mathrm{T}}^{\mathrm{miss}}$ background. For both this analysis and the 8 TeV analysis, this background was estimated by normalizing the $p_{\mathrm{T}}^{\mathrm{miss}}$ distribution of a data CR in low $p_{\mathrm{T}}^{\mathrm{miss}}$ to the photon CR. In the 8 TeV analysis, the jet CR was defined by replacing the photon by a photon candidate with increased isolation energies. Such photon candidates with increased isolation energies origin mostly from jets with few charged

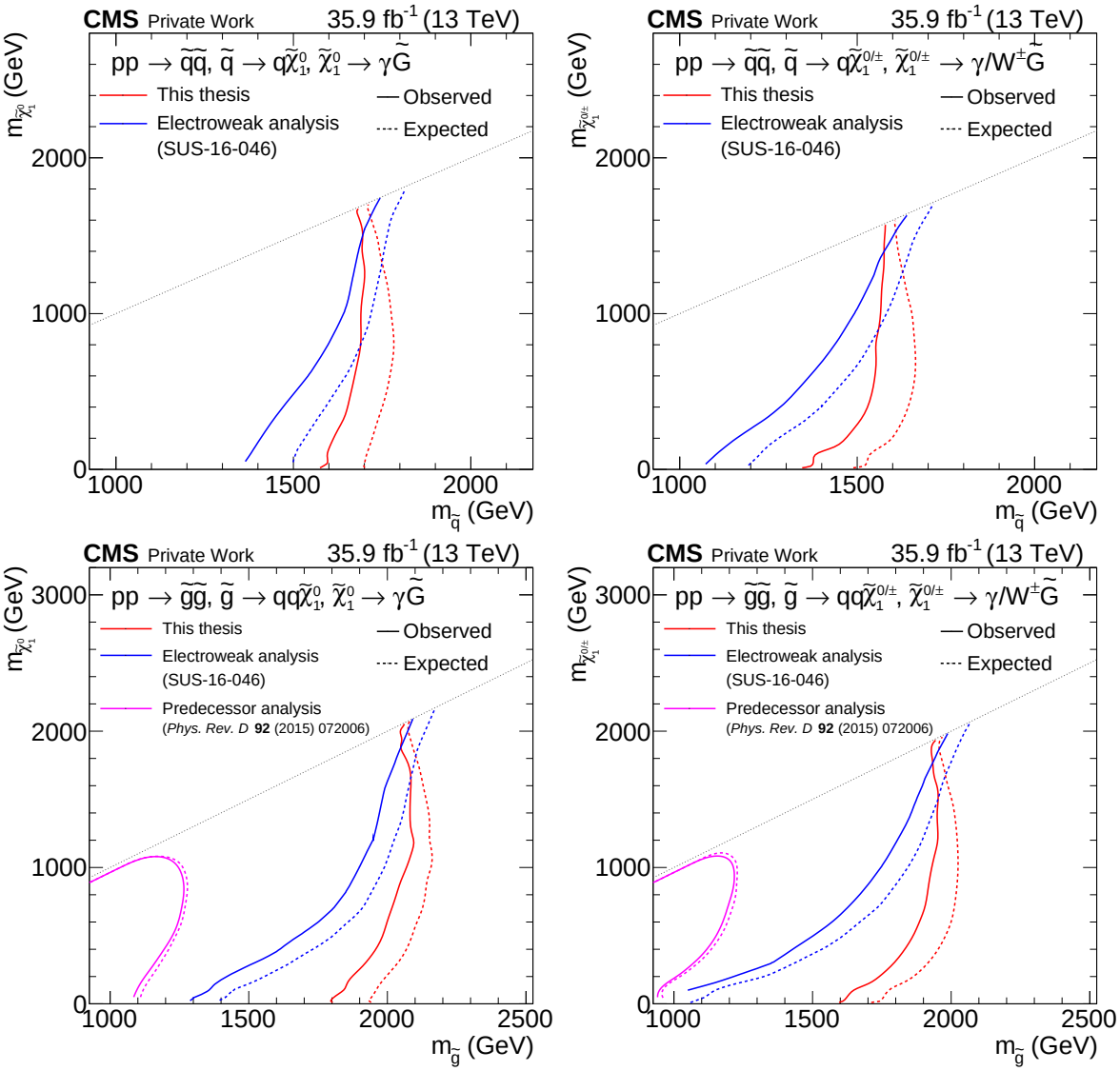

Figure 7.1: Comparison of the observed (solid) and expected (dashed) exclusion contours at 95% CL for the squark-diphoton (top left), squark-single-photon (top right), gluino-diphoton (bottom left), and gluino-single-photon (bottom right) models for different analyses [1, 59, 60].

particles, or high energetic neutral pions. The selections on the isolation requirements had to be tuned: Too strict requirements on the isolation values would result in a high contamination of events with real photons to the CR and therefore a high signal contamination. Too loose requirements on the isolation values would result in too large differences between the $p_{\mathrm{T}}^{\mathrm{miss}}$ distributions of the signal selection (with at least one photon) and the CR. To decrease the correlations between isolation energies and $p_{\mathrm{T}}^{\mathrm{miss}}$, the method was performed in bins of additional variables, leading to large statistical uncertainties. Due to the selection of the jet CR, the signal contamination of the analysis was about 20%, while it is negligible now.

For the 8 TeV analysis, the jet CR is defined by requiring at least one photon candidate with increased isolation energies. For this analysis, the jet CR is defined by requiring no photon, and is therefore more inclusive than the definition of the 8 TeV analysis. The statistical uncertainty of the background yields achieved this analysis is therefore smaller than the one of the 8 TeV analysis.

As shown in figures 4.7 and 4.8, the simulation of photons agrees well with the measured photons in data. The agreement between simulation and data is not as good for larger isolation values, and for jets being reconstructed as photon candidate with increased isolation energies. In the 8 TeV analysis, the background estimation method was also validated using simulated events, similar to the validation shown in figure 5.10. However, since the description of photon candidates with large isolation values is not as good simulated as real photons with low isolation values, it is not ensured that the background estimation method tested on simulation also performs well on data. The background estimation method used in this thesis does not rely on photon candidates with large isolation values, and so the positive validation on simulation increases our trust that the background estimation method is also working on data.

In addition to the more stable method in terms of simulation, the new background estimation methods are tested in a validation region with photons in the endcaps. Although not directly influencing the results, this additional validation ensures the performance of the background estimation methods in data.

The exclusion contours of the 8 TeV analysis and this analysis are shown in figure 7.1 for the gluino models. This analysis increases the excluded gluino mass range by about 700 GeV. The results of the 8 TeV analysis were not interpreted in squark models, so no comparison can be made for the quark models.

7.3 Other analyses performed by CMS

While this analysis is the first published search for SUSY in final states with photons analyzing all the data taken in 2016, there are other analyses developed by CMS at the time of this thesis.

The diphoton analysis selects events with two photons and high $p_{\mathrm{T}}^{\mathrm{miss}}$, and is therefore sensitive to scenarios in which the neutralinos have a large decay probability to photons. However, if one of the two photons from the SUSY process is not reconstructed or identified, the event is not selected, but may still be selected by this analysis. Predecessor analyses of this analysis and the diphoton analysis showed a similar sensitivity for SUSY models with two photons in the final state [139].

In the lepton+photon analysis events with at least one photon and at least one electron or muon is selected. It is sensitive to scenarios like the gluino-single photon model. However, the branching fraction BF($W \to e\nu/\mu\nu$) is only about 20%, reducing the maximal possible signal acceptance, while this analyses includes all decay possibilities of the W boson. Due to the low number of expected events in the lepton+photon analysis, a restriction on high H_{T}^{γ} values would dramatically increase the statistical uncertainty, and therefore the analysis discussed in this thesis has a better sensitivity for large gluino or squark masses.

As it is not known exactly in which final states BSM physics would result, it is important to search for hints as generically as possible. The selection of this search is defined more inclusively than others, while still resulting in stringent exclusion limits.

7.4 Ideas for the development of this analysis

In the low-H_{T}^{γ} region in this analysis and the search regions of the electroweak analysis, the contribution of the nongenuine $p_{\mathrm{T}}^{\mathrm{miss}}$ background is small compared to the contribution of backgrounds estimated from simulation. In the high-H_{T}^{γ} region, the relative contribution of the nongenuine $p_{\mathrm{T}}^{\mathrm{miss}}$ background is larger than in the low-H_{T}^{γ} region. An update of this

analysis should therefore focus on a better description or reduction of the SM background from nongenuine $p_{\mathrm{T}}^{\mathrm{miss}}$.

To reduce the nongenuine $p_{\mathrm{T}}^{\mathrm{miss}}$ background, restrictions on the angle between the $\vec{p}_{\mathrm{T}}^{\mathrm{miss}}$ and the $\vec{p}_{\mathrm{T}}$ of jets can be made. This reduced the number of events in which $p_{\mathrm{T}}^{\mathrm{miss}}$ is caused by the mismeasurement of the p_{T} of one of the jets.

To reduce the uncertainty in the event yields of the nongenuine $p_{\mathrm{T}}^{\mathrm{miss}}$ background, the number of events in the jet control region can be increased by using a unprescaled trigger for the high-H_{T}^{γ} region. In this analysis, events selected for the jet control region must fulfill $H_{\mathrm{T}}^{\gamma} > 600\,\mathrm{GeV}$ in the online trigger system, but due to the band width restriction on the HLT, only a fraction of these events are saved. There are less events with $H_{\mathrm{T}}^{\gamma} > 900\,\mathrm{GeV}$, such that every event with this requirement can be saved by the HLT system. As the jet control region requires $H_{\mathrm{T}}^{\gamma} > 2000\,\mathrm{GeV}$, for the high-$H_{\mathrm{T}}^{\gamma}$ region, a H_{T}^{γ} trigger with a higher H_{T}^{γ} threshold can be used. Using this $H_{\mathrm{T}}^{\gamma} > 900\,\mathrm{GeV}$ trigger has also the advantage to consider SUSY final states with low photon p_{T}. In this analysis, requirements on the photon p_{T} are made to ensure a high trigger efficiency of the photon-H_{T}^{γ} trigger, which is used in this analysis to select possible signal events. Reducing the minimal photon p_{T} would increase the sensitivity to SUSY scenarios with small gaugino masses.

In the electroweak analysis, the shapes of the γZ, γW, and $\gamma t\bar{t}$ backgrounds are estimated from simulation, while the normalization of these backgrounds is estimated from data control regions, yielding in a smaller relative uncertainty compared to this analysis. If suitable data control regions can be found for this analysis, this method could be used in this analysis as well.

To enhance the discrimination between signal and SM events, the H_{T}^{γ} criterion could also be replaced by a selection on more sophisticated variables, like the razor variables [115, 116] or the α_{T} variable [118]. To compute these variables, the jets and the photons are reclustered to form exactly two "mega-jets". The razor variables and α_{T} variable is then computed using the $\vec{p}_{\mathrm{T}}$ of the mega-jets and the $\vec{p}_{\mathrm{T}}^{\mathrm{miss}}$ like shown in the respective references [115, 116, 118], and yield a good discrimination power between signal and SM events in the corresponding search regions. Requirements on these variables can also increase the discrimination of signal and SM events in an update of this analysis.

The event selection in this thesis is defined inclusively to select several different signal scenarios. To increase the sensitivity to more special signal scenarios, the search region can be divided differently than done in this analysis. For example, by dividing the search regions with respect to the multiplicity of b-tagged jets, the sensitivity to models of bottom or top squark pair production or to models with higgsinos can be increased. Higgsinos decay usually into H bosons, which can then decay into two b-quarks, yielding final states with at least two b-jets.

In this thesis, events recorded in 2016 are studied, corresponding to an integrated luminosity of $35.9\,\mathrm{fb}^{-1}$. The data recorded in 2017 corresponds to an integrated luminosity of $47.4\,\mathrm{fb}^{-1}$, and in 2018 a similar integrated luminosity is expected. No collision data is planned in 2019 and 2020. Using more data, the statistical uncertainty can be reduced, and thus increasing the sensitivity to models not excluded in this thesis, even if the methods described in this thesis are unaltered.

8 Summary

In this thesis, a search for Supersymmetry (SUSY) in events with at least one photon, large transverse event activity, and large missing transverse momentum was presented. The data of proton-proton collisions, corresponding to an integrated luminosity of $35.9\,\mathrm{fb}^{-1}$, were recorded by the CMS detector in the year 2016 at a center-of-mass energy of 13 TeV. The results of this thesis are published by the Journal of High Energy Physics [1].

In gauge mediated SUSY breaking models, neutralinos can decay to a photon and a gravitino. If R-parity is assumed, the gravitino is stable and leaves the detector undetected, leading to events with large missing transverse momentum. Large transverse event activity, the sum of the transverse momenta of the jets and the leading photon, can be caused by heavy primary produced SUSY particles. No assumptions on the presence of a second photon, a lepton, or the multiplicity of jets is made, resulting in an analysis sensitive to various possible models of physics beyond the standard model (SM).

The background yield of SM events is estimated using data control regions and simulated events. Events with nongenuine $p_{\mathrm{T}}^{\mathrm{miss}}$ (mostly γ+jet and multijet events) are estimated using a data control region dominated by multijet events. The $p_{\mathrm{T}}^{\mathrm{miss}}$ distribution is modified and normalized for low values of $p_{\mathrm{T}}^{\mathrm{miss}}$ and is used as prediction for events with large $p_{\mathrm{T}}^{\mathrm{miss}}$ and photons.

The contribution of events with electrons misreconstructed as photons is estimated using a control region with an electron instead of the photon. This control region is then scaled by a photon-to-electron scale factor, which is estimated in $Z \to ee$ events.

Contributions from γW, γZ, and $\gamma t\bar{t}$ are estimated using generated events with next-to-leading order cross sections. The response of the detector is simulated, and the events are reconstructed and selected using the same methods as used for data events.

To validate the background estimation methods, they are applied to signal-depleted data selections. In these selections, the observed data agree with the SM expectation.

The data are compared to the SM expectation in six disjunct search regions. No significant excess of events above the SM background is observed. The most sensitive search region is dominated by γW events and events with nongenuine $p_{\mathrm{T}}^{\mathrm{miss}}$.

The results are interpreted in simplified models motivated by gauge mediated SUSY breaking models. Squark- and gluino pair production models are studied, in which neutralinos are produced in the decay chains. The neutralinos decay into a photon and a gravitino, resulting in final states with jets, photons, and missing transverse momentum. Squark masses up to 1.3–1.6 TeV and gluino masses up to 1.5–1.95 TeV can be excluded, depending on the gaugino masses and the branching fractions of the squarks and the gluinos.

Compared to the last publication of this analysis at a center-of-mass energy of 8 TeV [59], the excluded gluino mass range is increased by 700 GeV. At the time of writing, the exclusion for the models under consideration in this thesis are the most stringent ones for scenarios with low neutralino masses.

The amount of data analysed in this thesis corresponds to the data presented in the publication. Meanwhile, the CMS experiment is still recording data at the time of writing. Repeating this

analysis using more data can therefore increase the sensitivity to models with larger SUSY particle masses or smaller cross sections.

A Appendix

A.1 Data sets

Recorded events are processed and saved in several data sets, depending on the decision of the HLT. The *SinglePhoton* data set is used for events with photons and events with photons and H_{T}^{γ} (search region trigger), while the *JetHT* data set contains events triggered by high values of H_{T}^{γ}. The *SingleElectron* data set is used to estimated $R_{\gamma/e}$. The run ranges are shown in table A.1. The name of the trigger paths are given in table A.2.

The generated MC data sets, with their cross sections and their simulated integrated luminosities are displayed in table A.3. The $\gamma t\bar{t}$ sample is generated in NLO, and the NLO cross section is used. All other SM samples are generated at LO accuracy. If the samples are used for comparison to data, the cross section is multiplied by the k-factor, which is the ratio of NLO to LO cross section. For $t\bar{t}$, it is defined as the ratio between NNLO and LO cross section.

Table A.1: Run areas and luminosities for the data used in this analysis

Name	integrated luminosity (fb^{-1})
Run2016B-23Sep2016-v3	5.9
Run2016C-23Sep2016-v1	2.6
Run2016D-23Sep2016-v1	4.2
Run2016E-23Sep2016-v1	4.0
Run2016F-23Sep2016-v1	3.1
Run2016G-23Sep2016-v1	7.5
Run2016H-PromptReco-v2	8.4
Run2016H-PromptReco-v3	0.3

Table A.2: CMS internal names of the trigger paths

Name	Trigger path
Photon-H_{T}^{γ} trigger	HLT_Photon90_CaloIdL_PFHT600_v*
Photon trigger	HLT_Photon90_v*
H_{T}^{γ} trigger	HLT_PFHT600_v*
Electron trigger	HLT_Ele27_eta2p1_WPTight_Gsf_v*

Table A.3: Cross sections as used in the analysis, k-factors, and integrated luminosities for various processes. The k-factor is the factor by which the LO cross section is multiplied to obtain NLO accuracy for the cross section. For $t\bar{t}$, the NNLO cross section is used. The γW and γZ samples are binned in photon p_{T}.

Process	Selection (GeV)	(k $\cdot$) σ (pb)	k-factor	int. lumi. (fb^{-1})
γ+jet	$40 < H_{\mathrm{T}}^{\mathrm{gen}} < 100$	17 000	-	0.66
	$100 < H_{\mathrm{T}}^{\mathrm{gen}} < 200$	5 400	-	2.7
	$200 < H_{\mathrm{T}}^{\mathrm{gen}} < 400$	1 200	-	42
	$400 < H_{\mathrm{T}}^{\mathrm{gen}} < 600$	130	-	88
	$600 < H_{\mathrm{T}}^{\mathrm{gen}}$	44	-	260
Multijet	$500 < H_{\mathrm{T}}^{\mathrm{gen}} < 700$	32 000	-	1.9
	$700 < H_{\mathrm{T}}^{\mathrm{gen}} < 1000$	6 800	-	6.7
	$1000 < H_{\mathrm{T}}^{\mathrm{gen}} < 1500$	1 200	-	13
	$1500 < H_{\mathrm{T}}^{\mathrm{gen}} < 2000$	120	-	99
	$2000 < H_{\mathrm{T}}^{\mathrm{gen}}$	25	-	240
$t\bar{t}$		832	1.63	18
	$600 < H_{\mathrm{T}}^{\mathrm{gen}} < 800$	2.6	1.63	5 400
	$800 < H_{\mathrm{T}}^{\mathrm{gen}} < 1200$	1.1	1.63	9 600
	$1200 < H_{\mathrm{T}}^{\mathrm{gen}} < 2500$	0.20	1.63	15 000
	$2500 < H_{\mathrm{T}}^{\mathrm{gen}}$	0.0020	1.63	650 000
$\gamma t\bar{t}$ (NLO)		3.7	-	870
$W \to \ell\nu$	$200 < H_{\mathrm{T}}^{\mathrm{gen}} < 400$	440	1.21	38
	$400 < H_{\mathrm{T}}^{\mathrm{gen}} < 600$	59	1.21	130
	$600 < H_{\mathrm{T}}^{\mathrm{gen}} < 800$	15	1.21	1 300
	$800 < H_{\mathrm{T}}^{\mathrm{gen}} < 1200$	6.7	1.21	1 200
	$1200 < H_{\mathrm{T}}^{\mathrm{gen}} < 2500$	1.6	1.21	870
	$2500 < H_{\mathrm{T}}^{\mathrm{gen}}$	0.039	1.21	68 000
$\gamma W \to \gamma\ell\nu$	$40 < p_{\mathrm{T}} < 130$	17	1.34	300
	$130 < p_{\mathrm{T}}$	0.88	1.34	570
$Z \to \nu\nu$	$200 < H_{\mathrm{T}}^{\mathrm{gen}} < 400$	96	1.23	250
	$400 < H_{\mathrm{T}}^{\mathrm{gen}} < 600$	13	1.23	750
	$600 < H_{\mathrm{T}}^{\mathrm{gen}} < 800$	3.1	1.23	1 800
	$800 < H_{\mathrm{T}}^{\mathrm{gen}} < 1200$	1.5	1.23	1 500
	$1200 < H_{\mathrm{T}}^{\mathrm{gen}} < 2500$	0.35	1.23	1 500
	$2500 < H_{\mathrm{T}}^{\mathrm{gen}}$	0.0085	1.23	47 000
$\gamma Z \to \gamma\nu\nu$	$40 < p_{\mathrm{T}} < 130$	3.9	1.39	1 300
	$130 < p_{\mathrm{T}}$	0.25	1.39	1 300

A.2 Trigger efficiency for jet CR

For the search regions, events are triggered based on the presence of a photon and H_{T}^{γ}, while events for the jet CR are selected by the trigger based on H_{T}^{γ} only. In section 4.4, the trigger efficiency of the photon and H_{T}^{γ} trigger was measured. To check if the H_{T}^{γ}-only trigger performs similarly, the trigger efficiency is measured in the same way as in section 4.4, using events triggered only by the presence of a photon with $p_{\mathrm{T}} > 90\,\mathrm{GeV}$. The trigger efficiency is shown in figure A.1 as a function of H_{T}^{γ} and $p_{\mathrm{T}}^{\mathrm{miss}}$. The value of the trigger efficiency includes the prescale, and is therefore not close to 100%. As expected, the trigger efficiency is not depending on $p_{\mathrm{T}}^{\mathrm{miss}}$ or H_{T}^{γ} for $H_{\mathrm{T}}^{\gamma} > 700\,\mathrm{GeV}$.

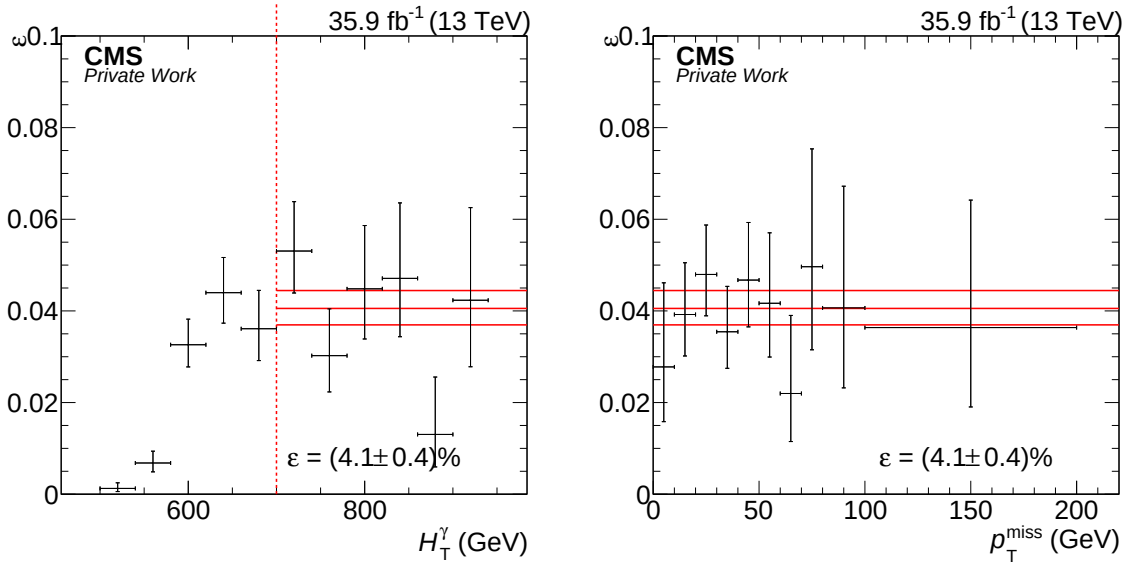

Figure A.1: Trigger efficiency for the jet CR as a function of H_{T}^{γ} (left) and $p_{\mathrm{T}}^{\mathrm{miss}}$ (right).

A.3 Scale determination for the nongenuine-$p_{\mathrm{T}}^{\mathrm{miss}}$ background estimation

Figure A.2 shows the χ^2 between the photon CR and the jet CR in $p_{\mathrm{T}}^{\mathrm{miss}} < 100\,\mathrm{GeV}$ as a function of the scale factor for the validation on simulation and the validation using the EE selection with data.

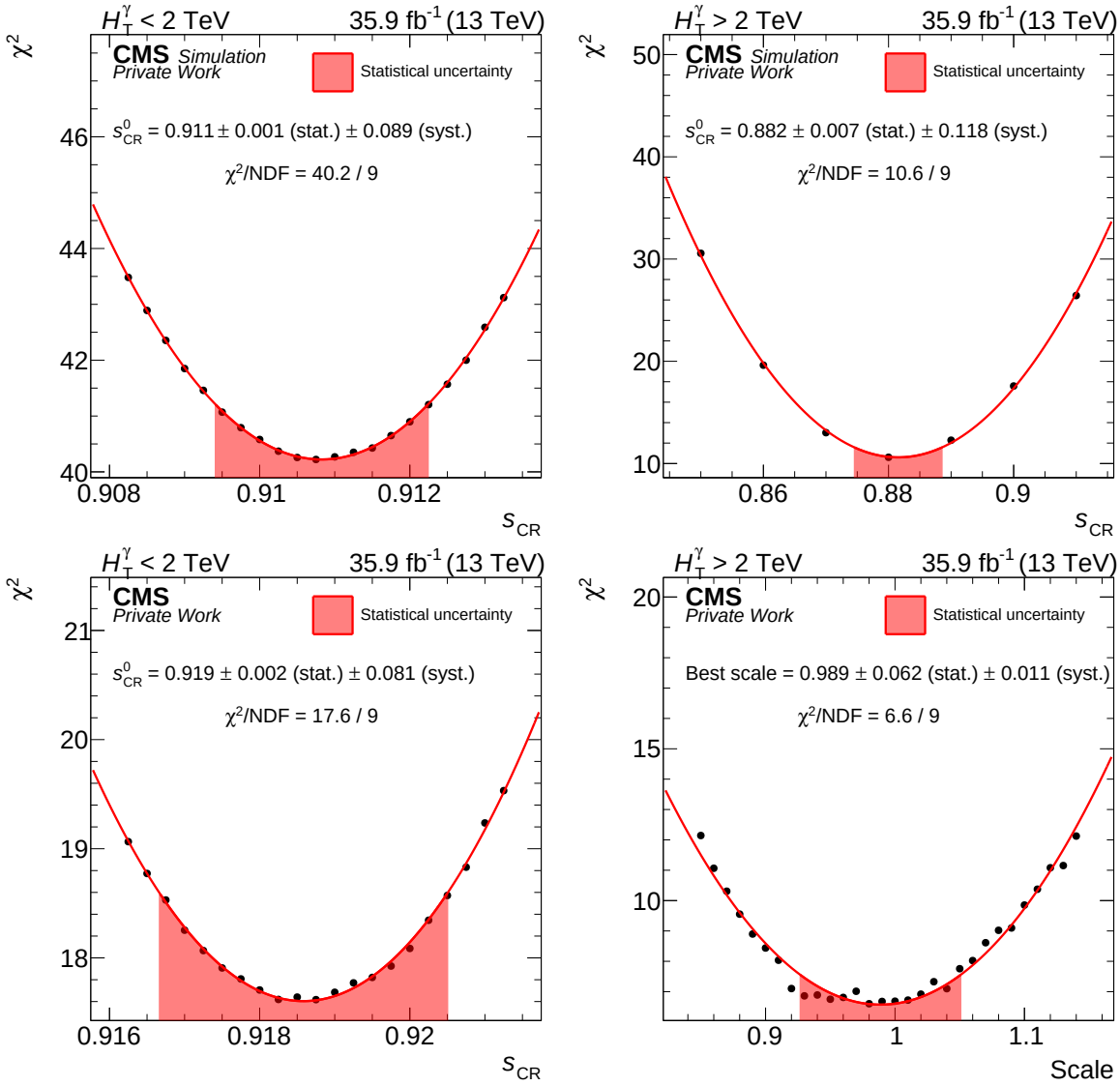

Figure A.2: The χ^2 between the photon CR and the jet CR as a function of scaling factors for the validation for low- (high-) H_T^γ CR on the left (right). The top row shows the validation on simulation, while the bottom row shows the validation in the EE selection.

A.4 Uncertainties for simulated backgrounds

The systematic uncertainties in the renormalization scale, factorization scale, PDF, pileup and the jet energy scale and resolution for simulated SM samples are estimated as discussed in section 5.4.2. Figures A.3-A.7 show the systematic uncertainties similar to figure 5.17.

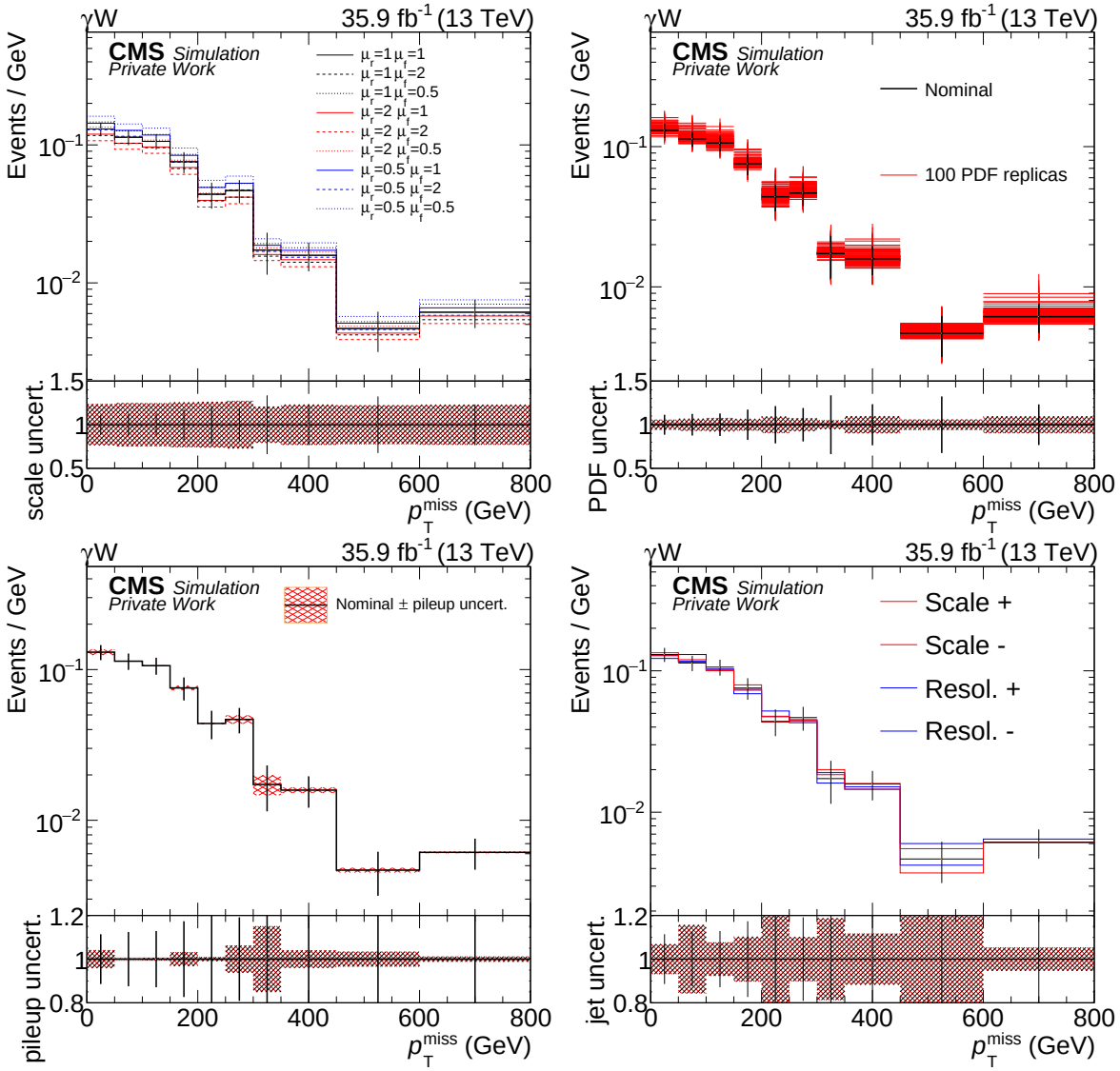

Figure A.3: Systematic uncertainties in the scale (top left), the PDF (top right), the pileup (bottom left), and the jet energy scale and resolution (bottom right) for γW simulation in the high-H_{T}^{γ} selection.

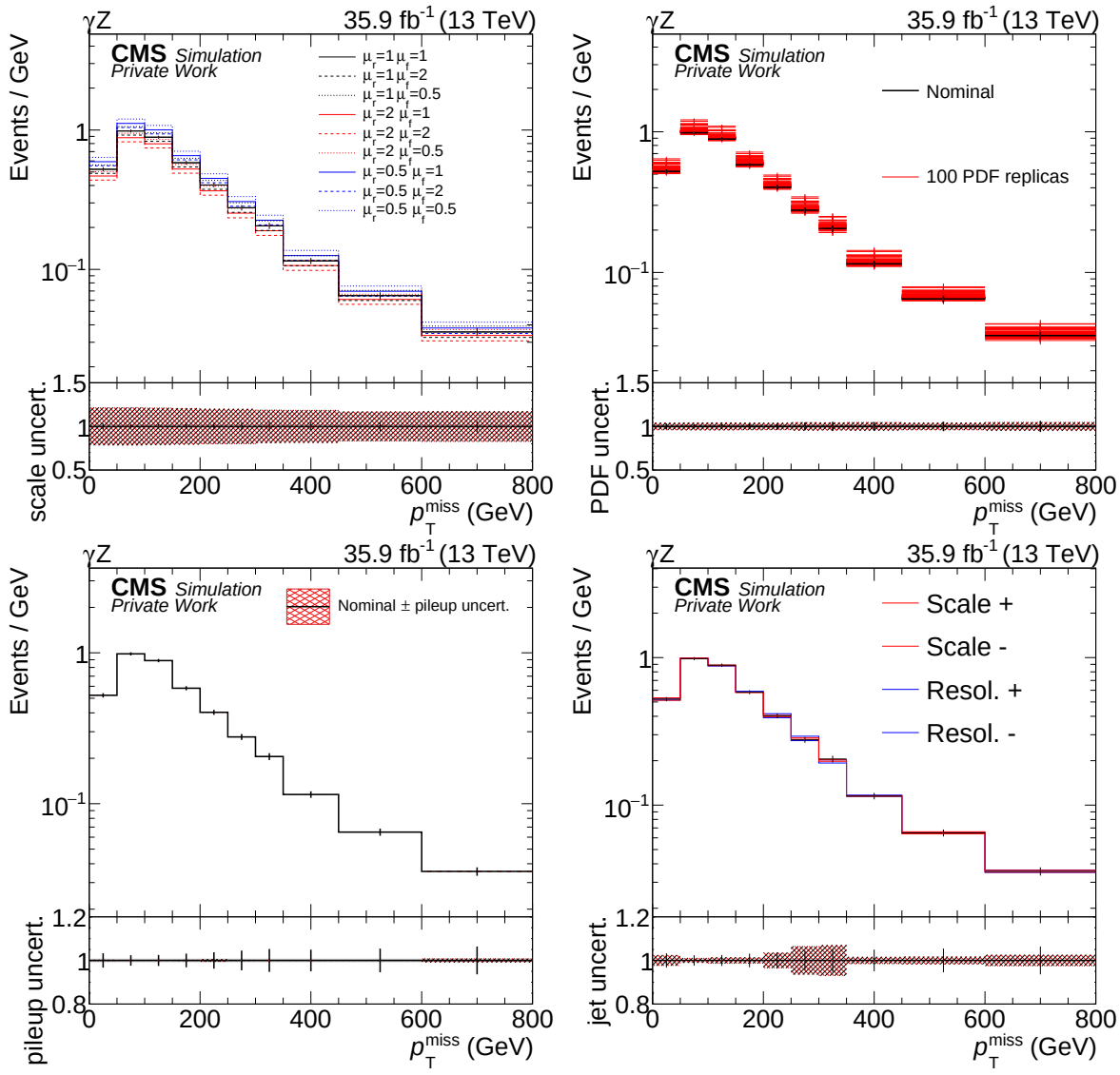

Figure A.4: Systematic uncertainties in the scale (top left), the PDF (top right), the pileup (bottom left), and the jet energy scale and resolution (bottom right) for γZ simulation in the low-H_{T}^{γ} selection.

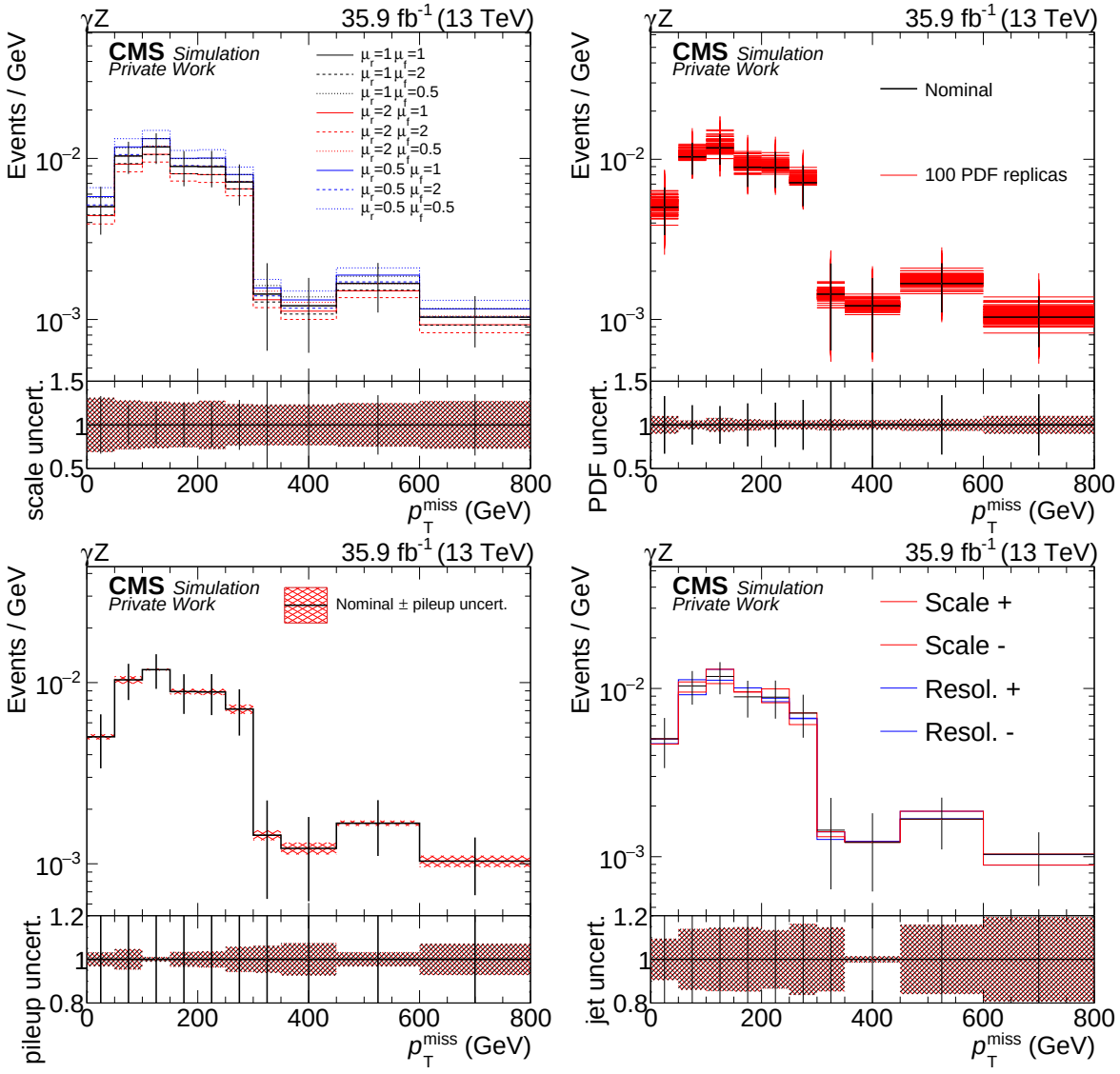

Figure A.5: Systematic uncertainties in the scale (top left), the PDF (top right), the pileup (bottom left), and the jet energy scale and resolution (bottom right) for γZ simulation in the high-H_{T}^{γ} selection.

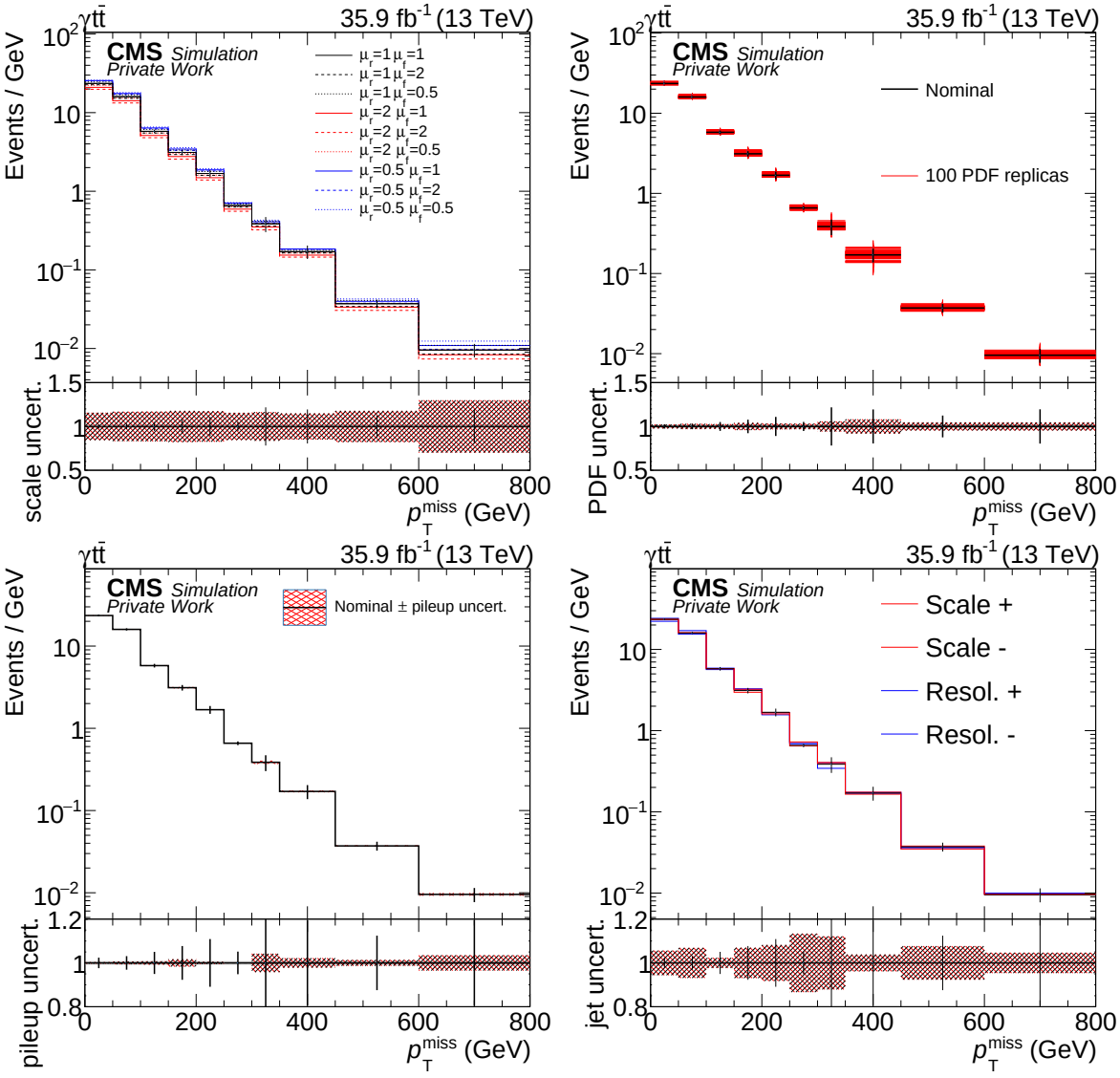

Figure A.6: Systematic uncertainties in the scale (top left), the PDF (top right), the pileup (bottom left), and the jet energy scale and resolution (bottom right) for $\gamma t\bar{t}$ simulation in the low-H_{T}^{γ} selection.

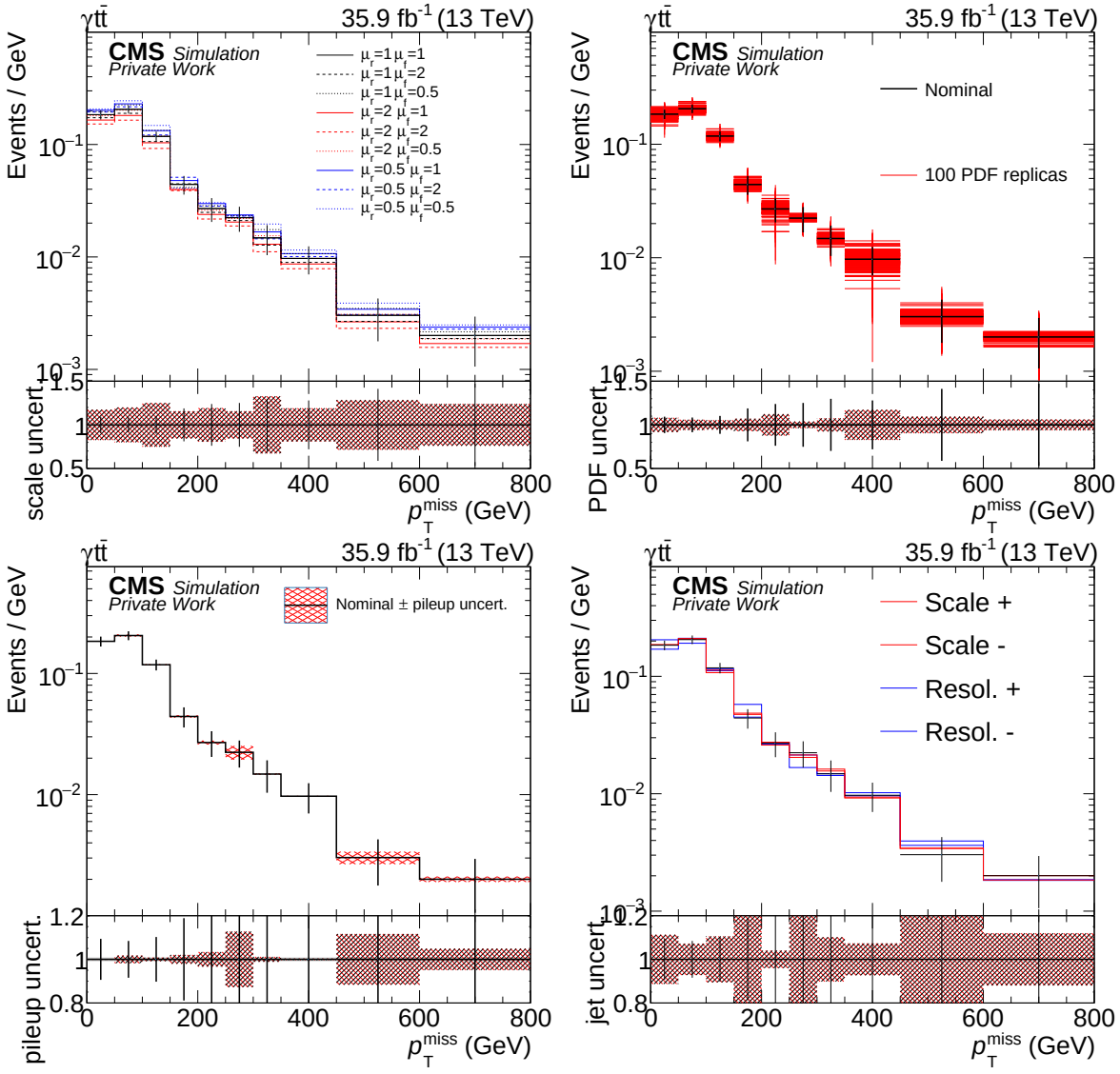

Figure A.7: Systematic uncertainties in the scale (top left), the PDF (top right), the pileup (bottom left), and the jet energy scale and resolution (bottom right) for $\gamma t\bar{t}$ simulation in the high-H_{T}^{γ} selection.

B Bibliography

[1] CMS Collaboration, "Search for supersymmetry in events with at least one photon, missing transverse momentum, and large transverse event activity in proton-proton collisions at $\sqrt{s} = 13\,\text{TeV}$", *J. High Energy Phys.* **12** (2017) 142, doi:10.1007/JHEP12(2017)142, arXiv:1707.06193.

[2] P. D. Group, "Review of Particle Physics", *Chin. Phys. C* **40** (2016) 100001, doi:10.1088/1674-1137/40/10/100001.

[3] P. W. Anderson, "Plasmons, gauge invariance, and mass", *Phys. Rev.* **130** (1963) 439, doi:10.1103/PhysRev.130.439.

[4] F. Englert and R. Brout, "Broken symmetry and the mass of gauge vector mesons", *Phys. Rev. Lett.* **13** (1964) 321, doi:10.1103/PhysRevLett.13.321.

[5] G. S. Guralnik, C. R. Hagen, and T. W. B. Kibble, "Global conservation laws and massless particles", *Phys. Rev. Lett.* **13** (1964) 585, doi:10.1103/PhysRevLett.13.585.

[6] P. W. Higgs, "Broken symmetries and the masses of gauge bosons", *Phys. Rev. Lett.* **13** (1964) 508, doi:10.1103/PhysRevLett.13.508.

[7] ATLAS Collaboration, "Observation of a new particle in the search for the Standard Model Higgs boson with the ATLAS detector at the LHC", *Phys. Lett. B* **716** (2012) 1, doi:10.1016/j.physletb.2012.08.020.

[8] CMS Collaboration, "Observation of a new boson at a mass of 125 GeV with the CMS experiment at the LHC", *J. High Energy Phys.* **06** (2013) 081, doi:10.1007/JHEP06(2013)081.

[9] P. J. Mohr, D. B. Newell, and B. N. Taylor, "CODATA recommended values of the fundamental physical constants: 2014", *Rev. Mod. Phys.* **88** (2016) 035009, doi:10.1103/RevModPhys.88.035009, arXiv:1507.07956.

[10] CMS Collaboration, "Measurement of the top quark mass using proton-proton data at $\sqrt{s} = 7$ and $8\,\text{TeV}$", *Phys. Rev. D* **93** (2016) 072004, doi:10.1103/PhysRevD.93.072004.

[11] B. T. Cleveland et al., "Measurement of the solar electron neutrino flux with the Homestake chlorine detector", *Astrophys. J.* **496** (1998) 505, doi:10.1086/305343.

[12] M. Hirsch and J. W. F. Valle, "Supersymmetric origin of neutrino mass", *New J. Phys.* **6** (2004) 76, doi:10.1088/1367-2630/6/1/076, arXiv:hep-ph/0405015.

[13] L. Canetti, M. Drewes, and M. Shaposhnikov, "Matter and antimatter in the universe", *New J. Phys.* **14** (2012) 095012, doi:10.1088/1367-2630/14/9/095012, arXiv:1204.4186.

[14] J. H. Christenson, J. W. Cronin, V. L. Fitch, and R. Turlay, "Evidence for the 2π Decay of the K_2^0 Meson", *Phys. Rev. Lett.* **13** (1964) 138, doi:10.1103/PhysRevLett.13.138.

[15] V. C. Rubin, N. Thonnard, and W. K. Ford, Jr., "Rotational properties of 21 SC galaxies with a large range of luminosities and radii, from NGC 4605 ($R = 4\,\text{kpc}$) to UGC 2885 ($R = 122\,\text{kpc}$)", *Astrophys. J.* **238** (1980) 471, doi:10.1086/158003.

[16] A. N. Taylor et al., "Gravitational lens magnification and the mass of Abell 1689", *Astrophys. J.* **501** (1998) 539, doi:10.1086/305827, arXiv:astro-ph/9801158.

[17] Planck Collaboration, "Planck 2015 results. I. Overview of products and scientific results", *Astron. Astrophys.* **594** (2016) A1, doi:10.1051/0004-6361/201527101, arXiv:1502.01582.

[18] J. C. Maxwell, "On physical lines of force", *Philosophical Magazine* **90** (1861) 11, doi:10.1080/14786431003659180.

[19] S. L. Glashow, "Partial Symmetries of Weak Interactions", *Nucl. Phys.* **22** (1961) 579, doi:10.1016/0029-5582(61)90469-2.

[20] S. Weinberg, "A Model of Leptons", *Phys. Rev. Lett.* **19** (1967) 1264, doi:10.1103/PhysRevLett.19.1264.

[21] A. Salam, "Weak and Electromagnetic Interactions", *Conf. Proc.* **C680519** (1968) 367.

[22] S. P. Martin, "A supersymmetry primer", *Adv. Ser. Direct. High Energy Phys.* **21** (2010) 1, doi:10.1142/9789814307505_0001, arXiv:hep-ph/9709356.

[23] H. Georgi and S. L. Glashow, "Unity of all elementary particle forces", *Phys. Rev. Lett.* **32** (1974) 438, doi:10.1103/PhysRevLett.32.438.

[24] S. Carlip, "Quantum gravity: a progress report", *Rept. Prog. Phys.* **64** (2001) 885, doi:10.1088/0034-4885/64/8/301, arXiv:gr-qc/0108040.

[25] R. Barbieri and G. F. Giudice, "Upper bounds on supersymmetric particle masses", *Nucl. Phys. B* **306** (1988) 63, doi:10.1016/0550-3213(88)90171-X.

[26] ATLAS and CMS Collaborations, "Combined measurement of the Higgs boson mass in pp collisions at $\sqrt{s} = 7$ and 8 TeV with the ATLAS and CMS experiments", *Phys. Rev. Lett.* **114** (2015) 191803, doi:10.1103/PhysRevLett.114.191803.

[27] P. Ramond, "Dual theory for free fermions", *Phys. Rev. D* **3** (1971) 2415, doi:10.1103/PhysRevD.3.2415.

[28] Y. A. Gol'fand and E. P. Likhtman, "Extension of the algebra of Poincare group generators and violation of P invariance", *JETP Lett.* **13** (1971) 323, *Pisma Zh. Eksp. Teor. Fiz.* **13** (1971) 452.

[29] J. Wess and B. Zumino, "Supergauge transformations in four-dimensions", *Nucl. Phys. B* **70** (1974) 39, doi:10.1016/0550-3213(74)90355-1.

[30] S. Ferrara and B. Zumino, "Supergauge invariant Yang-Mills theories", *Nucl. Phys. B* **79** (1974) 413, doi:10.1016/0550-3213(74)90559-8.

[31] A. H. Chamseddine, R. L. Arnowitt, and P. Nath, "Locally supersymmetric grand unification", *Phys. Rev. Lett.* **49** (1982) 970, doi:10.1103/PhysRevLett.49.970.

[32] R. Barbieri, S. Ferrara, and C. A. Savoy, "Gauge models with spontaneously broken local supersymmetry", *Phys. Lett. B* **119** (1982) 343, doi:10.1016/0370-2693(82)90685-2.

[33] L. J. Hall, J. D. Lykken, and S. Weinberg, "Supergravity as the messenger of supersymmetry breaking", *Phys. Rev. D* **27** (1983) 2359, doi:10.1103/PhysRevD.27.2359.

[34] K. Inoue, A. Kakuto, H. Komatsu, and S. Takeshita, "Aspects of grand unified models with softly broken supersymmetry", *Prog. Theor. Phys.* **68** (1982) 927, doi:10.1143/PTP.68.927, [Erratum: *Prog. Theor. Phys.* **70** (1983) 330].

[35] Super-Kamiokande Collaboration, "Search for proton decay via $p \to e^+\pi^0$ and $p \to \mu^+\pi^0$ in 0.31 megaton · years exposure of the Super-Kamiokande water Cherenkov detector", *Phys. Rev. D* **95** (2017) 012004, doi:10.1103/PhysRevD.95.012004, arXiv:1610.03597.

[36] F. Staub, W. Porod, and J. Niemeyer, "Strong dark matter constraints on GMSB models", *J. High Energy Phys.* **01** (2010) 058, doi:10.1007/JHEP01(2010)058.

[37] P. Fayet, "Mixing between gravitational and weak interactions through the massive gravitino", *Phys. Lett. B* **70** (1977) 461, doi:10.1016/0370-2693(77)90414-2.

[38] H. Baer, M. Brhlik, C.-h. Chen, and X. Tata, "Signals for the minimal gauge-mediated supersymmetry breaking model at the Fermilab Tevatron collider", *Phys. Rev. D* **55** (1997) 4463, doi:10.1103/PhysRevD.55.4463, arXiv:hep-ph/9610358.

[39] H. Baer, P. G. Mercadante, X. Tata, and Y. Wang, "Reach of Fermilab Tevatron upgrades in gauge-mediated supersymmetry breaking models", *Phys. Rev. D* **60** (1999) 055001, doi:10.1103/PhysRevD.60.055001, arXiv:hep-ph/9903333.

[40] S. Dimopoulos, S. Thomas, and J. D. Wells, "Sparticle spectroscopy and electroweak symmetry breaking with gauge-mediated supersymmetry breaking", *Nucl. Phys. B* **488** (1997) 39, doi:10.1016/S0550-3213(97)00030-8, arXiv:hep-ph/9609434.

[41] J. Ellis, J. L. Lopez, and D. V. Nanopoulos, "Analysis of LEP constraints on supersymmetric models with a light gravitino", *Phys. Lett. B* **394** (1997) 354, doi:10.1016/S0370-2693(97)00019-1, arXiv:hep-ph/9610470.

[42] M. Dine, A. E. Nelson, Y. Nir, and Y. Shirman, "New tools for low energy dynamical supersymmetry breaking", *Phys. Rev. D* **53** (1996) 2658, doi:10.1103/PhysRevD.53.2658, arXiv:hep-ph/9507378.

[43] M. A. Ajaib, I. Gogoladze, F. Nasir, and Q. Shafi, "Revisiting mGMSB in light of a 125 GeV Higgs", *Phys. Lett. B* **713** (2012) 462, doi:10.1016/j.physletb.2012.06.036, arXiv:1204.2856.

[44] P. Grajek, A. Mariotti, and D. Redigolo, "Phenomenology of general gauge mediation in light of a 125 GeV Higgs", *J. High Energy Phys.* **07** (2013) 109, doi:10.1007/JHEP07(2013)109, arXiv:1303.0870.

[45] P. Meade, M. Reece, and D. Shih, "Prompt decays of general neutralino NLSPs at the Tevatron", *J. High Energy Phys.* **05** (2010) 105, doi:10.1007/JHEP05(2010)105, arXiv:0911.4130.

[46] S. Myers, "The LEP collider, from design to approval and commissioning", John Adams' Lecture CERN-91-08, 1991, doi:10.5170/CERN-1991-008.

[47] R. R. Wilson, "The Tevatron", *Phys. Today* **30N10** (1977) 23, doi:10.1063/1.3037746.

[48] ATLAS and CMS Collaborations, "Measurements of the Higgs boson production and decay rates and constraints on its couplings from a combined ATLAS and CMS analysis of the LHC pp collision data at $\sqrt{s} = 7$ and 8 TeV", *J. High Energy Phys.* **08** (2016) 045, doi:10.1007/JHEP08(2016)045.

[49] CMS and LHCb Collaborations, "Observation of the rare $B_s^0 \to \mu^+\mu^-$ decay from the combined analysis of CMS and LHCb data", *Nature* **522** (2015) 68,

doi:10.1038/nature14474, arXiv:1411.4413.

[50] CMS Collaboration, "Search for long-lived particles in events with photons and missing energy in proton-proton collisions at $\sqrt{s} = 7\,\text{TeV}$", *Phys. Lett. B* **722** (2013) 273, doi:10.1016/j.physletb.2013.04.027.

[51] ATLAS Collaboration, "Search for nonpointing and delayed photons in the diphoton and missing transverse momentum final state in 8 TeV *pp* collisions at the LHC using the ATLAS detector", *Phys. Rev. D* **90** (2014) 112005, doi:10.1103/PhysRevD.90.112005.

[52] CMS Collaboration, "Search for stealth supersymmetry in events with jets, either photons or leptons, and low missing transverse momentum in pp collisions at 8 TeV", *Phys. Lett. B* **743** (2015) 503, doi:10.1016/j.physletb.2015.03.017.

[53] CMS Collaboration, "Search for natural supersymmetry in events with top quark pairs and photons in pp collisions at $\sqrt{s} = 8\,\text{TeV}$", *J. High Energy Phys.* **03** (2018) 167, doi:10.1007/JHEP03(2018)167.

[54] CMS Collaboration, "Search for supersymmetry in events with a photon, a lepton, and missing transverse momentum in pp collisions at $\sqrt{s} = 8\,\text{TeV}$", *Phys. Lett. B* **757** (2016) 6, doi:10.1016/j.physletb.2016.03.039.

[55] ATLAS Collaboration, "Search for supersymmetry in a final state containing two photons and missing transverse momentum in $\sqrt{s} = 13\,\text{TeV}$ pp collisions at the LHC using the ATLAS detector", *Eur. Phys. J. C* **76** (2016) 517, doi:10.1140/epjc/s10052-016-4344-x.

[56] CMS Collaboration, "Search for supersymmetry in events with photons and missing transverse energy in pp collisions at 13 TeV", *Phys. Lett. B* **769** (2017) 391, doi:10.1016/j.physletb.2017.04.005, arXiv:1611.06604.

[57] CMS Collaboration, "Search for supersymmetry with Higgs boson to diphoton decays using the razor variables at $\sqrt{s} = 13\,\text{TeV}$", *Phys. Lett. B* **779** (2017) 166, doi:10.1016/j.physletb.2017.12.069, arXiv:1709.00384.

[58] ATLAS Collaboration, "Search for supersymmetry in events with photons, jets and missing transverse energy with the ATLAS detector in 13 TeV pp collisions", ATLAS Conference Report ATLAS-CONF-2016-066, 2016.

[59] CMS Collaboration, "Search for supersymmetry with photons in pp collisions at $\sqrt{s} = 8\,\text{TeV}$", *Phys. Rev. D* **92** (2015) 072006, doi:10.1103/PhysRevD.92.072006.

[60] CMS Collaboration, "Search for gauge-mediated supersymmetry in events with at least one photon and missing transverse momentum in pp collisions at $\sqrt{s} = 13\,\text{TeV}$", *Phys. Lett. B* **780** (2018) 118, doi:10.1016/j.physletb.2018.02.045.

[61] LHC New Physics Working Group, "Simplified models for LHC new physics searches", *J. Phys. G* **39** (2012) 105005, doi:10.1088/0954-3899/39/10/105005, arXiv:1105.2838.

[62] CMS Collaboration, "Interpretation of searches for supersymmetry with simplified models", *Phys. Rev. D* **88** (2013) 052017, doi:10.1103/PhysRevD.88.052017.

[63] L. Evans and P. Bryant, "LHC Machine", *J. Instrum.* **3** (2008) S08001, doi:10.1088/1748-0221/3/08/S08001.

[64] R. Bruce et al., "Reaching record-low β^* at the CERN Large Hadron Collider using a novel scheme of collimator settings and optics", *Nucl. Instrum. Meth. A* **848** (2017) 19, doi:10.1016/j.nima.2016.12.039.

[65] ATLAS Collaboration, "The ATLAS experiment at the CERN Large Hadron Collider", *J. Instrum.* **3** (2008) S08003, doi:10.1088/1748-0221/3/08/S08003.

[66] ALICE Collaboration, "The ALICE experiment at the CERN LHC", *J. Instrum.* **3** (2008) S08002, doi:10.1088/1748-0221/3/08/S08002.

[67] LHCb Collaboration, "The LHCb Detector at the LHC", *J. Instrum.* **3** (2008) S08005, doi:10.1088/1748-0221/3/08/S08005.

[68] CMS Collaboration, "The CMS experiment at the CERN LHC", *J. Instrum.* **3** (2008) S08004, doi:10.1088/1748-0221/3/08/S08004.

[69] CMS Collaboration, "CMS luminosity measurement for the 2015 data-taking period", CMS Physics Analysis Summary CMS-PAS-LUM-15-001, 2015.

[70] CMS Collaboration, "Public CMS data quality information", TWiki Webpage https://twiki.cern.ch/twiki/bin/view/CMSPublic/DataQuality#Dataset_For_Morion17_Conference, 2017, Accessed on 2017-04-19.

[71] J. Alwall et al., "The automated computation of tree-level and next-to-leading order differential cross sections, and their matching to parton shower simulations", *J. High Energy Phys.* **07** (2014) 079, doi:10.1007/JHEP07(2014)079, arXiv:1405.0301.

[72] CMS Collaboration, "Description and performance of track and primary-vertex reconstruction with the CMS tracker", *J. Instrum.* **9** (2014) P10009, doi:10.1088/1748-0221/9/10/P10009.

[73] CMS Collaboration, "CMS Physics: Technical Design Report Volume 1: Detector Performance and Software", CMS Technical Design Report CMS-TDR-008-1, 2006.

[74] CMS Collaboration, "Crystal ECAL performance and operation", *J. Instrum.* **5** (2010) T03010, doi:10.1088/1748-0221/5/03/T03010.

[75] CMS Collaboration, "Performance of the CMS hadron calorimeter with cosmic ray muons and LHC beam data", *J. Instrum.* **5** (2010) T03012, doi:10.1088/1748-0221/5/03/T03012.

[76] CMS Collaboration, "The CMS trigger system", *J. Instrum.* **12** (2017) P01020, doi:10.1088/1748-0221/12/01/P01020.

[77] CMS Collaboration, R. Manzoni, "Overview talk on trigger performances in run II (CMS)", in *5th Internationial Conference on New Frontiers in Physics (ICNFP2016)*, Crete, Geece, July, 2016.

[78] CMS Collaboration, "CMS Luminosity Measurements for the 2016 Data Taking Period", CMS Physics Analysis Summary CMS-PAS-LUM-17-001, 2017.

[79] S. van der Meer, "Calibration of the effective beam height in the ISR", Technical Report CERN-ISR-PO-68-31, 1968.

[80] P. Odier, M. Ludwig, and S. Thoulet, "The DCCT for the LHC beam intensity measurement", Technical Report CERN-BE-2009-019, 2009.

[81] D. Belohrad et al., "The LHC fast BCT system: A comparison of design parameters with initial performance", Technical Report CERN-BE-2010-010, 2010.

[82] NNPDF Collaboration, "Parton distributions for the LHC Run II", *J. High Energy Phys.* **04** (2015) 040, doi:10.1007/JHEP04(2015)040, arXiv:1410.8849.

[83] T. Sjöstrand, S. Mrenna, and P. Z. Skands, "A brief introduction to PYTHIA 8.1", *Comput. Phys. Commun.* **178** (2008) 852, doi:10.1016/j.cpc.2008.01.036, arXiv:0710.3820.

[84] CMS Collaboration, "Event generator tunes obtained from underlying event and multiparton scattering measurements", *Eur. Phys. J. C* **76** (2016) 155, doi:10.1140/epjc/s10052-016-3988-x, arXiv:1512.00815.

[85] J. Alwall et al., "Comparative study of various algorithms for the merging of parton showers and matrix elements in hadronic collisions", *Eur. Phys. J. C* **53** (2008) 473, doi:10.1140/epjc/s10052-007-0490-5, arXiv:0706.2569.

[86] R. Frederix and S. Frixione, "Merging meets matching in MC@NLO", *J. High Energy Phys.* **12** (2012) 061, doi:10.1007/JHEP12(2012)061, arXiv:1209.6215.

[87] GEANT4 Collaboration, "GEANT4 - a simulation toolkit", *Nucl. Instrum. Meth. A* **506** (2003) 250, doi:10.1016/S0168-9002(03)01368-8.

[88] CMS Collaboration, "The fast simulation of the CMS detector at LHC", *J. Phys. Conf. Ser.* **331** (2011) 032049, doi:10.1088/1742-6596/331/3/032049.

[89] CMS Collaboration, S. Sekmen, "Recent developments in CMS Fast Simulation", in *Proceedings, 38th International Conference on High Energy Physics (ICHEP 2016)*, Chicago, Illinois, USA, August, 2016, arXiv:1701.03850, [PoS(ICHEP2016)181].

[90] G. Grindhammer, M. Rudowicz, and S. Peters, "The fast simulation of electromagnetic and hadronic showers", *Nucl. Instrum. Meth. A* **290** (1990) 469, doi:10.1016/0168-9002(90)90566-0.

[91] G. Grindhammer and S. Peters, "The Parameterized simulation of electromagnetic showers in homogeneous and sampling calorimeters", in *International Conference on Monte Carlo Simulation in High-Energy and Nuclear Physics*, MC 93 Tallahassee, Florida, February, 1993, arXiv:hep-ex/0001020,

[92] M. K. Kiesel, "Improvements of the fast simulation of the CMS detector", in *DPG 2015: Spring Meeting of the German Physical Society*, Wuppertal, Germany, March, 2015.

[93] CMS Collaboration, "Alignment of the CMS tracker with LHC and cosmic ray data", *J. Instrum.* **9** (2014) P06009, doi:10.1088/1748-0221/9/06/P06009.

[94] CMS Collaboration, "Performance of photon reconstruction and identification with the CMS detector in proton-proton collisions at $\sqrt{s} = 8\,\text{TeV}$", *J. Instrum.* **10** (2015) P08010, doi:10.1088/1748-0221/10/08/P08010.

[95] CMS Collaboration, "Particle-flow reconstruction and global event description with the CMS detector", *J. Instrum.* **12** (2017) P10003, doi:10.1088/1748-0221/12/10/P10003, arXiv:1706.04965.

[96] K. Rose, "Deterministic annealing for clustering, compression, classification, regression, and related optimization problems", *Proceedings of the IEEE* **86** (1998) 2210, doi:10.1109/5.726788.

[97] M. Cacciari, G. P. Salam, and G. Soyez, "The anti-k_t jet clustering algorithm", *J. High Energy Phys.* **0804** (2008) 063, doi:10.1088/1126-6708/2008/04/063.

[98] R. K. Ellis, W. J. Stirling, and B. R. Webber, "QCD and collider physics". Cambridge monographs on particle physics, nuclear physics and cosmology. Cambridge University Press, 1996. doi:10.1017/CBO9780511628788.

[99] S. D. Ellis and D. E. Soper, "Successive combination jet algorithm for hadron collisions", *Phys. Rev. D* **48** (1993) 3160, doi:10.1103/PhysRevD.48.3160, arXiv:hep-ph/9305266.

[100] Y. L. Dokshitzer, G. D. Leder, S. Moretti, and B. R. Webber, "Better jet clustering algorithms", *J. High Energy Phys.* **08** (1997) 001, doi:10.1088/1126-6708/1997/08/001, arXiv:hep-ph/9707323.

[101] M. Wobisch and T. Wengler, "Hadronization corrections to jet cross-sections in deep inelastic scattering", *Proceedings for Monte Carlo generators for HERA physics* (1998) 270, arXiv:hep-ph/9907280.

[102] M. Cacciari, G. P. Salam, and G. Soyez, "FastJet User Manual", *Eur. Phys. J. C* **72** (2012) 1896, doi:10.1140/epjc/s10052-012-1896-2, arXiv:1111.6097.

[103] CMS Collaboration, "Pileup Removal Algorithms", CMS Physics Analysis Summary CMS-PAS-JME-14-001, 2014.

[104] CMS Collaboration, "Determination of jet energy calibration and transverse momentum resolution in CMS", *J. Instrum.* **6** (2011) P11002, doi:10.1088/1748-0221/6/11/P11002.

[105] CMS Collaboration, "Jet energy scale and resolution performances with 13 TeV data", CMS Detector Performance Summary CMS-DP-2016-020, 2016.

[106] CMS Collaboration, "Jet algorithms performance in 13 TeV data", CMS Physics Analysis Summary CMS-PAS-JME-16-003, 2016.

[107] CMS Collaboration, "Performance of missing energy reconstruction in 13 TeV pp collision data using the CMS detector", CMS Physics Analysis Summary CMS-PAS-JME-16-004, 2016.

[108] CMS Collaboration, "Electron and photon performance in CMS with the full 2016 data sample", CMS Detector Performance Summary CMS-DP-2017-004, 2017.

[109] M. K. Kiesel, "Coding HLT paths in ConfDB", CMS Internal Trigger Tutorial, CERN, Geneva, March, 2015.

[110] I. Bird, "Computing for the Large Hadron Collider", *Ann. Rev. Nucl. Part. Sci.* **61** (2011) 99, doi:10.1146/annurev-nucl-102010-130059.

[111] I. Bird et al., "Update of the computing models of the WLCG and the LHC experiments", Technical Report CERN-LHCC-2014-014, LCG-TDR-002, 2014.

[112] K. Bloom, "CMS software and computing for LHC Run 2", in *Proceedings, 38th International Conference on High Energy Physics (ICHEP 2016)*, Chicago, IL, USA, August, 2016, arXiv:1611.03215,

[113] R. Brun and F. Rademakers, "ROOT: An object oriented data analysis framework", *Nucl. Instrum. Meth. A* **389** (1997) 81, doi:10.1016/S0168-9002(97)00048-X.

[114] I. Antcheva et al., "ROOT: A C++ framework for petabyte data storage, statistical analysis and visualization", *Comput. Phys. Commun.* **180** (2009) 2499, doi:10.1016/j.cpc.2009.08.005, arXiv:1508.07749.

[115] C. Rogan, "Kinematics for new dynamics at the LHC", Report CALT-68-2790, 2010, arXiv:1006.2727.

[116] CMS Collaboration, "Inclusive search for squarks and gluinos in pp collisions at $\sqrt{s} = 7$ TeV", *Phys. Rev. D* **85** (2012) 012004, doi:10.1103/PhysRevD.85.012004.

[117] L. Randall and D. Tucker-Smith, "Dijet searches for supersymmetry at the LHC", *Phys. Rev. Lett.* **101** (2008) 221803, doi:10.1103/PhysRevLett.101.221803, arXiv:0806.1049.

[118] CMS Collaboration, "Search strategy for exclusive multi-jet events from supersymmetry at CMS", CMS Physics Analysis Summary CMS-PAS-SUS-09-001, 2009.

[119] G. Cowan, K. Cranmer, E. Gross, and O. Vitells, "Asymptotic formulae for likelihood-based tests of new physics", *Eur. Phys. J. C* **71** (2011) 1554, doi:10.1140/epjc/s10052-011-1554-0,10.1140/epjc/s10052-013-2501-z, arXiv:1007.1727, [Erratum: *Eur. Phys. J. C* **73** (2013) 2501].

[120] CMS Collaboration, "Jet energy scale and resolution in the CMS experiment in pp collisions at 8 TeV", *J. Instrum.* **12** (2016) P02014, doi:10.1088/1748-0221/12/02/P02014.

[121] N. D. Gagunashvili, "Pearson's chi-square test modifications for comparison of unweighted and weighted histograms and two weighted histograms", in *Proceedings, 11th International Workshop on Advanced computing and analysis techniques in physics research (ACAT 2007)*, Amsterdam, Netherlands, April, 2007, PoS(ACAT2007)060,

[122] K. S. Cranmer, "Kernel estimation in high-energy physics", *Comput. Phys. Commun.* **136** (2001) 198, doi:10.1016/S0010-4655(00)00243-5, arXiv:hep-ex/0011057.

[123] J. W. Cooley and J. W. Tukey, "An algorithm for the machine calculation of complex Fourier series", *Math. Comp.* **19** (1965) 297, doi:10.1090/S0025-5718-1965-0178586-1.

[124] CMS Collaboration, "Measurement of the production cross section for pp $\to Z\gamma \to \nu\nu\gamma$ at $\sqrt{s} = 13$ TeV at CMS", CMS Physics Analysis Summary CMS-PAS-SMP-16-004, 2016.

[125] CMS Collaboration, "Measurement of the semileptonic $t\bar{t} + \gamma$ production cross section in pp collisions at $\sqrt{s} = 8$ TeV", *J. High Energy Phys.* **10** (2017) 006, doi:10.1007/JHEP10(2017)006, arXiv:1706.08128.

[126] CMS Collaboration, "Measurement of the $W\gamma$ and $Z\gamma$ inclusive cross sections in pp collisions at $\sqrt{s} = 7$ TeV and limits on anomalous triple gauge boson couplings", *Phys. Rev. D* **89** (2014) 092005, doi:10.1103/PhysRevD.89.092005.

[127] CMS Collaboration, "CMS SUSY Results: Objects Efficiency", TWiki Webpage https://twiki.cern.ch/twiki/bin/view/CMSPublic/SUSMoriond2017ObjectsEfficiency, 2017, Accessed on 2017-04-19.

[128] M. Cacciari et al., "The $t\bar{t}$ cross-section at 1.8 TeV and 1.96 TeV: A study of the systematics due to parton densities and scale dependence", *J. High Energy Phys.* **04** (2004) 068, doi:10.1088/1126-6708/2004/04/068, arXiv:hep-ph/0303085.

[129] S. Catani, D. de Florian, M. Grazzini, and P. Nason, "Soft gluon resummation for Higgs boson production at hadron colliders", *J. High Energy Phys.* **07** (2003) 028, doi:10.1088/1126-6708/2003/07/028, arXiv:hep-ph/0306211.

[130] J. Butterworth et al., "PDF4LHC recommendations for LHC Run II", *J. Phys. G* **43** (2016) 023001, doi:10.1088/0954-3899/43/2/023001, arXiv:1510.03865.

[131] C. Borschensky et al., "Squark and gluino production cross sections in pp collisions at $\sqrt{s} = 13$, 14, 33 and 100 TeV", *Eur. Phys. J. C* **74** (2014) 3174, doi:10.1140/epjc/s10052-014-3174-y, arXiv:1407.5066.

[132] A. Kulesza and L. Motyka, "Threshold resummation for squark-antisquark and gluino-pair production at the LHC", *Phys. Rev. Lett.* **102** (2009) 111802, doi:10.1103/PhysRevLett.102.111802, arXiv:0807.2405.

[133] T. Junk, "Confidence level computation for combining searches with small statistics", *Nucl. Instrum. Meth. A* **434** (1999) 435, doi:10.1016/S0168-9002(99)00498-2, arXiv:hep-ex/9902006.

[134] A. L. Read, "Presentation of search results: the CL_s technique", *J. Phys. G* **28** (2002) 2693, doi:10.1088/0954-3899/28/10/313.

[135] ATLAS and CMS Collaborations, "Procedure for the LHC Higgs boson search combination in Summer 2011", Technical Report CMS-NOTE-2011-005, ATL-PHYS-PUB-2011-11, 2011.

[136] S. Wilks, "The Large-Sample Distribution of the Likelihood Ratio for Testing Composite Hypotheses", *Ann. Math. Statist.* **9** (1938) 60, doi:10.1214/aoms/1177732360.

[137] B. N. Delaunay, "Sur la sphère vide", *Bulletin of Academy of Sciences of the USSR* (1934) 793.

[138] M. K. Kiesel for the CMS Collaboration, "Search for Supersymmetry in Events with one Photon, Jets and missing transverse Energy at $\sqrt{s} = 8\,\text{TeV}$", *Proceedings, 20th International Conference on Particles and Nuclei* (2014) 707, doi:10.3204/DESY-PROC-2014-04/278.

[139] CMS Collaboration, "Search for supersymmetry in events with photons and missing energy", CMS Physics Analysis Summary CMS-PAS-SUS-12-018, 2012.

Acknowledgements

I would like to thank everyone who supported me during my time as PhD student.

My adviser Prof. Dr. Lutz Feld gave me the opportunity to work on an interesting topic, helpful advice, and the freedom to develop this analysis as I wanted. His correctness and his quick comprehension of difficult relationships are an example for me.

I would like to thank Prof. Dr. Jörg Pretz for his lecture on statistical methods and for agreeing to be the second referee of this work.

I would also like to thank all other members of our working group, especially Johannes Schulz, Johannes Lange, Dr. Jan-Frederik Schulte, Dr. Christian Autermann, Christian Schomakers and Marius Teroerde for many fruitful discussions. For many detailed insights into the hardware of the CMS experiment, I would like to thank Dr. Katja Klein, Dr. Jan Sammet, Martin Lipinski, Marius Preuten, and Max Rauch. I am happy that I found not only colleagues, but also friends.

It was also a pleasure to work with many CMS colleges from different countries all over the world, helpful advice did come around-the-clock. I would like to thank Wolfgang Adams, Claudio Campagnari, Si Xie, and Andrew Askew for reviewing the analysis, and Michael Hildrith for carefully and thoroughly reviewing the publication. More generally, I am obliged to thank the CMS collaboration for building the detector, taking data, developing event reconstruction algorithms, and providing recommendations for object selections. Processing the data would not have been possible without the worldwide LHC computing grid. Thanks to the LHC team for also delivering the data used in this analysis.

For the IT service in Aachen, I would like to thank Dr. Thomas Kress, Dr. Andreas Nowack, and Nikolas Zimmermann.

This thesis would not have been possible without the support of my family and friends. Thank you for the instructing academic debates about physics and science, and thank you for the relaxing times afterwards. Special thanks to my wife Ulrike and my daughter Eleonore, who both fill my heart with joy.